

Real-Time Optical Intensity Correlation Using Photorefractive BSO

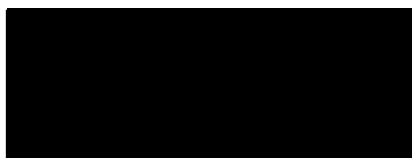
Zhao Qi Wang

A thesis submitted in partial fulfilment of the requirements
for the degree of Doctor of Philosophy

Sponsoring establishment: University of Abertay Dundee
Submitted: May 1995

I certify that this thesis is the true and accurate version of the thesis approved by the
examiners.

Signed

A black rectangular box redacting the signature of the Director of Studies.

(Director of Studies)

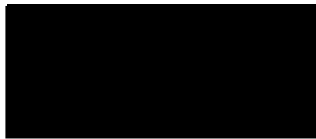
..... Date

28 / 8 / 95

Declaration

I hereby declare that while registered as a candidate for the degree for which this thesis is presented I have not been a candidate for any other award. I further declare that except where stated, the work contained in this thesis is original and was performed by myself.

Signed



.... (Zhao Qi Wang)

Date 28 / 8 / 1995

Acknowledgements

Thanks to my supervisors Dr.'s Colin Cartwright and Allan Gillespie for their encouragement, assistance and patience throughout the time of this work. Without their support, this research could not have been implemented. Also thanks to Mr. Brian Lawrenson, my external supervisor, for many discussions concerning this research.

Special thanks to Dr. B. Jefferies and Dr. P.F. Martin who, as Heads of Department, lent their support to this research.

The advice and assistance of the technical staff of the Department of Electronic and Electrical Engineering, especial Leon who provided so much help in the laser laboratory and computer-aided vision laboratory, is gratefully acknowledged. Thanks are due to the departmental secretarial staff for their assistance and co-operation.

This thesis is dedicated to my dear wife, Zhu Qiu-Zhen, and my wonderful mother, Kong Qing-Gui.

Real-Time Optical Intensity Correlation Using Photorefractive BSO

Zhao Qi Wang

Abstract

Real-time optical intensity correlation using a photorefractive BSO crystal and a liquid crystal television is implemented. The underlying physics basis is considered, some specific techniques to improve the operation are proposed, and several optical pattern recognition tasks are achieved.

Photorefractive BSO is used as the holographic recording medium in the real-time intensity correlator. To improve the dynamic holographic recording, a moving grating technique is adopted. The nonlinear effects of moving gratings at large fringe modulation are experimentally investigated, and are compared with numerical predictions.

Optical bias is adopted to overcome the difficulty of a large drop in the optimum fringe velocity with moving gratings. The effects of optical bias on the optimum fringe velocity and on the diffraction efficiency are studied.

To overcome the inherent drawback of low discrimination of intensity correlation in optical pattern recognition, real-time edge-enhanced intensity correlation is achieved by means of nonlinear holographic recording in BSO.

Real-time colour object recognition is achieved by using a commercially available and inexpensive colour liquid crystal television in the intensity correlator. Multi-class object recognition is achieved with a synthetic discriminant function filter displayed by the Epson liquid crystal display in the real-time intensity correlator. The phase and intensity modulation properties of the Epson liquid crystal display are studied.

A further research topic which uses the Epson liquid crystal display to realize a newly designed spatial filter, the quantized amplitude-compensated matched filter, is proposed. The performance merits of the filter are investigated by means of computer simulations.

SYMBOLS

α	Absorption Constant.
Δ	Discrimination of Spatial Filter.
e	Electronic Charge.
E_D	Diffusion Electric Field, $\left(\frac{KTk_B}{e}\right)$.
E_M	$\frac{\gamma_R N_A}{\mu K}$.
E_0	Applied Electric Field.
E_Q	Saturation Electric Field, $\left(\frac{eN_A}{\epsilon K}\right)$.
E_r	r th Fourier Component of Electric Field.
E_{sc}	Space-Charge Field.
ϵ	Permittivity.
F	Fourier Transform.
F^{-1}	Inverse Fourier Transform.
Fr	Fresnel Transform.
φ	Phase Shift.
Φ	Phase Angle of Space-Charge Field.
ϕ	Slant Angle of Grating.
G	Enhancement of Diffraction Efficiency by a Moving Grating.
γ	Phase Conversion Factor of Waves, $\left(\frac{2\pi\Delta n_s \cos(\Phi)}{\lambda_0 \cos(\vartheta_0)}\right)$.
γ_R	Recombination Rate.
r_{ij}	Linear Electro-Optic Coefficients.
Γ	Intensity Coupling Constant of Waves, $\left(\frac{4\pi\Delta n_s \sin(\Phi)}{\lambda_0 \cos(\vartheta_0)}\right)$.
η	Diffraction Efficiency of Grating.
η_H	Light Efficiency of Spatial Filter.
I	Light Intensity.
I_{ob}	Intensity of Optical Bias.

J	Current Density.
J_r	r th Fourier Component of Current Density.
k_B	Boltzmann Constant.
\bar{K}	Grating Vector.
κ	Elongation of Piezo Stack for Unity Voltage.
χ	Coupling Constant of Waves, $\left(\frac{\pi\Delta n}{\lambda_0}\right)$.
L	Linear Operator of Optical System.
λ	Wavelength of Beam.
λ_0	Wavelength of Beam in Air.
ϑ_L	L th Diffracted Angle of Wave.
ϑ_0	Incident Angle of Wave.
Λ	Fringe Spacing.
m	Fringe Modulation, $\left(\frac{2(I_1 I_2)^{1/2}}{I_1 + I_2}\right)$.
μ	Free Electron Mobility.
n	Refractive Index.
n_0	Ordinary Refractive Index.
n_e	Extraordinary Refractive Index.
Δn_s	Saturation Value of Refractive Index Modulation.
N_A	Acceptor Density.
N_D	Donor Density.
N_D^+	Ionised Donor Density.
N_{Dr}^+	r th Fourier Component of Ionised Donor Density.
n	Free Electron Density.
n_0	Average Free Electron Density, $\left(\frac{sI_0 N_D}{\gamma_R N_A}\right)$.
n_r	r th Fourier Component of Free Electron Density.
n_{ob}	Photoelectron Density Generated by Optical Bias.

$P_R^{(TN)}$ Rotatory Power of Liquid Crystal Cell,

$$\left(1 - \frac{\sin^2 \left[\frac{\pi}{2} (1 + U^2)^{1/2} \right]}{1 + U^2}, U = 2T(\Delta n)/\lambda \right).$$

\vec{r} Position Vector of Wave.

$\vec{\rho}$ Incident Wave Vector.

s Photoionization Cross Section.

$\vec{\sigma}$ Diffracted Wave Vector.

σ_t Noise Tolerance of Spatial Filter.

T Thickness of Volume Grating.

T_{\parallel} Intensity Transmission for Parallel Liquid Crystal Cell,

$$\left(1 - P_R^{(TN)} \left[1 - \sin^2(2\psi) \sin^2 \left(\frac{\Delta\phi}{2} \right) \right] \right).$$

T Temperature.

τ Response Time of Medium.

τ_M Maxwell Dielectric Relaxation Parameter, $\left(\frac{\epsilon}{\epsilon\mu n_0} \right)$.

U_M Peak Amplitude of Voltage.

v Fringe Velocity.

v_{opt} Optimum Fringe Velocity.

V Voltage.

ψ Polarization Direction of Polarizer.

Contents:

Chapter 1. Introduction	1
1.1. Preliminary Remarks	1
1.1.1 Incoherent Systems	1
1.1.2. The Fresnel Transform	1
1.1.3. Real-Time Processing	2
1.2. Main Aspects of the Research	2
1.3. Outline of the Thesis	3
Chapter 2. Optical Linear Systems, and the Fourier and Fresnel Transforms	5
2.1. Optical Linear Spatially Invariant Systems	5
2.2. The Fourier Transform and its Properties	7
2.3. The Fresnel Transform and its Properties	10
2.4. Coherent and Incoherent Optical Systems	13
References	16
Chapter 3. Photorefractive BSO in Holography	18
3.1. Photo-Induced Space-Charge Field and the Refractive Index Grating	19
3.1.1. The Material Equations	19
3.1.2. Solution for the Space-Charge Field	20
3.1.3. Time-Independent Solution for the Space-Charge Field	22
3.1.4. Photo-Induced Refractive Index Modulation	22
3.2. Diffraction from Volume Refractive Index Gratings	26
3.2.1. Bragg Diffraction from a Volume Grating	26
3.2.2. Diffraction Efficiency for a Transmission Grating	29
3.3. Energy Transfer Between Writing Beams in the Steady State	31
3.4. Transient Energy Transfer Between Writing Beams	34
References	36

Chapter 4. Properties of Moving Gratings in BSO at Large Fringe Modulation	39
4.1. Introduction	39
4.2. Theory of a Moving Grating at Small Fringe Modulation	39
4.3. Numerical Results of a Moving Grating at Large Fringe Modulation	42
4.4. Experiments	48
4.4.1. Experimental Configuration	48
4.4.2. Resonant Effect of a Moving Grating	49
4.4.3. Nonlinearity of Optimum Fringe Velocity on Fringe Modulation	52
4.4.4. Nonlinear Enhancement of the Diffraction Efficiency	55
4.4.5. The Characteristics of the Absolute Diffraction Efficiency	56
4.4.6. The Dependence of the Optimum Velocity on the Applied Electric Field	58
4.4.7. The Dependence of the Optimum Velocity on the Writing Beam Intensity	59
4.5. Conclusions	
References	61
Chapter 5. The Effects of Optical Bias on Moving Gratings in BSO at Large Fringe modulation	63
5.1. Analysis	64
5.2. Experimental Configuration	65
5.3. Experimental Results	66
5.3.1. The Influence of Optical Bias on the Optimum Fringe Velocity	66
5.3.2. The Influence of Optical Bias on the Absolute Diffraction Efficiency	69
5.3.3. The Influence of Optical Bias on Enhancement of the Diffraction Efficiency	73
5.4. Conclusions	75
References	75

Chapter 6. Development of a Real-Time Intensity Correlator using BSO	77
6.1. Introduction	77
6.2. Basic Intensity Correlator using a Fresnel Transform Filter	79
6.2.1. Fabrication of the Fresnel Transform Filter	80
6.2.2. Optical Intensity Correlation using a Fresnel Transform Filter	82
6.3. Real-Time Intensity Correlator using BSO	84
6.4. Real-Time Edge-Enhanced Intensity Correlation with BSO	88
6.4.1. Incoherent Edge-Enhancement using BSO	89
6.4.2. Intensity Edge-Enhanced Correlation	90
6.4.3. Experiments and Results	91
6.5. Improved Real-Time Intensity Correlation by Moving Gratings	95
6.5.1. Factors Concerning the Application of a Moving Grating	95
6.5.2. Real-Time Intensity Correlation by Moving Gratings	96
6.5.3. Experiments and Results	96
6.6. Conclusions	99
References	100
 Chapter 7. Applications of a Liquid Crystal Television in a Real-Time Optical Correlator	 101
7.1. Optical Properties of Twisted Nematic Liquid Crystals	101
7.2. Colour Image Intensity Correlation with a Colour LCTV	104
7.2.1. Synthesis of a Multi-Wavelength Fresnel Transform Filter	105
7.2.2. Real-Time Colour Image Intensity Correlator	107
7.2.3. Experimental Results	109
7.3. Real-Time Intensity Correlation Using a Synthetic Discriminant Function Filter	112
7.3.1. Modulation Properties of the Epson Liquid Crystal Display	112
7.3.2. The Synthetic Discriminant Function	118
7.3.3. Experiments	119

7.4. Further Research: the Application of the LCTV to a Quantized Amplitude-Compensated Matched Filter	129
7.4.1. Performance Criteria of Spatial Filters	130
7.4.2. Different Types of Spatial Filters	131
7.4.3. A New Quantized Amplitude-Compensated Matched Filter	134
7.4.4. Application of the Epson Liquid Crystal Display to the Quantized Amplitude-Compensated Matched Filter	138
7.5. Conclusions	140
References	140
Chapter 8. Conclusions	145
Appendix. List of Publication	147

Chapter 1. Introduction

1.1. Preliminary Remarks

This research concentrates on real-time optical intensity (i.e. incoherent) correlation techniques using Fresnel transforms. There are three features of this research: incoherent illumination, the Fresnel transform, and real-time processing.

1.1.1. Incoherent Systems

During the last three decades coherent optical correlators with Fourier transform filters have dominated optical pattern recognition because coherent illumination endows an optical signal with complex (phase and amplitude) content so that a higher discrimination can be achieved. However, in the real world most objects are either self-luminous or illuminated with natural light, and usually coloured. An incoherent system is therefore more suitable to real object processing. The incoherent system also benefits from the absence of coherent noise, which is almost inevitable in a coherent system and severely affects the processing quality, and has relaxed requirements on the accuracy of alignment, which is significant in real-time processors. Furthermore, the incoherent system can tolerate the use of a spatial light modulator which suffers from phase variations such as the liquid crystal television employed in this research. In a coherent system, the inhomogeneity of phase variations in the liquid crystal television leads to a lack of spatial invariance, and phase conjugate techniques have to be adopted. With the incoherent system, on the other hand, the inhomogeneity of phase variations in the liquid crystal television has no influence at all. For these reasons an incoherent system is more convenient for real-time processing.

1.1.2. The Fresnel Transform

In a coherent system, the Fourier transform possesses unique translation invariance and the positioning problem of the input is therefore avoided. Fourier transform is also the most powerful means of altering image features. On the other hand, the Fresnel transform suffers from translation variance and the input has to be positioned accurately. However, in an incoherent system the translation variance of the Fresnel transform has no influence at all, and for optical pattern recognition selective alteration

of spatial frequencies is normally not necessary. Thus Fourier transform filters become less important in an incoherent correlator. From a sampling point of view, the Fresnel transform maintains as good an information content as the Fourier transform, but it offers flexibility of control over the light distribution, which is beneficial to the dynamic range of the holographic recording materials, to the light efficiency, and most importantly to the holographic recording with a moving grating developed in this research. Therefore we have implemented the Fresnel transform in this study.

1.1.3. Real-Time Processing

The essential merits of an optical processor are its two-dimensional processing ability and high processing speed. However, there are two processes which severely restrict its actual speed: the transformation of the input signals into optical signals and the preparation of the spatial filters. Therefore research on real-time performance is a most attractive topic and of special significance. The real-time performance requires real-time input and real-time holographic recording devices. As a holographic recording material, bismuth silicon oxide (BSO) possesses many attractive properties, for example fast response, good optical quality, high spatial frequency response, and low writing and erasing energy. As a type of spatial light modulator, the liquid crystal television has unique features such as the colour display, low cost, and commercial availability. In this research a photorefractive BSO crystal is used to record the Fresnel transform filters and liquid crystal televisions are used as real-time input devices in the intensity correlator.

1.2. Main Aspects of the Research

This research includes a fundamental investigation of the real-time recording material and display device, the techniques developed to improve the correlation performance, and specific applications in optical pattern recognition. The following are the main aspects:

— the experimental investigation on moving gratings at large fringe modulations, which is complementary to those previously reported on moving gratings at small fringe modulation, and to those reported on the numerical results of moving gratings at large fringe modulation;

- the study of the application of optical bias to the moving gratings, which provides an effective method to overcome the difficulty in the application of moving gratings;
- the realization of real-time incoherent edge enhancement and its application to edge-enhanced intensity correlation;
- the improvement of holographic recording with BSO by means of moving gratings and its application to real-time intensity correlation;
- the achievement of colour object recognition using a colour liquid crystal television in an intensity correlator, which could be realized in real-time recording with photorefractive crystals at a later stage;
- the realization of multi-class optical pattern recognition in a real-time intensity correlator by using a synthetic discriminant function filter implemented with an Epson liquid crystal display;
- a new spatial filter design, the quantized amplitude-compensated matched filter, its performance merits and potential implementation with an Epson liquid crystal display.

1.3. Outline of the Thesis

Chapter 2 introduces the theory of the linear optical system, by which our topic is mathematically treated, the properties of the Fourier and the Fresnel transforms, and the essentials of coherent and incoherent optical systems. Especially the Fresnel transform and the concept of the intensity impulse response, which are widely used in the following chapters, are emphasized.

Chapter 3 covers the associated fundamentals of the photorefractive material BSO: the Kukhtarev differential equations, the photo-induced space-charge field, the linear electro-optic effect, the refractive index ellipsoid, the Bragg condition, coupled wave theory, diffraction from a volume phase grating, and energy transfer between writing beams in steady and transient states.

Chapter 4 deals with the fundamentals of moving gratings at large fringe modulation. It includes the theory of a moving grating at small fringe modulation, the numerical analysis of a moving grating at large fringe modulation, and the experimental results of a moving grating at large fringe modulation: the resonant effect, the nonlinear dependence of the optimum fringe velocity and the enhancement of the diffraction efficiency on the fringe modulation, and the dependence of the optimum fringe velocity on the applied electric field and on the total writing beam intensity.

Chapter 5 describes the experiments and the analysis relating to optical bias, including the experimental results of the influence of the optical bias on the optimum fringe velocity, on the absolute diffraction efficiency and on the enhancement of the diffraction efficiency.

Chapter 6 describes the intensity correlator using a Fresnel transform filter, and presents the recent developments on real-time intensity correlation, the edge-enhanced intensity correlation and the intensity correlation improved by a moving grating.

In chapter 7 the properties and applications of liquid crystal televisions as a type of spatial light modulator are presented. These include the optical properties of the twisted nematic liquid crystal cell, the synthesis of a multi-wavelength Fresnel transform filter, the colour object intensity correlation using a colour liquid crystal television, the phase and the amplitude modulation properties of the Epson liquid crystal display in various modulation modes, the computation of the intensity synthetic discriminant function and its realization using the Epson liquid crystal display, and the experimental results of multi-class object recognition.

The last part of chapter 7 considers further research directions: the realization of the quantized amplitude-compensated matched filter using the Epson liquid crystal display working in its amplitude-mostly modulation mode. This part discusses the performance criteria of spatial filters, different spatial filters, the structure and the performance merits of the quantized amplitude-compensated matched filter, and a possible optical correlation system using the quantized amplitude-compensated matched filter.

Chapter 2. Optical Linear Systems, and the Fourier and Fresnel Transforms

2.1. Optical Linear Spatially Invariant Systems

The mathematical analysis throughout this thesis is based on the theory of linear systems. This is because (1) it is virtually impossible to make a complete analysis of a general system, and a linear system can be treated with normal mathematical analysis and an exact solution can be obtained; (2) most optical correlation systems are linear in the system variable (amplitude or intensity), and the linear system treatment in our optical system results in a quite accurate approximation.

An optical system can be described by the input excitation, system operation, and the output response. Suppose the input excitations are $f_i(x_1, y_1)$, where $i = 1, 2, \dots$ and (x_1, y_1) is the coordinate system of the input plane, the system operator is L , and the output responses are $g_i(x_2, y_2)$, where (x_2, y_2) is the coordinate system of the output plane. Their relationship can be written as:

$$g_i(x_2, y_2) = L[f_i(x_1, y_1)] \quad (2.1)$$

A specific optical system is the linear optical system^{2.1-2.3}, which satisfies the principle of superposition:

$$L\left[\sum_i C_i f_i(x_1, y_1)\right] = \sum_i C_i g_i(x_2, y_2) \quad (2.2)$$

where C_i are arbitrary constants. The above equation implies that the output response to a complicated input can be found by first decomposing this input into a linear combination of elementary functions, finding the response to each elementary function, and then taking the same linear combination of these elementary responses. Physically, linearity implies that the behaviour of the optical system is independent of the magnitude of the input.

Typical elementary functions are the impulse δ functions. According to the sifting property of the δ function, any input can be described as:

$$f(x_1, y_1) = \iint_{-\infty}^{\infty} f(x_0, y_0) \delta(x_1 - x_0, y_1 - y_0) dx_0 dy_0 \quad (2.3)$$

where (x_0, y_0) is the position of the δ function in the input plane. The output of the linear optical system can be obtained by substituting Eq. (2.3) into Eq. (2.1) and using Eq. (2.2), yielding:

$$\begin{aligned} g(x_2, y_2) &= L[f(x_1, y_1)] \\ &= \iint_{-\infty}^{\infty} f(x_0, y_0) L[\delta(x_1 - x_0, y_1 - y_0)] dx_0 dy_0 \end{aligned} \quad (2.4)$$

where $L[\delta(x_1 - x_0, y_1 - y_0)] = h(x_2, y_2; x_0, y_0)$ is the impulse response of the system. Obviously, the impulse response is not only a function of the coordinates of the output plane but also a function of the position of the impulse in the input plane. If the impulse response can be simplified as:

$$h(x_2, y_2; x_0, y_0) = h(x_2 - x_0, y_2 - y_0) \quad (2.5)$$

i.e. the displacement of the impulse at the input plane only causes a corresponding displacement of the impulse response at the output plane without any changes in the functional form, the system is said to be spatially shift invariant. Substituting Eq. (2.5) into Eq. (2.4), we have:

$$g(x_2, y_2) = \iint_{-\infty}^{\infty} f(x_1, y_1) h(x_2 - x_1, y_2 - y_1) dx_1 dy_1 \quad (2.6)$$

which is a two-dimensional convolution operation. Thus the output response for an optical linear spatially invariant system can be obtained by first calculating the response of the impulse at the origin of the input plane, and then convoluting it with the input excitation. Eq. (2.6) has a simple expression:

$$g(x_2, y_2) = f(x_1, y_1) * h(x_1, y_1) \quad (2.7)$$

where * denotes the convolution operation.

It should be remembered that the physical variables in Eq. (2.7) could be either complex amplitude or intensity, depending on which variable the optical system is linear in. We assign the term impulse response to the variable complex amplitude, and the term intensity impulse response to the variable intensity. Obviously, the intensity impulse response is the square of the modulus of the impulse response.

2.2. The Fourier Transform and its Properties

The two-dimensional Fourier transform is particularly important in optical information processing. It is the basis of spectrum analysis, spatial filtering, and the convolution and correlation operations of optical signals. This section considers the most useful properties of the Fourier transform, i.e. the translation and correlation theorems^{2.1-2.4}.

Suppose an object $f(x, y)$ is inserted in the front focal plane of a lens and illuminated by coherent light as shown in Fig. 2.1. The complex amplitude at the back focal plane of the lens is given by the Fourier transform:

$$\begin{aligned} F(p, q) &= F[f(x, y)] \\ &= \iint_{-\infty}^{\infty} f(x, y) \exp[-i(px + qy)] dx dy \end{aligned} \quad (2.8)$$

with

$$p = \frac{2\pi\alpha}{\lambda f}, \quad q = \frac{2\pi\beta}{\lambda f} \quad (2.9)$$

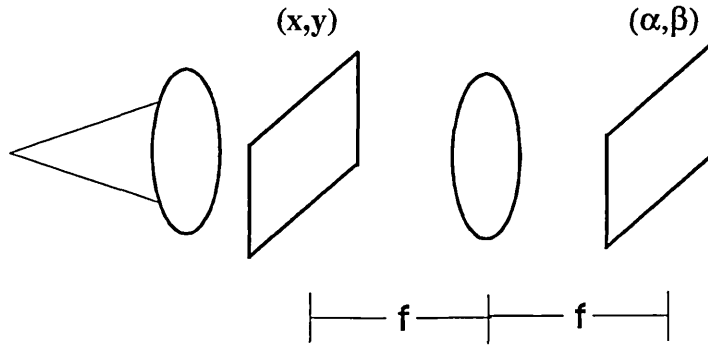


Fig. 2.1. An optical Fourier transform system.

where $F(p,q)$ is the Fourier spectrum, F denotes the Fourier transform, (α,β) is the coordinate system in the back focal plane of the lens, λ is the illuminating wavelength, f is the focal length of the transform lens, and (p,q) are the spatial frequency coordinates. The original object can be obtained from its Fourier spectrum by an inverse transform. This can be done by a succeeding transform lens with an inverse coordinate system selection in the back focal plane of the lens. The inverse Fourier transform is expressed as:

$$\begin{aligned}
 f(x,y) &= F^{-1}[F(p,q)] \\
 &= \iint_{-\infty}^{\infty} F(p,q) \exp[i(px + qy)] dpdq
 \end{aligned}
 \tag{2.10}$$

where F^{-1} denotes the inverse Fourier transform. The Fourier transform possesses the property of translation invariance. Suppose the input object shifts to a position (x_0, y_0) , Eq. (2.8) gives:

$$\begin{aligned}
 F[f(x - x_0, y - y_0)] &= \iint_{-\infty}^{\infty} f(x - x_0, y - y_0) \exp[-i(px + qy)] dx dy \\
 &= \exp[-i(px_0 + qy_0)] F(p,q)
 \end{aligned}
 \tag{2.11}$$

i.e. the translation of an object only causes a linear phase shift in the Fourier spectrum without a change in position.

Another useful property of the Fourier transform is the correlation theorem. Considers two Fourier transform pairs:

$$f_1(x, y) \leftrightarrow F_1(p, q), \text{ and } f_2(x, y) \leftrightarrow F_2(p, q) \quad (2.12)$$

The inverse Fourier transform of the function $F_1(p, q)F_2^*(p, q)$, where the superscript * denotes the complex conjugate, gives the cross correlation of the original objects:

$$\begin{aligned} \iint_{-\infty}^{\infty} F_1(p, q)F_2^*(p, q)\exp[i(px + qy)]dpdq &= \iint_{-\infty}^{\infty} f_1(x', y')f_2^*(x' - x, y' - y) dx' dy' \\ &= f_1(x, y) \otimes f_2(x, y) \end{aligned} \quad (2.13)$$

where \otimes denotes correlation operation. The correlation operation yields a sharply peaked intensity distribution, and therefore it can be used for signal detection.

Fig. 2.2 shows the so called 4-f optical system^{2,5}, which can perform two dimensional signal correlation. In Fig. 2.2 two transform lenses are arranged in succession, and a Fourier transform filter having the form of $F_2^*(p, q)$ is inserted at the back focal plane of the first transform lens. If a signal $f_1(x, y)$ is at the front focal plane of the first transform lens, the cross correlation of $f_1(x, y)$ with $f_2(x, y)$ will be formed at the back focal plane of the second transform lens. This correlator possesses shift invariance because Fourier transforms are used in the optical system.

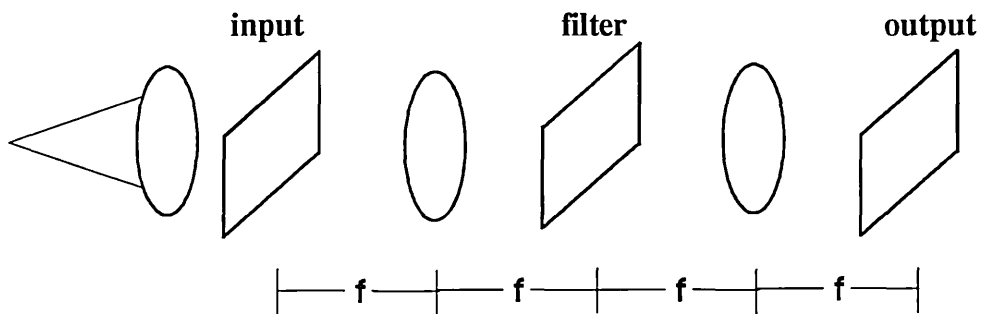


Fig. 2.2. The 4-f optical system for optical correlation.

2.3. The Fresnel Transform and its Properties

There are some applications of optical pattern recognition in which the translation invariance of the object could be a drawback. For instance, in machine vision correct placement of the object can be as important as its identity. In this case a space-variant optical correlator is required. This can be done by using Fresnel transforms in the optical correlator^{2,6}.

Consider the optical system shown in Fig. 2.3 where the output plane is not at the focal plane but a distance d away from the transform lens. For simplicity, we assume the input plane is at the front focal plane of the transform lens. The complex light distribution at the output plane is given by the Fresnel transform:

$$\begin{aligned}
 Fr(p,q) &= Fr[f(x,y)] \\
 &= \iiint_{-\infty}^{\infty} f(x,y) \exp\left\{\frac{i\pi}{\lambda f}[(\xi-x)^2 + (\eta-y)^2]\right\} \exp\left[\frac{-i\pi}{\lambda f}(\xi^2 + \eta^2)\right] \\
 &\quad \exp\left\{\frac{i\pi}{\lambda d}[(\alpha-\xi)^2 + (\beta-\eta)^2]\right\} dx dy d\xi d\eta \\
 &= F[f(x,y)Z(x,y; d,f)]
 \end{aligned} \tag{2.14}$$

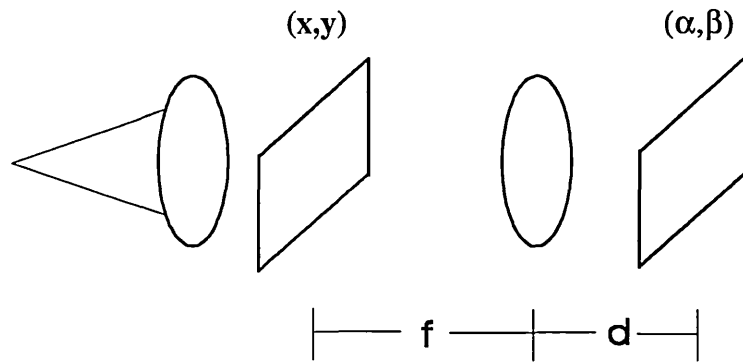


Fig. 2.3. An optical Fresnel transform system.

where p and q are as defined in Eq. (2.9) with (α, β) as the coordinate system of the selected Fresnel transform plane, $Fr(p,q)$ is the Fresnel spectrum, Fr denotes the

Fresnel transform, (ξ, η) is the coordinate system in the lens plane, and $Z(x, y; d, f)$ is a quadratic phase function:

$$Z(x, y; d, f) = \exp\left[\frac{i\pi}{\lambda f}\left(1 - \frac{d}{f}\right)(x^2 + y^2)\right] \quad (2.15)$$

Eq. (2.14) shows that the Fresnel transform of a signal can be regarded as the Fourier transform of the signal modified by a quadratic phase factor. The Fresnel transform shares the properties of the space and the spatial spectrum. If N samples are sufficient to represent an object accurately, N samples are also sufficient to sample the signal at any Fresnel transform plane^{2,7}. From this point of view, a Fresnel transform filter could perform as well as a Fourier transform filter. However the Fresnel transform possesses no translation invariance. Suppose the input has a displacement (x_0, y_0) , Eq. (2.14) yields:

$$\begin{aligned} Fr[f(x - x_0, y - y_0)] &= F[f(x - x_0, y - y_0)Z(x, y; d, f)] \\ &= \exp\left[\frac{i\pi}{\lambda f}\left(1 - \frac{d}{f}\right)(x_0^2 + y_0^2)\right] \exp[-i(px_0 + qy_0)] \\ &Fr\left[p - \frac{2\pi}{\lambda f}\left(1 - \frac{d}{f}\right)x_0, q - \frac{2\pi}{\lambda f}\left(1 - \frac{d}{f}\right)y_0\right] \end{aligned} \quad (2.16)$$

We can see that the displacement of the object introduces not only a phase shift $\exp[-i(px_0 + qy_0)]$, but also a positional shift $\left[\alpha - \left(1 - \frac{d}{f}\right)x_0, \beta - \left(1 - \frac{d}{f}\right)y_0\right]$ in its Fresnel spectrum. The larger the deviation of the distance d from the focal length f , the bigger the displacement of the Fresnel spectrum.

Using the shift variant property of the Fresnel transform, a space variant optical correlator can be set up. Such a correlator, as shown in Fig. 2.4, can detect not only the shape, but also the position of an object.

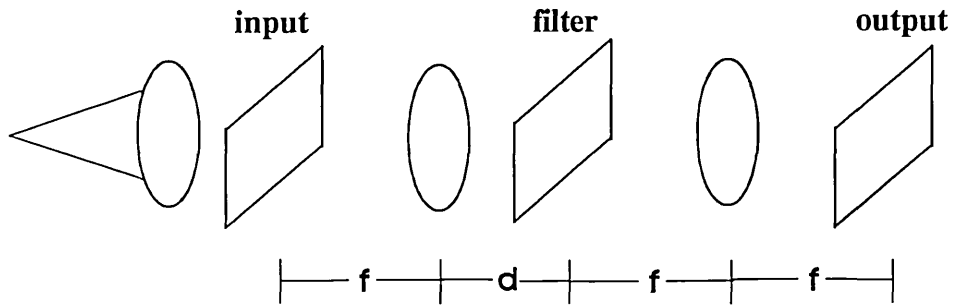


Fig. 2.4. An optical correlator using Fresnel transform filter.

In Fig. 2.4 the Fresnel transform filter given by the complex conjugate of Eq. (2.14) is placed at the filter plane where the Fresnel transform of an input signal is formed by the first transform lens. If the signal $f(x,y)$ is at the origin of the input plane, the complex light distribution just behind the Fresnel plane will be given by:

$$\begin{aligned}
 E(p,q) &= |\text{Fr}(p,q)|^2 \\
 &= |F[f(x,y)Z(x,y; d,f)]|^2
 \end{aligned}
 \tag{2.17}$$

The second transform lens makes the inverse Fourier transform of $E(p,q)$, yielding the complex light distribution at the output plane, according to the correlation theorem of the Fourier transform:

$$\begin{aligned}
 g(x,y) &= F^{-1}[E(p,q)] \\
 &= [f(x,y)Z(x,y; d,f)] \otimes [f(x,y)Z(x,y; d,f)]
 \end{aligned}
 \tag{2.18}$$

which is the autocorrelation of the signal modified by a quadratic phase angle.

If the signal has a displacement of (x_0, y_0) , its Fresnel spectrum will have not only a phase shift but also a position displacement as shown in Eq. (2.16). The light distribution will not overlap with the filter, and the autocorrelation cannot be obtained at the output plane. Thus with a Fresnel transform used in an optical correlator, the autocorrelation can be achieved only when the shape **and the position** of the input are both matched to the reference object.

The light distribution of the Fresnel spectrum is relatively uniform over a larger area than its Fourier counterpart. This helps to accommodate the dynamic range of the holographic recording material and brings about higher light efficiency in the case of diffused light illumination. It is also helpful in the case of a moving grating, since the relatively uniform light distribution eliminates the nonlinear effect of the optimum fringe velocity on the fringe modulation (see chapters 4 and 6).

2.4. Coherent and Incoherent Optical Systems

Consider an optical imaging system which is illuminated by a monochromatic light source Σ as shown in Fig 2.5. The basic assumption is that for an incremental light source $d\Sigma$, which induces a complex light field $u(x_1, y_1)$ at the input plane, the system is space invariant and linear in the complex amplitude. This assumption is generally valid for small amplitude disturbances over a small region of the input plane. If the complex amplitude transmittance in the input plane is $f(x, y)$, the complex amplitude distribution at the output plane is determined by the convolution:

$$g(x_2, y_2) = u(x_1, y_1) f(x_1, y_1) * h(x_1, y_1) \quad (2.19)$$

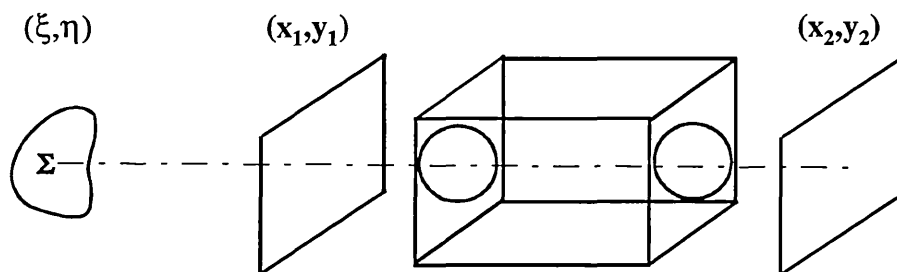


Fig. 2.5. An optical imaging system.

The output intensity due to $d\Sigma$ is the square of the modulus of $g(x_2, y_2)$, and the total output intensity produced by the whole light source is then given by:

$$I(x_2, y_2) = \iiint_{-\infty}^{\infty} \Gamma(x_1, y_1; x_1', y_1') h(x_2 - x_1, y_2 - y_1) h^*(x_2 - x_1', y_2 - y_1') f(x_1, y_1) f^*(x_1', y_1') dx_1 dy_1 dx_1' dy_1' \quad (2.20)$$

$$\Gamma(x_1, y_1; x_1', y_1') = \iint_{\Sigma} u(x_1, y_1) u^*(x_1', y_1') d\Sigma \quad (2.21)$$

where $\Gamma(x_1, y_1; x_1', y_1')$ is the mutual coherence function^{2.8-2.9} at the input plane induced by the light source, which obviously depends on the characteristics of the light source.

If the incremental light source has intensity $I(\xi, \eta)$, the induced complex disturbances $u(x_1, y_1)$ and $u(x_1', y_1')$ can be written, using spherical wave expressions, as:

$$u(x_1, y_1) = \frac{[I(\xi, \eta)]^{1/2}}{r_1} \exp\left(\frac{i2\pi r_1}{\lambda}\right) \quad (2.22)$$

$$u(x_1', y_1') = \frac{[I(\xi, \eta)]^{1/2}}{r_1'} \exp\left(\frac{i2\pi r_1'}{\lambda}\right) \quad (2.23)$$

where r_1 and r_1' are the distances from $d\Sigma$ to the points (x_1, y_1) and (x_1', y_1') , respectively. Substituting Eqs. (2.22) and (2.23) into (2.21) and applying the paraxial approximation to $r_1 - r_1'$, we have:

$$\Gamma(x_1, y_1; x_1', y_1') = \frac{1}{r^2} \iint_{\Sigma} I(\xi, \eta) \exp\left\{\frac{-i2\pi}{\lambda r} [\xi(x_1 - x_1') + \eta(y_1 - y_1')]\right\} d\xi d\eta \quad (2.24)$$

where r is the separation between the light source plane and the input plane. Eq. (2.24) indicates that the mutual coherence function is given by the Fourier transform of the intensity distribution of the light source.

If $I(\xi, \eta)$ is a δ function, which corresponds to a spatially coherent source, the integration of Eq. (2.24) will yield:

$$\Gamma(x_1, y_1; x_1', y_1') = K_1 \quad (2.25)$$

where K_1 is a constant. Substituting Eq. (2.25) into Eq. (2.20) we have:

$$I(x_2, y_2) = \left| \iint_{-\infty}^{\infty} f(x_1, y_1) h(x_2 - x_1, y_2 - y_1) dx_1 dy_1 \right|^2 \quad (2.26)$$

or alternatively:

$$g(x_2, y_2) = \iint_{-\infty}^{\infty} f(x_1, y_1) h(x_2 - x_1, y_2 - y_1) dx_1 dy_1 \quad (2.27)$$

i.e. the output complex amplitude is the convolution of the input complex amplitude with the impulse response. The system is linear with respect to complex amplitude. Eq. (2.27) can be expressed in the spatial frequency domain by a Fourier transformation:

$$G(p, q) = F(p, q)H(p, q) \quad (2.28)$$

where $G(p, q)$, $F(p, q)$ and $H(p, q)$ are the corresponding Fourier spectra of $g(x_2, y_2)$, $f(x_1, y_1)$ and $h(x_1, y_1)$, respectively.

If $I(\xi, \eta)$ is constant and Σ is infinitely large, which corresponds to a spatially incoherent source, the integration of (2.24) will give a δ function:

$$\Gamma(x_1, y_1; x_1', y_1') = K_2 \delta(x_1 - x_1', y_1 - y_1') \quad (2.29)$$

where K_2 is a constant. Substituting Eq. (2.29) into Eq. (2.20) we have:

$$I(x_2, y_2) = \iint_{-\infty}^{\infty} |f(x_1, y_1)|^2 |h(x_2 - x_1, y_2 - y_1)|^2 dx_1 dy_1 \quad (2.30)$$

where

$$|h(x_2 - x_1, y_2 - y_1)|^2 = h_i(x_2, y_2; x_1, y_1) \quad (2.31)$$

is the intensity impulse response. Eq. (2.30) indicates that the output intensity is the convolution of the input intensity with the intensity impulse response. The system is linear with respect to intensity. Again Eq. (2.30) can be expressed in the spatial frequency domain:

$$I(p,q) = F_i(p,q)H_i(p,q) \quad (2.32)$$

where $I(p,q)$, $F_i(p,q)$ and $H_i(p,q)$ are the corresponding Fourier transforms of $I(x_2,y_2)$, $|f(x_1,y_1)|^2$ and $h_i(x_1,y_1)$, respectively.

This thesis deals with intensity correlation. We treat our topic assuming linear system theory i.e. the output intensity response of the optical system is calculated by first calculating the intensity impulse response and then convoluting it with the input intensity excitation.

References:

- 2.1 J.W. Goodman, "Introduction to Fourier Optics", Chapter 2, McGraw-Hill, New York, 1968.
- 2.2. F.T.S. Yu, "Optical Information Processing", Chapter 1, John Wiley & Sons, New York, 1982.
- 2.3. P.K. Das, "Optical Signal Processing", Chapter 3, Springer-Verlag, Berlin, 1990.
- 2.4. G.W. Stroke, "An Introduction to Coherent Optics and Holography", Chapter 7, Academic Press, New York, 1969.
- 2.5. J.L. Horner, "Optical Signal Processing", Chapter 2, Academic Press, San Diego, 1987.
- 2.6 J.A. Davis, D.M. Cottrell, N. Nestorovic, and S.M. Highnote, "Space-variant Fresnel transform optical correlator", Appl. Opt., **31** (1992) 6889-6893.

2.7 A. Vander Lugt, "Optimum sampling of Fresnel transforms", *Appl. Opt.*, **29** (1990) 3352-3361.

2.8 M. Born and E. Wolf, "Principles of Optics", Chapter 10 Pergamon Press, Oxford, 1980.

2.9. F.T.S. Yu and S. Jutamulia, "Optical Signal Processing, Computing, and Neural Networks", Chapter 1, John Wiley & Sons, New York, 1992.

Chapter 3. Photorefractive BSO in Holography

The photorefractive crystal bismuth silicon oxide (BSO) has been widely used as a dynamic holographic medium in real-time coherent optical correlation^{3.1, 3.2}, novelty filtering^{3.3, 3.4} and incoherent optical correlation^{3.5}. Its attractive features are the fast response, good optical quality over a large surface area, high spatial frequency response, and low writing and erasing energy. These make it suitable for real-time applications. It is well known that when the writing beams are incident on a photorefractive crystal, a volume refractive index grating is established. This is the photorefractive effect. The mechanism is as follows: the writing beams produce a photo-excited charge-carrier distribution which corresponds to the intensity distribution of the interference pattern; the charge-carriers migrate via drift or diffusion into dark regions of the crystal, where they are re-trapped; the resultant space-charge distribution produces a space-charge field; this field modulates the refractive index of the crystal via the linear electro-optic effect and forms the refractive index grating. Fig. 3.1 shows the mechanism for the establishment of the refractive index modulation.

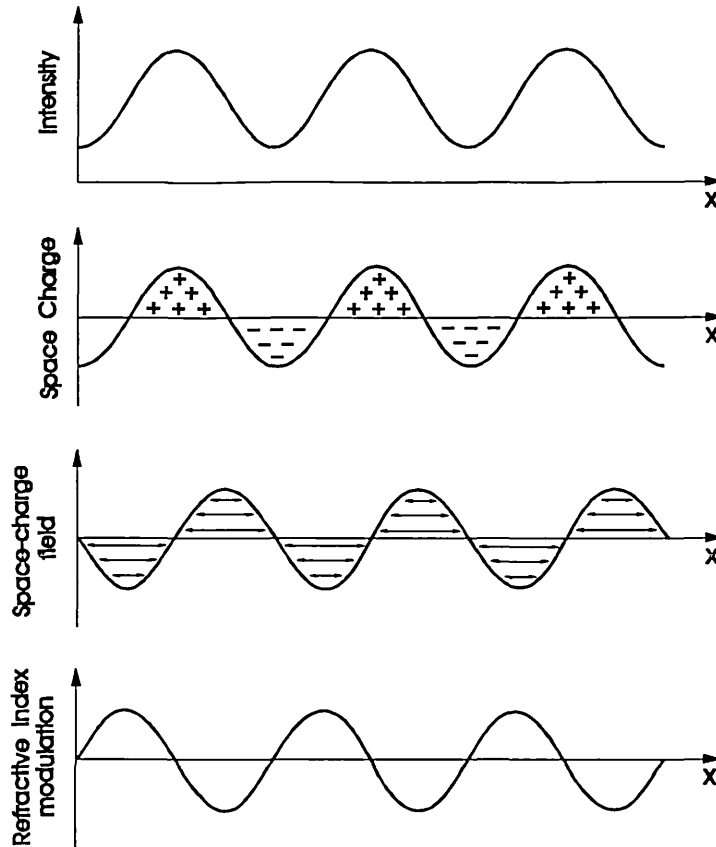


Fig. 3.1. The establishment of the refractive index modulation in photorefractive crystals.

3.1. Photo-Induced Space-Charge Field and the Refractive Index Grating

3.1.1. The Material Equations

The photo-induced space-charge field is the physical quantity responsible for the refractive index modulation in photorefractive materials. The differential equations proposed by Kukhtarev et al.^{3,6} are believed to characterize the space-charge field accurately:

$$\frac{\partial E}{\partial x} = \frac{e}{\epsilon} (N_A - N_D^+) \quad (3.1)$$

$$e \frac{\partial N_D^+}{\partial t} = \frac{\partial J}{\partial x} \quad (3.2)$$

$$\frac{\partial N_D^+}{\partial t} = sIN_D - \gamma_R n N_D^+ \quad (3.3)$$

$$J = e\mu n E - k_B T \mu \frac{\partial n}{\partial x} \quad (3.4)$$

where E is the total electric field made up of the external applied electric field E_0 and the created space-charge field E_{sc} , e is the electronic charge, N_A and N_D are the acceptor and the donor densities, respectively, N_D^+ is the density of ionised donors, ϵ is the permittivity of the material, J is the current density, μ is the free-electron mobility, I is the total incident beam intensity, s is the photoionization cross section, γ_R is the recombination rate, n is the free electron distribution, k_B is the Boltzmann constant, T is temperature, t is time, and ∂ is the differential operator. Eqs. (3.1) to (3.4) are valid under the conditions: $n \ll N_D$, $N_D^+ \ll N_D$, there is no thermal generation, the photovoltaic constant is zero, the spatial variation can be regarded as only in the x direction and ϵ is independent of x .

3.1.2. Solution for the Space-Charge Field

We consider the holographic recording of two interfering plane waves with intensities I_1 and I_2 . The intensity distribution of the interference pattern will be periodic:

$$I = I_0 [1 + m \cos(Kx)] \quad (3.5)$$

where $I_0 = I_1 + I_2$, $K = |\vec{K}| = \frac{2\pi}{\Lambda}$, \vec{K} is the grating vector, Λ is the fringe spacing, and m is the fringe modulation defined as:

$$m = \frac{2(I_1 I_2)^{1/2}}{I_0}, \quad \text{where } 0 \leq m \leq 1 \quad (3.6)$$

With this periodic illumination, all physical variables in the differential equations, N_D^+ , n , J , and E , are expected to vary in the same periodic manner, and they can be

represented in the form of a complex Fourier series. To a first-order approximation, which is valid in the case of small fringe modulation^{3,7}, the variables can be written as:

$$I = I_0 + \frac{1}{2}[I_0 m \exp(iKx) + cc] \quad (3.7)$$

$$N_D^+ = N_{D0}^+ + \frac{1}{2}[N_{D1}^+ \exp(iKx) + cc] \quad (3.8)$$

$$n = n_0 + \frac{1}{2}[n_1 \exp(iKx) + cc] \quad (3.9)$$

$$J = J_0 + \frac{1}{2}[J_1 \exp(iKx) + cc] \quad (3.10)$$

$$E = E_0 + \frac{1}{2}[E_{sc} \exp(iKx) + cc] \quad (3.11)$$

where cc denotes complex conjugate, N_{D0}^+ , n_0 , and J_0 are the coefficients of the fundamental components of the Fourier series, and N_{D1}^+ , n_1 , J_1 , and E_{sc} are the coefficients of the first-order components of the Fourier series.

Substituting Eqs. (3.7)-(3.11) into Eqs. (3.1)-(3.4) a set of differential equations for the first-order coefficients, which are of interest here, can be obtained. With further approximations, the cross products of the two first-order coefficients and the second time derivatives can be neglected, and then the differential equations will contain two kinds of term, the constant terms and terms with the factor $\exp(iKx)$. Compared separately, a set of temporal differential equations will be constructed. The temporal derivative of the space-charge field takes the form:

$$\frac{\partial E_{sc}}{\partial t} = \frac{m(-E_0 + iE_D) - E_{sc} \left(1 + \frac{E_D}{E_Q} + i \frac{E_0}{E_Q} \right)}{\tau_M \left(1 + \frac{E_D}{E_M} + i \frac{E_0}{E_M} \right)} \quad (3.12)$$

where $\tau_M = \frac{\epsilon}{e\mu n_0}$ is the Maxwell dielectric relaxation parameter, $E_D = \frac{KTk_B}{e}$ is the

diffusion field, $E_Q = \frac{eN_A}{\epsilon K}$ is the saturation field, $E_M = \frac{\gamma_R N_A}{\mu K}$, and $n_0 = \frac{sI_0 N_D}{\gamma_R N_A}$. The

partial differential equation (3.12) has the typical solution of:

$$E_{sc} = \frac{m(-E_0 + iE_D)}{\left(1 + \frac{E_D}{E_Q} + i\frac{E_0}{E_Q}\right)} \left\{ 1 - \exp \left[-\frac{\left(1 + \frac{E_D}{E_Q} + i\frac{E_0}{E_Q}\right)}{\tau_M \left(1 + \frac{E_D}{E_M} + i\frac{E_0}{E_M}\right)} t \right] \right\} \quad (3.13)$$

Eq. (3.13) predicts an oscillatory behaviour of the modulus of the space-charge field, and a transient peak is expected^{3.8-3.10}.

3.1.3. Time-Independent Solution for the Space-Charge Field

We consider the steady-state as $t \rightarrow \infty$. In this case Eq. (3.13) yields the following solution for the space-charge field:

$$E_{sc} = \frac{m(-E_0 + iE_D)}{\left(1 + \frac{E_D}{E_Q}\right) + i\left(\frac{E_0}{E_Q}\right)} = |E_{sc}| \exp(i\Phi) \quad (3.14)$$

which is a complex function, with Φ as the phase angle. The real part of the space-charge field presents an in-phase sinusoidal refractive index variation with respect to the sinusoidal light distribution, while the imaginary part represents a $\frac{\pi}{2}$ phase-shifted sinusoidal refractive index variation.

3.1.4. Photo-Induced Refractive Index Modulation

The optical properties of photorefractive materials are described by the refractive index ellipsoid. The initial BSO crystal (in the absence of an applied electric field) is

an optically isotropic crystal, and its refractive index ellipsoid is a sphere and is given in the standard crystallographic coordinate system by:

$$\frac{x^2}{n_0^2} + \frac{y^2}{n_0^2} + \frac{z^2}{n_0^2} = 1 \quad (3.15)$$

where n_0 is the refractive index of the crystal. BSO is a paraelectric electro-optic material. By applying an electric field it becomes birefringent. The photo-induced space-charge field changes the initial refractive index via the linear electro-optic (Pockels) effect, and the change in the refractive index ellipsoid is given by^{3.11-3.13}:

$$\Delta\left(\frac{1}{n^2}\right)_{ij} = \sum_k r_{ijk} (E_{sc})_k \quad (3.16)$$

where $(i, j, k) \rightarrow (x, y, z)$, n is the refractive index, and r_{ijk} are the linear electro-

optic coefficients. The tensor $\left(\frac{1}{n^2}\right)_{ij}$ is symmetric in the subscripts i and j , therefore it has only six independent components. With the convenient notation of $ij, xx \rightarrow 1, yy \rightarrow 2, zz \rightarrow 3, yz \rightarrow 4, zx \rightarrow 5$ and $xy \rightarrow 6$, Eq. (3.16) can be expressed as:

$$\Delta\left(\frac{1}{n^2}\right)_i = \sum_j r_{ij} (E_{sc})_j \quad (3.17)$$

where $i = 1, 2, \dots, 6$ and $j = 1, 2, 3$. Now Eq. (3.15) is modified as the field-induced refractive index ellipsoid, which has the general form:

$$\begin{aligned} & x^2 \left[\frac{1}{n_0^2} + \Delta\left(\frac{1}{n^2}\right)_1 \right] + y^2 \left[\frac{1}{n_0^2} + \Delta\left(\frac{1}{n^2}\right)_2 \right] + z^2 \left[\frac{1}{n_0^2} + \Delta\left(\frac{1}{n^2}\right)_3 \right] \\ & + 2yz \Delta\left(\frac{1}{n^2}\right)_4 + 2zx \Delta\left(\frac{1}{n^2}\right)_5 + 2xy \Delta\left(\frac{1}{n^2}\right)_6 = 1 \end{aligned} \quad (3.18)$$

BSO belongs to the crystallographic class 23 point group symmetry, which has three equal non-zero linear electro-optic coefficients:

$$r_{41} = r_{52} = r_{63} = 5 \text{ pm/V} \quad (3.19)$$

Therefore the components in Eq. (3.17) have the only non-zero values:

$$\Delta\left(\frac{1}{n^2}\right)_4 = r_{41}(E_{sc})_x, \quad \Delta\left(\frac{1}{n^2}\right)_5 = r_{41}(E_{sc})_y, \quad \Delta\left(\frac{1}{n^2}\right)_6 = r_{41}(E_{sc})_z \quad (3.20)$$

Substituting Eqs. (3.20) into Eq. (3.18), we will obtain a simplified expression for the refractive index ellipsoid.

$$x^2 \left[\frac{1}{n_0^2} \right] + y^2 \left[\frac{1}{n_0^2} \right] + z^2 \left[\frac{1}{n_0^2} \right] + 2r_{41}(E_{sc})_x yz + 2r_{41}(E_{sc})_y zx + 2r_{41}(E_{sc})_z xy = 1 \quad (3.21)$$

By geometric coordinate transformation the ellipsoid of Eq. (3.21) can be rewritten in its principal-axis coordinate system:

$$\frac{X'^2}{n_{X'}^2} + \frac{Y'^2}{n_{Y'}^2} + \frac{Z'^2}{n_{Z'}^2} = 1 \quad (3.22)$$

where (X', Y', Z') are the principal-axis based coordinates of the refractive index ellipsoid. Obviously, the orientations and the magnitudes of the principal axes depend on the direction of the space-charge field with respect to the crystallographic axes.

If the crystal orientation is selected such that the incident beam is on the $(\bar{1}10)$ face, and the grating vector and the applied electric field are along $[110]$ crystallographic direction, the sixth term in Eq. (3.21) will vanish $[(E_{sc})_z = 0]$. In this case the principal axes of the refractive index ellipsoid determined by Eq. (3.22) are shown in Fig. 3.2. This arrangement presents maximum refractive index modulation, and the refractive index modulation along the grating direction is given by^{3.14, 3.15}:

$$\Delta n = n_0^3 r_{41} E_{sc} \quad (3.23)$$

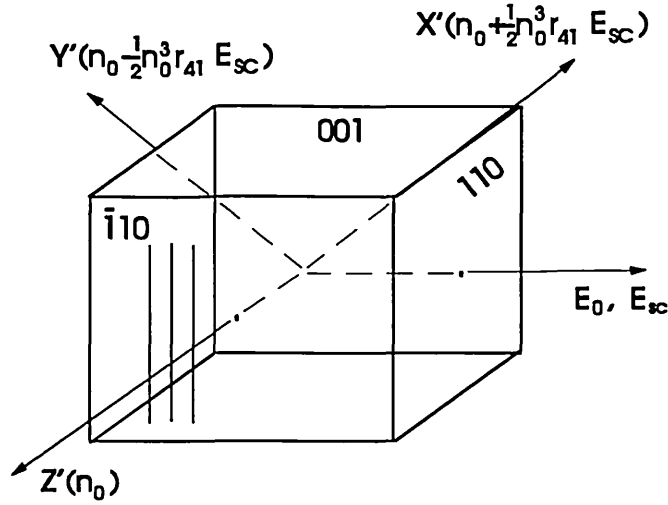


Fig. 3.2. The crystal geometry for maximum diffraction efficiency. X' , Y' , Z' : the principal axes of the refractive index ellipsoid.

If the crystal orientation is selected such that the incident beams are on the $\left(\bar{1}10\right)$ face, and the grating vector and applied electric field are along $[001]$ crystallographic direction, the fourth and the fifth terms in Eq. (3.21) will vanish $\left[\left(E_{sc}\right)_x = \left(E_{sc}\right)_y = 0\right]$. In this case the principal axes of the refractive index ellipsoid are shown in Fig. 3.3. This arrangement results in the strongest beam-coupling, and the refractive index modulation along the grating direction is given by:

$$\Delta n = \frac{1}{2} n_0^3 r_{41} E_{sc} \quad (3.24)$$

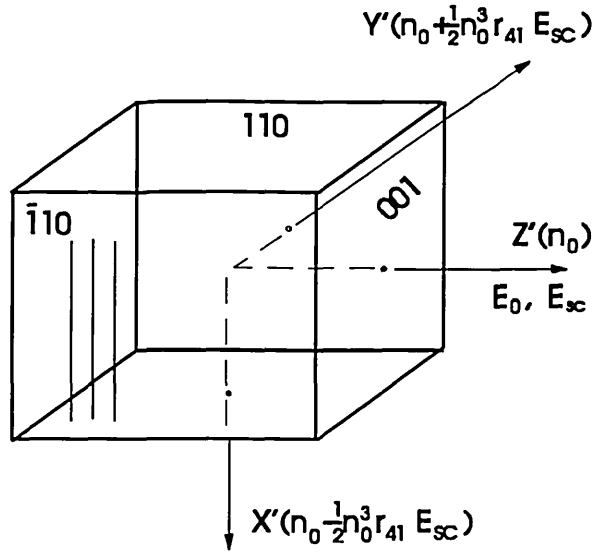


Fig. 3.3. The crystal geometry for maximum energy transfer. X', Y', Z': are the principal axes of the refractive index ellipsoid.

3.2. Diffraction from Volume Refractive Index Gratings

3.2.1. Bragg Diffraction from a Volume Grating

A plane grating can be regarded as a set of periodically spaced transparent slits in an opaque screen. When a plane wave encounters these slits, it is scattered into different directions. Diffraction maxima occur when the scattered components from these slits are in-phase, which allows a constructive addition of these components. Fig. 3.4 shows the geometry for diffraction from a plane grating. Suppose the grating spacing is Λ , the refractive index everywhere is n_0 , the wavelength of the incident wave is λ_0 in air, and the incident angle and diffracted angle of the plane wave are ϑ_0 , and ϑ_L , respectively. The in-phase scattering takes place when the addition of the optical path lengths AB and AC is a whole number of wavelengths, which yields:

$$\sin(\vartheta_0) + \sin(\vartheta_L) = \frac{L\lambda_0}{n_0\Lambda} \quad (3.25)$$

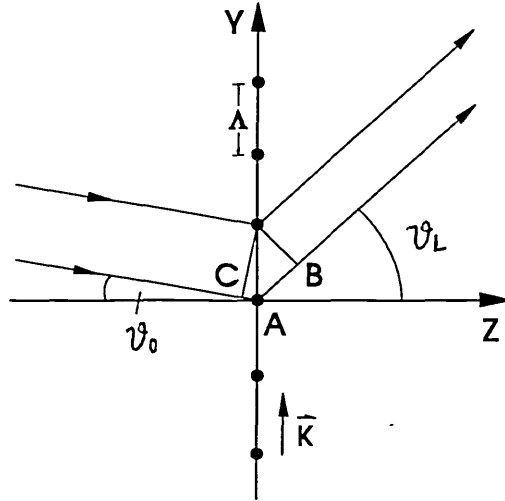


Fig. 3.4 Diffraction from a plane grating.

where L is a integer. Eq. (3.25) shows that the incident angle has no specific restriction, and for a certain incident angle, a set of diffraction maxima with different angles can exist.

For a volume grating, Eq. (3.25) must still be valid. In addition, we must consider the scattering from all points along the same fringe. Fig. 3.5 shows this in a slanted grating with a slant angle ϕ . The in-phase addition of the scattered components from a single fringe occurs when the optical path lengths EF and HG in Fig. 3.5 are equal. This yields a condition:

$$\cos(\vartheta_L - \phi) = \cos(\vartheta_0 + \phi) \quad (3.26)$$

which additionally restricts the diffraction angles to:

$$\vartheta_L = -\vartheta_0 \quad \text{or} \quad \vartheta_L = \vartheta_0 + 2\phi \quad (3.27)$$

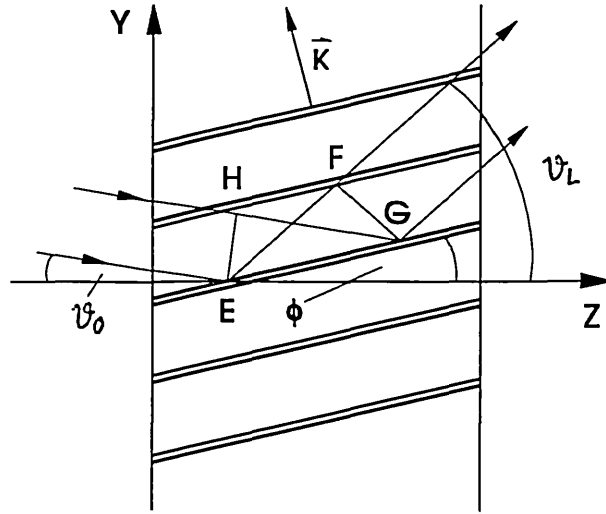


Fig. 3.5 Diffraction from a volume grating.

For the condition of $\vartheta_L = -\vartheta_0$, the solution to Eq. (3.25) is $L = 0$, and only zero-order diffraction is allowed. For the condition of $\vartheta_L = \vartheta_0 + 2\phi$ Eq. (3.25) yields:

$$2\text{Sin}(\vartheta_0 + \phi) = \frac{L\lambda_0}{n_0\Lambda} \quad (3.28)$$

This implies that other diffraction orders can exist at certain specific incident angles, namely the "Bragg" angles. With light incident at the Lth Bragg angle, up to two waves are permitted. These are the zeroth and Lth diffraction orders. With other incident angles, the wave travels through the grating without diffraction. The first diffraction order is allowed when light is incident at the first Bragg angle:

$$2\text{Sin}(\vartheta_0 + \phi) = \frac{\lambda_0}{n_0\Lambda} \quad (3.29)$$

which is the Bragg condition and the incident light is said to be "Bragg-matched" to the grating.

3.2.2. Diffraction Efficiency for a Transmission Grating

Using coupled wave theory, Kogelnik^{3.16} has analyzed the diffraction efficiency of volume gratings in the Bragg regime. In this thesis a slantless transmission grating formed in BSO and readout at the Bragg angle are employed. Therefore we consider here the diffraction efficiency of a slantless transmission grating under the Bragg condition.

Suppose the refractive index variation of a fixed grating is described by:

$$n = n_0 + \frac{\Delta n}{2} \left[\exp(-i\bar{K} \cdot \bar{r}) + cc \right] \quad (3.30)$$

where \bar{r} is the position vector. The incident wave a_i and the diffracted wave a_d can be described by:

$$a_i = R(z) \exp(-i\bar{\rho} \cdot \bar{r}) \quad (3.31)$$

$$a_d = S(z) \exp(-i\bar{\sigma} \cdot \bar{r}) \quad (3.32)$$

where $R(z)$ and $S(z)$ are the complex amplitudes, and $\bar{\rho}$ and $\bar{\sigma}$ are the wave vectors. The coherent sum must satisfy the scalar wave equation:

$$\nabla^2(a_i + a_d) + k^2(a_i + a_d) = 0 \quad (3.33)$$

where k is the propagation constant related to relative dielectric constant and the conductivity of the medium. Substituting Eqs. (3.31) and (3.32) into Eq. (3.33) we can obtain the coupled wave equations. Under the conditions of Bragg matching and assuming a slowly varying approximation for the complex amplitudes, the coupled wave equations take the form:

$$\cos(\vartheta_0) \frac{dR}{dz} + \frac{\alpha}{2} R = -i\chi S \quad (3.34)$$

$$\cos(\vartheta_0) \frac{dS}{dz} + \frac{\alpha}{2} S = -i\chi R \quad (3.35)$$

where α is the average intensity absorption coefficient, and

$$\chi = \frac{\pi\Delta n}{\lambda_0} \quad (3.36)$$

is the coupling constant. The coupled equations (3.34) and (3.35) have the typical solution:

$$R(z) = R_1 \exp(\gamma_1 z) + R_2 \exp(\gamma_2 z) \quad (3.37)$$

$$S(z) = S_1 \exp(\gamma_1 z) + S_2 \exp(\gamma_2 z) \quad (3.38)$$

where

$$\gamma_{1,2} = -\frac{\alpha}{2\cos(\vartheta_0)} \pm \frac{i\chi}{\cos(\vartheta_0)} \quad (3.39)$$

Adopting the following boundary conditions:

$$R(0) = R_1 + R_2 = 1 \quad (3.40)$$

$$S(0) = S_1 + S_2 = 0 \quad (3.41)$$

$$\frac{dS(0)}{dz} = \gamma_1 S_1 + \gamma_2 S_2 \quad (3.42)$$

in Eq. (3.38) we can obtain the diffracted wave at the output of the volume grating:

$$\begin{aligned} S(T) &= -i \exp\left[\frac{-\alpha T}{2\cos(\vartheta_0)}\right] \sin\left[\frac{\pi\Delta n T}{\lambda_0 \cos(\vartheta_0)}\right] \\ &\approx \frac{-i\pi\Delta n T}{\lambda_0 \cos(\vartheta_0)} \exp\left[\frac{-\alpha T}{2\cos(\vartheta_0)}\right] \end{aligned} \quad (3.43)$$

where T is the thickness of the volume grating. The last expression in Eq. (3.43) is valid for small fringe modulations. Considering a volume grating formed in BSO with the crystal orientation set for maximum refractive index modulation (Fig. 3.2), the

complex amplitude of the diffracted wave can be obtained by substituting Eq. (3.23) into Eq. (3.43), yielding:

$$S(T) = \frac{-i\pi n_0^3 \gamma_{41} T E_{sc}}{\lambda_0 \cos(\vartheta_0)} \exp\left[\frac{-\alpha T}{2 \cos(\vartheta_0)}\right] \quad (3.44)$$

We can see that if the space-charge field has no additional phase shift, the diffracted wave will be $-\frac{\pi}{2}$ phase shifted with respect to the incident beam. The diffraction efficiency of the transmission volume grating is then given by:

$$\eta = \frac{|S(T)|^2}{|R(0)|^2} = \left[\frac{\pi n_0^3 \gamma_{41} T}{\lambda_0 \cos(\vartheta_0)}\right]^2 |E_{sc}|^2 \exp\left[\frac{-\alpha T}{\cos(\vartheta_0)}\right] \quad (3.45)$$

It can be seen that the diffraction efficiency is proportional to the square of the modulus of the space-charge field. As the space-charge field is proportional to the fringe modulation [see Eq. (3.14)], the diffraction efficiency is proportional to the square of the fringe modulation.

3.3. Energy Transfer Between Writing Beams in the Steady State

Consider two waves propagating in a photorefractive material in which they create a periodic refractive index modulation, a phase grating. Each wave is then diffracted by the grating and, for an unshifted grating, the diffracted wave has a $-\frac{\pi}{2}$ phase shift with respect to the original wave. If the grating is $\frac{\pi}{2}$ phase shifted, there will be an additional $\pm\frac{\pi}{2}$ phase shift with respect to the diffracted waves. Thus an in phase superposition of waves occurs in one propagation direction, and an anti phase superposition of waves occurs in another propagation direction.

Suppose two waves a_1 and a_2 are described as:

$$a_1 = R(z)\exp(-i\bar{\rho} \cdot \bar{r}) \quad (3.46)$$

$$a_2 = S(z)\exp(-i\bar{\sigma} \cdot \bar{r}) \quad (3.47)$$

where $R(z) = |R(z)|\exp[-i\varphi_1(z)]$ and $S(z) = |S(z)|\exp[-i\varphi_2(z)]$ where $\varphi_1(z)$ and $\varphi_2(z)$ are the phase angles of the complex amplitude. The interference of these waves forms a dynamic refractive index grating. If the dynamic grating is Φ phase shifted with respect to the interference pattern, the refractive index modulation will be described as:

$$n = n_0 + \frac{\Delta n_s}{I_0} \left\{ \exp(-i\Phi)R(z)S^*(z)\exp[-i(\bar{\rho} - \bar{\sigma}) \cdot \bar{r}] + cc \right\} \quad (3.48)$$

where Δn_s is the saturation value of the photo-induced refractive index modulation. The coupled wave equations in (3.34) and (3.35) should now be modified, by taking the phase shift into account, to^{3.17-3.20}:

$$\cos(\vartheta_0) \frac{dR}{dz} + \frac{\alpha}{2} R = -i \exp(-i\Phi) \frac{2\pi\Delta n_s}{\lambda_0} \frac{RS^*S}{I_0} \quad (3.49)$$

$$\cos(\vartheta_0) \frac{dS}{dz} + \frac{\alpha}{2} S = -i \exp(i\Phi) \frac{2\pi\Delta n_s}{\lambda_0} \frac{SR^*R}{I_0} \quad (3.50)$$

The two waves are coupled in both the intensity and the phase according to the grating phase shift angle. By differentiating S and R , substituting them into Eqs. (3.49) and (3.50), separating the real and the imaginary parts, we obtain the differential equations for coupled intensities (the real parts) and coupled phases (the imaginary parts). The coupled intensity equations have the form:

$$\frac{dI_R}{dz} + \frac{\alpha}{\cos(\vartheta_0)} I_R = -\Gamma \frac{I_R I_S}{I_R + I_S} \quad (3.51)$$

$$\frac{dI_S}{dz} + \frac{\alpha}{\cos(\vartheta_0)} I_S = \Gamma \frac{I_R I_S}{I_R + I_S} \quad (3.52)$$

where

$$\Gamma = \frac{4\pi\Delta n_s \sin(\Phi)}{\lambda_0 \cos(\vartheta_0)} \quad (3.53)$$

is the intensity coupling constant. The solution of Eq. (3.52) is given by:

$$I_S(z) = I_S(0) \frac{I_R(0) + I_S(0)}{I_R(0) + I_S(0) \exp(\Gamma z)} \exp\left\{\left[\Gamma - \frac{\alpha}{\cos(\vartheta_0)}\right]z\right\} \quad (3.54)$$

If $I_S(0) \ll I_R(0)$, Eq. (3.54) can be simplified as:

$$I_S(z) = I_S(0) \exp\left\{\left[\Gamma - \frac{\alpha}{\cos(\vartheta_0)}\right]z\right\} \quad (3.55)$$

The signal wave is amplified with an exponential gain proportional to the intensity coupling constant Γ .

The energy transfer between writing beams in a dynamic holographic recording depends on the phase shift between the interference pattern and the grating formed. The "drift" mechanism of charge-carrier migration (under an applied electric field) gives rise to a very small phase shift when the drift length is much smaller than the grating spacing, for which stationary energy transfer is almost forbidden. The "diffusion" mechanism of charge-carrier migration (without an applied electric field)

yields a $\frac{\pi}{2}$ phase shift grating for which stationary energy transfer occurs. However the index modulation by diffusion is low in the high spatial frequency domain (fringe spacings less than $0.5 \mu\text{m}$ ^{3.21, 3.22}), and so the intensity coupling constant Γ is small. Effective energy transfer can be achieved with a photorefractive crystal in the drift recording mode, which has higher index modulation at high spatial frequency, and using the moving grating technique, which yields an additional $\frac{\pi}{2}$ phase shift between the grating and the interference patterns (see chapter 4).

3.4. Transient Energy Transfer Between Writing Beams

Although stationary energy transfer is almost forbidden in a grating formed by the drift mechanism of charge-carrier migration, transient energy transfer during the grating recording could occur. This effect is a consequence of the non stationary phase mismatch between the recorded grating and the interference fringes when the two writing beams are of different intensities^{3.23-3.27}.

Let us consider the coupled phase equation deduced from Eqs. (3.49) and (3.50), which has the form:

$$\frac{d\varphi}{dz} = \gamma \frac{I_R - I_S}{I_R + I_S} \quad (3.56)$$

where $\varphi(z) = \varphi_1(z) - \varphi_2(z)$ is the phase difference between the interacting waves and γ is the phase conversion factor given by:

$$\gamma = \frac{2\pi\Delta n_s \cos(\Phi)}{\lambda_0 \cos(\vartheta_0)} \quad (3.57)$$

It is clear from above equations that when the refractive index grating has a $\frac{\pi}{2}$ phase shift with respect to the interference fringes, Γ is finite and γ is zero. In this case $\frac{d\varphi}{dz} = 0$, but stationary energy transfer occurs. On the other hand, when the index grating is in phase with the interference fringes, γ is finite and Γ is zero. In this case there is no stationary energy transfer, but $\frac{d\varphi}{dz} \neq 0$ provided that the intensities of the writing beams are different, which causes transient energy transfer.

Fig. 3.6 demonstrates the evolution of a dynamic grating during holographic recording, and the following is a qualitative analysis of transient energy transfer. The dashed lines denote bright fringes while the solid lines denote the surfaces of equal phase of the dynamic grating. (a), (b), and (c) represent the initial state, transient state and steady state, respectively.

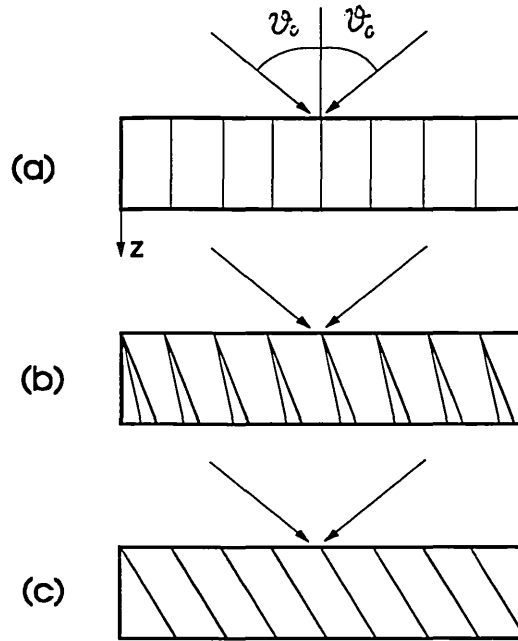


Fig. 3.6. The variation of the dynamic grating during holographic recording.

Suppose two writing beams are incident on the medium with same incident angle ϑ_0 . At $t=0$ there is no grating, and the surfaces of equal phase in the interference pattern lie along the normal to the surface of the nonlinear media i.e. $\frac{\partial\varphi}{\partial z} = 0$ [Fig. 3.6

(a)]. In the stationary case $\frac{\partial\varphi}{\partial z} \neq 0$, according to Eq. (3.56), and the surfaces of equal phase in the interference pattern are inclined relative to their original positions. The equal phase contours of the refractive index grating are coincident with the inclined interference fringes because there is zero phase shift between them in the charge-carrier drifting mode of recording [Fig. 3.6 (c)]. Assume that the recording medium has a finite time response and that the response time is τ . During $0 < t < \tau$, the time mismatch between the writing and the diffraction processes leads to a spatial mismatch between the interference pattern and the recorded refractive index grating [Fig. 3.6 (b)]. Thus transient energy transfer occurs. When $t \gg \tau$ the refractive index grating succeeds in catching up with the inclined stationary interference distribution and the transient energy transfer ceases. It is clear that the following conditions should be satisfied for transient energy transfer: first, the recording medium has a finite response time; second, the intensities of the writing beams are different at the surface of incidence.

The analytical expression for transient energy transfer is given by^{3.23, 3.28}:

$$I_{\pm}(z) - I_{\pm}(0) = \pm(\tau z \Delta)^2 [I_{-}(0) - I_{+}(0)] I_{+}(0) I_{-}(0) \exp\left(\frac{-t}{\tau}\right) \left[\frac{t}{\tau} + \exp\left(\frac{-t}{\tau}\right) - 1 \right] \quad (3.58)$$

where Δ is determined by the ensemble of characteristic parameters of the medium that defines the photorefraction process. It can be seen that the non stationary increment (decrement) of the light intensity is proportional to the square of the thickness z and the response time of the medium τ .

References:

- 3.1. L. Pichon and J.P. Huignard, "Dynamic joint-Fourier-transform correlator by Bragg diffraction in photorefractive $\text{Bi}_{12}\text{SiO}_{20}$ crystal", *Opt. Comm.*, **36** (1981) 277-280.
- 3.2. L. Connors, P. Foote, T. J. Hall, R. Jaura, L.C. Laycock, M.W. McCall and C.R. Petts, "Fidelity of real-time correlation by four-wave mixing", *SPIE*, **492** (1984) 361-369.
- 3.3. J.A. Khoury, G. Hussain and R.W. Eason, "Optical tracking and motion detection using photorefractive $\text{Bi}_{12}\text{SiO}_{20}$ ", *Opt. Comm.*, **71** (1989) 138-144.
- 3.4. C. Soutar, C.M. Cartwright, W.A. Gillespie and Z.Q. Wang, "Tracking novelty filter using transient enhancement of gratings in photorefractive BSO", *Opt. Comm.*, **86** (1991) 155-259.
- 3.5. C. Soutar, Z.Q. Wang, C.M. Cartwright and W.A. Gillespie, "Real-time optical intensity correlator using photorefractive BSO and a liquid crystal television", *J. Mod. Opt.*, **39** (1992) 761-769.
- 3.6. N.V. Kukhtarev, V.B. Markov, S.G. Odulov, M.S. Soskin and V.L. Vinetskii, "Holographic storage in electrooptic crystals. I. steady state", *Ferroelectrics*, **22** (1979) 949-960.

- 3.7. Ph. Refregier, L. Solymar, H. Rajbenbach and J.P. Huignard, "Two-beam coupling in photorefractive $\text{Bi}_{12}\text{SiO}_{20}$ crystals with moving grating: theory and experiments", *J. Appl. Phys.*, **58** (1985) 45-57.
- 3.8. T.J. Hall, R. Jaura, L.M. Conners and P.D. Foote, "The photorefractive effect - a review", *Prog. Quant. Electr.*, **10** (1985) 77-146.
- 3.9. J.M.C. Jonathan, R.W. Hellwarth and G. Roosen, "Effect of applied field on the build-up and decay of photorefractive gratings", *IEEE J. Quant. Electr.*, **QE-22** (1986) 1936-1941.
- 3.10. J.P. Partanen, J.M.C. Jonathan and R.W. Hellwarth, "Direct determination of electron mobility in photorefractive $\text{Bi}_{12}\text{SiO}_{20}$ by a holographic time-of-flight technique", *Appl. Phys. Lett.*, **57** (1990) 2404-2406.
- 3.11. P. Günter and J.P. Huignard, "Photorefractive Materials and Their Applications I", Chapter 2, Springer-Verlag, Berlin, 1988.
- 3.12. R.W. Boyd, "Nonlinear Optics", Chapter 10, Academic Press Limited, London, 1992.
- 3.13. P.K. Das, "Optical Information Processing", Chapter 2, Springer-Verlag, Berlin, 1990.
- 3.14. P. Günter, "Holography, coherent light amplification and optical phase conjugation with photorefractive materials", *Phys. Reports*, **93**, (1982) 199-299.
- 3.15. P. Pellat-Finet, "Measurement of the electro-optic coefficient of BSO crystals", *Opt. Comm.*, **50** (1984) 275-280.
- 3.16. H. Kogelnik, "Coupled wave theory for thick hologram gratings", *Bell. Syst. Tech. J.*, **48** (1969) 2909-2946.
- 3.17. P. Günter, "Electro-Optic and Photorefractive Materials", Part 4, Springer-Verlag, Berlin, 1989.

- 3.18. J.P. Huignard and A. Marrakchi, "Coherent signal beam amplification in two-wave mixing experiments with photorefractive $\text{Bi}_{12}\text{SiO}_{20}$ crystals", *Opt. Comm.*, **38** (1981) 249-254.
- 3.19. P. Günter and J.P. Huignard, "Photorefractive Materials and Their Applications II", Chapter 4, Springer-Verlag, Berlin, 1989.
- 3.20. M.P. Petrov, S.I. Stepanov and A.V. Khomenko, "Photorefractive Crystals in Coherent Optical Systems", Chapter 6, Springer-Verlag, Berlin, 1991.
- 3.21. A. Marrakchi, J.P. Huignard and P. Günter, "Diffraction efficiency and energy transfer in two-wave mixing experiments with $\text{Bi}_{12}\text{SiO}_{20}$ crystal", *Appl. Phys.*, **24** (1981) 131-138.
- 3.22. J.P. Huignard, J.P. Herriau, G. Rivet and P. Günter, "Phase-conjugation and spatial-frequency dependence of wave-front reflectivity in $\text{Bi}_{12}\text{SiO}_{20}$ crystals", *Opt. Lett.*, **5** (1980) 102-104.
- 3.23. V.L. Vinetskii, N.V. Kukhtarev, S.G. Odulov and M.S. Soskin, "Dynamic self-diffraction of coherent light beams", *Sov. Phys. Usp.*, **22** (1979) 742-756.
- 3.24. P. Günter, "Transient energy transfer between writing beams during hologram formation in $\text{Bi}_{12}\text{GeO}_{20}$ ", *Opt. Comm.*, **41** (1982) 83-88.
- 3.25. S.-K. Kwong, Y. Tamita and A. Yariv, "Optical tracking filter using transient energy coupling", *J. Opt. Soc. Am. B*, **5** (1988) 1788-1791.
- 3.26. L. Solymar and J.M. Heaton, "Transient energy transfer in photorefractive materials; an analytic solution", *Opt. Comm.*, **51** (1984) 76-78.
- 3.27. J.M. Heaton and L. Solymar, "Transient energy transfer during hologram formation in photorefractive crystals", *Opt. Acta*, **32** (1985) 397-408.
- 3.28. N.V. Kukhtarev, V.B. Markov and S.G. Odulov, "Transient energy transfer during hologram formation in LiNbO_3 in external electric field", *Opt. Comm.*, **23** (1977) 338-343.

Chapter 4. Properties of Moving Gratings in BSO at Large Fringe Modulations

4.1. Introduction

The phenomenon of energy transfer in BSO is useful for signal amplification in two-wave mixing and four-wave mixing, and has been widely investigated in the last decade^{3,18, 4.1-4.5}. In particular, Refregier et al.^{3,7} have solved the differential equations and presented an expression for the space-charge field with a moving grating in the case of small fringe modulations. But in the case of holographic recording for correlation purposes, the fringe modulation is usually large and the small modulation theory should be modified.

For the large fringe modulation case, Au and Solymar^{4,6, 4.7}, and Vachss and Hesselink^{4,8} have presented numerical solutions of the differential equations by taking the higher order harmonic components of the space-charge field into account. Recently Brost^{4,9} has provided a more detailed numerical study of this topic. Their analysis predicts unexpected behaviour at large fringe modulations in the form of nonlinearities.

This chapter presents the experimental results made with moving gratings in BSO at large fringe modulations, which are then compared with the numerical results. The highly nonlinear dependence of the optimum fringe velocity and the enhancement of the diffraction efficiency on the fringe modulation is experimentally verified. This work is complementary to that previously reported on experimental measurements at small fringe modulations, and to the numerical results for large fringe modulations.

4.2 Theory of a Moving Grating at Small Fringe Modulation

In the case of a moving grating, the variables in Kukhtarev's differential equations should have the same form, to a first order approximation, as in Eqs.(3.7)-(3.11) but replacing " $\exp(iKx)$ " by " $\exp[iK(x - vt)]$ " i.e.:

$$I = I_0 + \frac{1}{2} \{ I_0 m \exp[iK(x - vt)] + cc \} \quad (4.1)$$

$$N_D^+ = N_{D0}^+ + \frac{1}{2} \{ N_{D1}^+ \exp[iK(x - vt)] + cc \} \quad (4.2)$$

$$n = n_0 + \frac{1}{2} \{ n_1 \exp[iK(x - vt)] + cc \} \quad (4.3)$$

$$J = J_0 + \frac{1}{2} \{ J_1 \exp[iK(x - vt)] + cc \} \quad (4.4)$$

$$E = E_0 + \frac{1}{2} \{ E_{sc} \exp[iK(x - vt)] + cc \} \quad (4.5)$$

where v is the fringe velocity. Substituting the Eqs. (4.1)-(4.5) into the Kukhtarev equations, a set of differential equations for the first-order coefficients can be obtained. With the same approximation as in section 3.1.2, the differential equations will contain constant terms and terms with factor $\exp[iK(x - vt)]$. Comparing them separately and

considering the space-charge field at steady state only i.e. $\frac{\partial E_{sc}}{\partial t} = 0$, we will obtain the expression^{3.7}:

$$E_{sc} = \frac{-m(E_D + iE_0)}{-\frac{E_0}{E_Q} + Kv\tau_M \left(1 + \frac{E_D}{E_M}\right) + i \left(1 + \frac{E_D}{E_Q} + Kv\tau_M \frac{E_0}{E_M}\right)} \quad (4.6)$$

where all parameters are as described in Eq. (3.12). When diffusion is negligible (with $E_D = 0$), Eq. (4.6) can be simplified, and the modulus of the space-charge field can be expressed as:

$$|E_{sc}| = \frac{mE_0}{\left[\left(Kv\tau_M - \frac{E_0}{E_Q} \right)^2 + \left(1 + Kv\tau_M \frac{E_0}{E_M} \right)^2 \right]^{\frac{1}{2}}} \quad (4.7)$$

It is obvious from Eq. (4.7) that there is an optimum fringe velocity v_{opt} which makes the modulus of the space-charge field a maximum. v_{opt} can be obtained by differentiating Eq. (4.7) with respect to v . With the condition $E_Q \gg E_M$, (E_M is typically less than 2 % of E_Q in BSO), we have:

$$v_{\text{opt}} = \frac{-E_M E_0}{K\tau_M(E_M^2 + E_0^2)} \quad (4.8)$$

Substituting Eq. (4.8) into Eq. (4.7) we can obtain the modulus of the space-charge field with a moving grating at optimum fringe velocity. According to Eq. (3.45) the diffraction efficiency η of a phase grating is proportional to the square of the modulus of the space-charge field. We define the enhancement of the diffraction efficiency, G , as the ratio of the diffraction efficiency when the grating moves with the optimum fringe velocity to that when the grating is stationary. It is given by:

$$G = \frac{\eta_{\text{at optimum velocity}}}{\eta_{\text{at zero velocity}}} = \left(\frac{|E_{\text{sc}}|_{\text{at optimum velocity}}}{|E_{\text{sc}}|_{\text{at zero velocity}}} \right)^2 \quad (4.9)$$

$$= \frac{E_0^4 E_Q^2}{E_0^2(E_0^2 + E_Q E_M)^2 + E_M^4 E_Q^2}$$

E_Q and E_M are proportional to the fringe spacing [see Eq. (3.12)]. By differentiating Eq. (4.9) with respect to E_0 , we can obtain the relationship between E_0 , E_Q and E_M for the maximum enhancement of the diffraction efficiency. With the further assumption that $E_0 \gg E_M$, this relationship can be expressed as:

$$E_0^2 = E_Q E_M \quad (4.10)$$

which corresponds to an optimum fringe spacing:

$$\Lambda_{\text{opt}} = \frac{2\pi E_0}{N_A} \left(\frac{\epsilon\mu}{e\gamma_R} \right)^{\frac{1}{2}} \quad (4.11)$$

Eqs. (4.8), (4.9) and (4.11) present the theoretical expressions for the optimum fringe velocity, the enhancement of the diffraction efficiency and the optimum fringe spacing of the moving grating, respectively. These inferences are valid under the condition of small fringe modulation. We will see, by experimental investigation, that Eq. (4.11) still gives a quite accurate result for the optimum fringe spacing at large fringe modulation, however, Eqs. (4.8) and (4.9) do not. The optimum fringe velocity and the enhancement of the diffraction efficiency exhibit strong modulation dependence at large fringe modulations. Therefore a further analysis is required.

4.3 Numerical Results for a Moving Grating at Large Fringe Modulations

At small fringe modulations the higher Fourier harmonics of the variables in Kukhtarev's differential equations are assumed to be much smaller than the first-order components and can be neglected. At large fringe modulation, the higher harmonics may be very strong and must be taken into account. In this case the intensity distribution of the interference pattern in Eq. (4.1) remains unchanged, but Eqs. (4.2)-(4.5) should be rewritten as:

$$N_D^+ = N_{D0}^+ + \frac{1}{2} \sum_{r=1}^{\infty} \{N_{Dr}^+ \exp[irK(x - vt)] + cc\} \quad (4.12)$$

$$n = n_0 + \frac{1}{2} \sum_{r=1}^{\infty} \{n_r \exp[irK(x - vt)] + cc\} \quad (4.13)$$

$$J = J_0 + \frac{1}{2} \sum_{r=1}^{\infty} \{J_r \exp[irK(x - vt)] + cc\} \quad (4.14)$$

$$E = E_0 + \frac{1}{2} \sum_{r=1}^{\infty} \{E_r \exp[irK(x - vt)] + cc\} \quad (4.15)$$

where N_{Dr}^+ , n_r , J_r and E_r are the r th Fourier components of these variables. Obviously, with the above expressions there is no analytic solution to the differential equations, but Au and Solymar^{4.6, 4.7} have provided numerical results. The computed data of the normalized space-charge field divided by the fringe modulation (E_{sc}/m) are plotted in reference 4.6, where the space-charge field is expressed by w_1 . Fig. 4.1 shows this figure.

Fig. 4.1. The variations of E_{sc}/m (w_1/m in the figure) with fringe modulation m and frequency detuning y in the complex plane (ref. 4.6).

From this figure we can draw some conclusions which are of interest here:

1. The $m = 0.01$ curve is practically indistinguishable from those for small fringe modulation, and the $m = 0.1$ curve is close to the $m = 0.01$ curve i.e. as the fringe modulation increases from $m = 0.01$ to $m = 0.1$, the maximum (E_{sc}/m) decreases slowly. The $m = 0.3, 0.6$ and 0.9 curves show large deviations from the $m = 0.01$ curve, and the larger the m value is, the bigger the rate of the deviation, i.e. as the modulation increases further, the maximum (E_{sc}/m) decreases rapidly. As a consequence, the square power dependence of the diffraction efficiency on the fringe modulation is no longer valid. On the other hand, (E_{sc}/m) is approximately constant in the case of a stationary grating. Therefore the variations of the maximum (E_{sc}/m) value with the fringe modulation indicate that the enhancement of the diffraction efficiency is nonlinearly dependent on the fringe modulation.

2. As the fringe modulation increases from $m = 0.01$, the curves become flatter and flatter, and the peak value of (E_{sc}/m) shifts to the right. This indicates that as the fringe modulation increases the optimum fringe velocity (implied by the parameter y) increases. When the fringe modulation reaches 0.6 the curve becomes complicated, implying a more complicated behaviour for the optimum fringe velocity.

Brost^{4,9} has provided a more detailed numerical study for the large fringe modulation case. Figs. 4.2, 4.3 and 4.4 show the numerical results for the modulus of the space-charge field versus the relative fringe velocity obtained by Brost. The relative fringe velocity is defined as the ratio of the fringe velocity to the optimum

fringe velocity at small fringe modulation $\left(\frac{v}{v_{opt}}\right)$, v_{opt} here refers in particular to the case of small fringes modulation. These figures correspond to fringe modulations 0.2, 0.6 and 0.9, respectively. The grating recording condition is assumed such that the applied electric field is 5kV/cm and the grating spacing is 20 μ m.

We can see that the curve for $m = 0.2$ (Fig. 4.2) has a single peak at the relative fringe velocity 1.03, which shows that as the fringe modulation increases the optimum fringe velocity increases as well. The characteristics of this curve are very similar to that at small fringe modulation, showing peak enhancement of the space-charge field at $v \approx v_{opt}$.

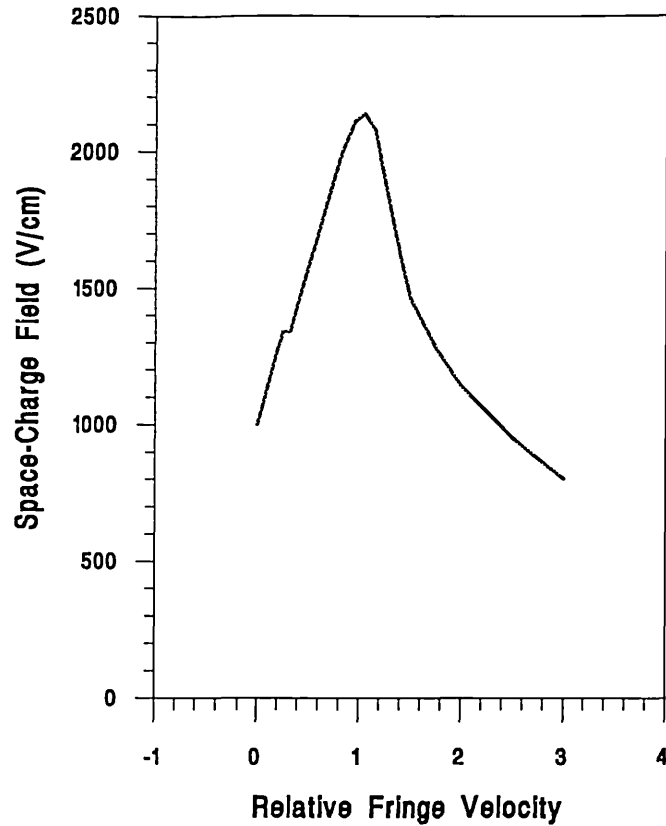


Fig. 4.2. The space-charge field versus the fringe velocity at $m = 0.2$ (ref. 4.9).

The curve for $m = 0.6$ (Fig. 4.3) is more complicated. There are now two peaks for the space-charge field. One is at higher fringe velocity, $\frac{v}{v_{opt}} = 1.38$, and another is at lower fringe velocity, $\frac{v}{v_{opt}} = 0.2$. The higher velocity peak can be regarded as a shift of the peak from the curve $m = 0.2$ as expected. The lower velocity peak, however, has little relation to the curve $m = 0.2$, and is apparently a characteristic of large fringe modulations.

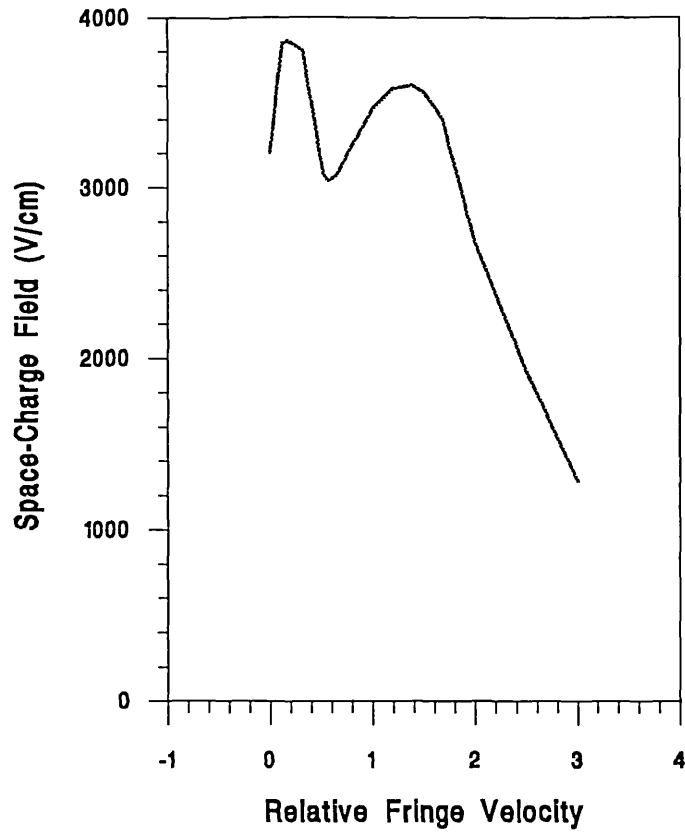


Fig. 4.3. The space-charge field versus the fringe velocity at $m = 0.6$ (ref. 4.9).

The $m = 0.9$ curve (Fig. 4.4) also has two peaks for the space-charge field, being at $\frac{v}{v_{opt}} = 1.5$ and 0.05 , respectively. They can be regarded as a high velocity shift and a low velocity shift with respect to the peaks in the $m = 0.6$ curve. However the peak at high fringe velocity becomes less distinct, implying that the peak associated with small fringe modulations deteriorates at large modulations.

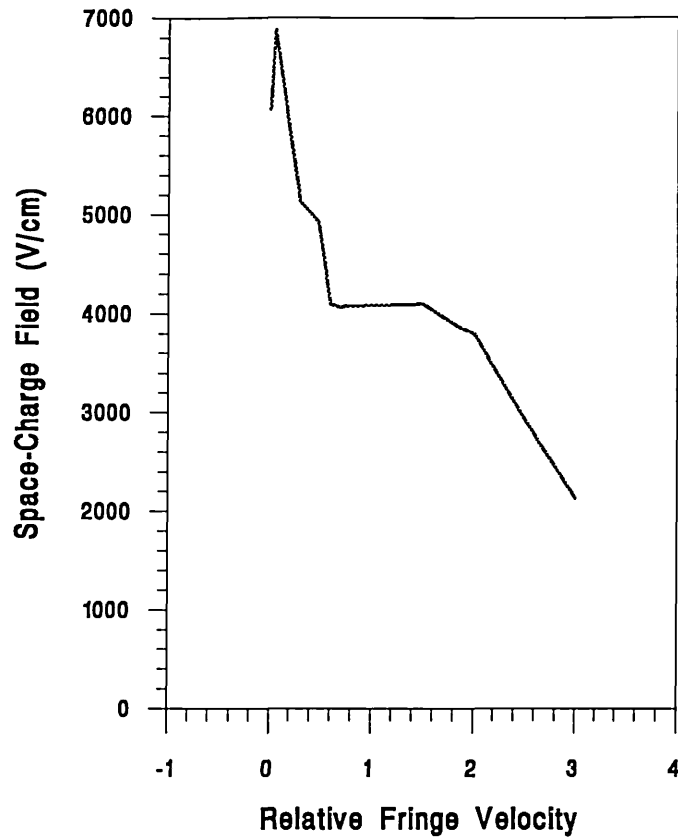


Fig. 4.4. The space-charge field versus the fringe velocity at $m = 0.9$ (ref. 4.9).

From these Figures we can also calculate the enhancement of the diffraction efficiency for different fringe modulations, and make a comparison. They are $G = 4.51, 1.37$ and 1.23 for the fringe modulations of $0.2, 0.6,$ and $0.9,$ respectively. We can see that as the fringe modulation increases the enhancement of the diffraction efficiency decreases rapidly exhibiting nonlinear characteristics.

4.4. Experiments

4.4.1 Experimental Configuration

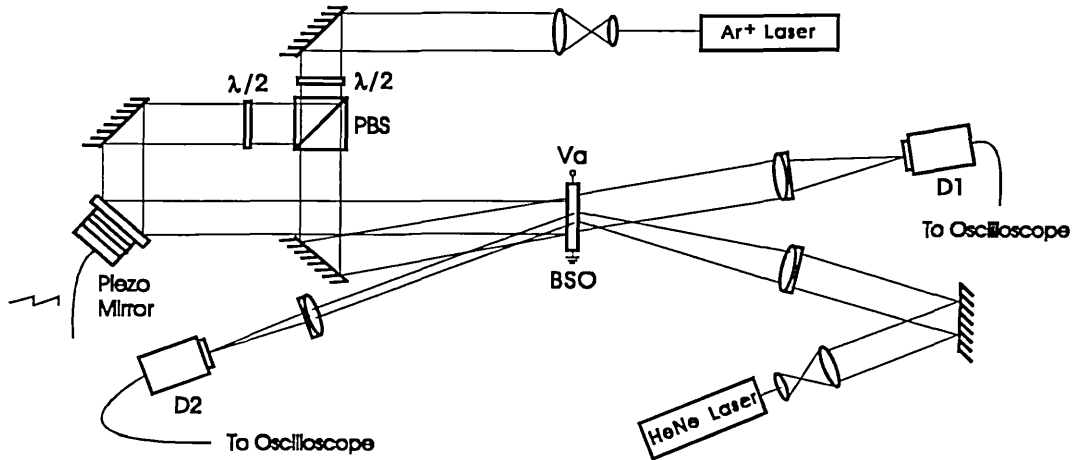


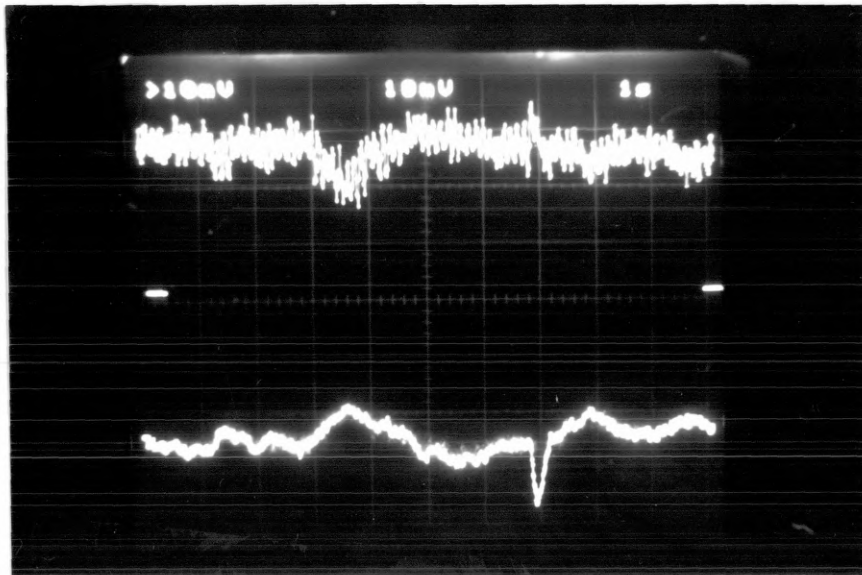
Fig. 4.5 The experimental system for simultaneously measuring the diffraction efficiency and the energy transfer of the dynamic grating recorded in a BSO crystal.

The experimental system is shown in Fig. 4.5. The BSO crystal had dimensions $10 \times 8 \times 2 \text{ mm}^3$. The orientation of the crystal with respect to the applied electric field and the writing beams was arranged as in Fig. 3.2 to obtain the maximum diffraction efficiency. The argon ion laser was operated at $\lambda = 514.5 \text{ nm}$, expanded and collimated to 15 mm in diameter. The polarizing beam splitter (PBS) was used to divide the argon laser beam into two beams, whose ratio can be adjusted by rotating the first $\frac{\lambda}{2}$ plate. By rotating the second $\frac{\lambda}{2}$ plate the polarization directions of the beams are kept parallel. A piezomirror was used to obtain a frequency detuning of the reference beam. The He-Ne laser was used as a reading beam. Detector D1 measured the transmitted intensity of one of the writing beams which corresponds to the imaginary part of the space-charge field, while D2 measured the diffracted intensity of the reading beam which corresponds to the modulus of the space-charge field. Both signals were sent to a digital oscilloscope to simultaneously monitor the variations in the components of the space-charge field.

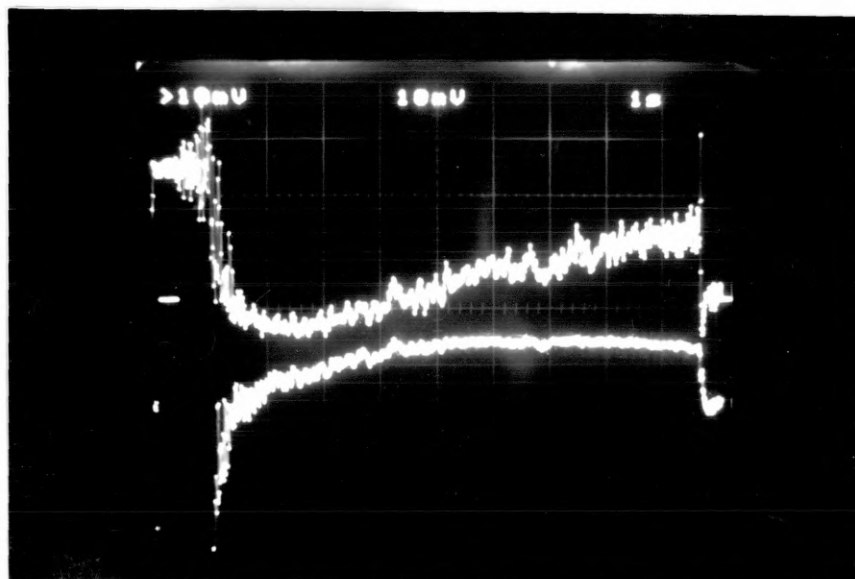
4.4.2 Resonant Effect of a Moving Grating

Fig. 4.6 shows the resonant enhancement of the space-charge field by a moving grating. The grating recording conditions are $\Lambda = 10 \mu\text{m}$ (we will see later that this is near to the optimum fringe spacing), $E_0 = 6.25 \text{ kV/cm}$, $I_0 = 5 \text{ mW/cm}^2$, and $m = 0.94$. The upper trace shows the transmitted argon beam, while the bottom trace shows the diffracted He-Ne beam. The time base is set to be 1s/division , and the traces correspond to a single scanning period.

Fig. 4.6 (a) is the case without a moving grating. It is clear that the traces fluctuate randomly. It is found that this fluctuation is almost inevitable even if in a quiet environment. Fig. 4.6 (b) is the case with a moving grating at optimum fringe velocity. The transmitted Ar^+ beam decreases and reaches its minimum value (maximum energy loss) while the diffracted He-Ne beam increases and reaches its maximum value. It can be seen that the trace of the diffracted beam in (b) is much higher than that in (a), indicating that enhancement of the diffraction efficiency is achieved by a moving grating. It also can be seen that the trace of the diffracted beam in (b) is much more stable, showing that moving the grating has the effect of suppressing random fluctuations.

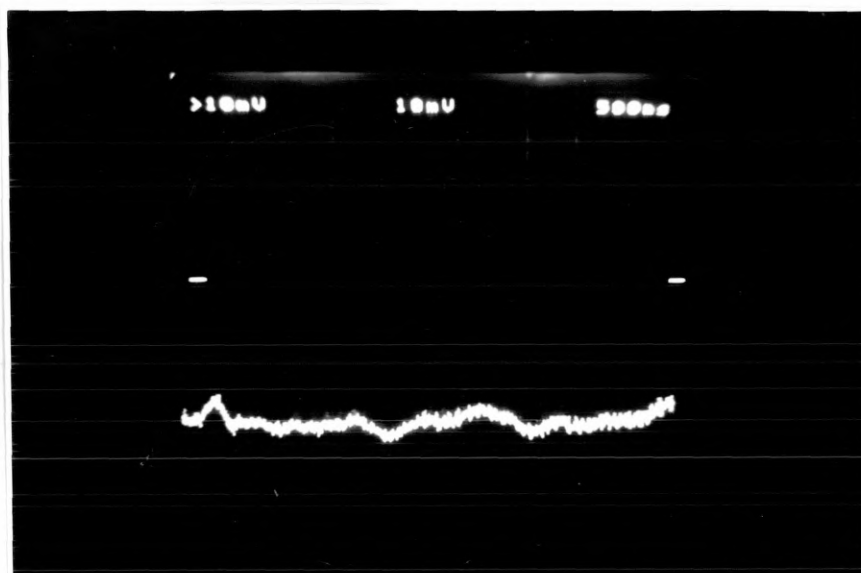


(a) without moving grating

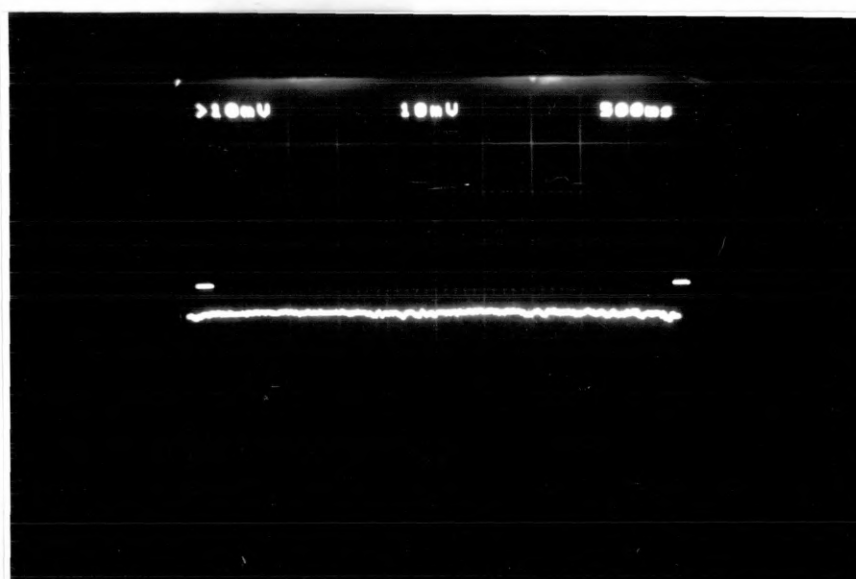


(b) with moving grating at optimum fringe velocity

Fig. 4.6. Temporal responses of the transmitted Ar^+ beam (the upper trace) and the diffracted He-Ne beam (the bottom trace) with a time scale of 1 s/division.



(a) without moving grating



(b) with moving grating at optimum fringe velocity

Fig. 4.7. Temporal responses of the diffracted He-Ne beam with a time scale of 500 ms/division.

To show the resonant enhancement in the diffracted light more clearly, Fig. 4.7 presents the traces of the diffracted signal with a faster time base of the oscilloscope (500ms/division). (a) is the case without a moving grating and (b) is the case with a moving grating.

The effect of suppressing random fluctuations by moving the grating could be explained as follows: Any environmental fluctuations will affect a dynamic grating and cause a transient energy transfer, resulting in unstable grating diffraction. With the grating moving at the optimum fringe velocity, a $\frac{\pi}{2}$ phase shift between the grating and the interference pattern is achieved. Whilst it brings about the highest stationary energy transfer due to the intensity coupling constant Γ in Eqs.(3.51) and (3.52) becoming a maximum, the transient energy transfer is suppressed due to the phase conversion factor γ in Eq. (3.56) becoming zero. Thus a moving grating has the effect of enhancing the diffraction efficiency as well as eliminating the influence of environmental fluctuations.

4.4.3 Dependence of the Optimum Fringe Velocity on the Fringe Modulation

The velocity of the moving grating caused by the scanning piezomirror is determined by the relationship:

$$v = \frac{2\kappa U_M \Lambda \cos(\vartheta_0)}{\lambda t} \quad (4.16)$$

where U_M is the peak amplitude of the sawtooth voltage applied to the piezomirror, κ is the elongation of the stack of the piezo for unity voltage, ϑ_0 is the incident angle of the beam to the piezomirror and t is the scanning period of the sawtooth voltage.

In our investigation, the actual optimum fringe velocity will be compared with the theoretical calculations. For this purpose, we assume that the optimum fringe velocity at $m = 0.1$ is close to that at small fringe modulation, which can be calculated with Eq. (4.8), and choose the constants in the theoretical formulas, s , N_A , N_D , μ , γ_R and ϵ to be those given in reference 4.6, i.e. $s = 2 \times 10^{-5} \text{ m}^2 \text{ J}^{-1}$, $N_A = 10^{22} \text{ m}^{-3}$, $N_D = 10^{25} \text{ m}^{-3}$, $\epsilon = 56 \epsilon_0$, $\mu = 0.3 \times 10^{-5} \text{ m}^2 \text{ V}^{-1} \text{ sec}^{-1}$, and $\gamma = 1.6 \times 10^{-17} \text{ m}^3 \text{ sec}^{-1}$.

Fig 4.8 shows the dependence of the optimum fringe velocity on the fringe modulation. The adopted grating recording conditions are $E_0 = 6.25 \text{ kV/cm}$, $I_0 = 25 \text{ m W/cm}^2$, and $\Lambda = 20 \text{ }\mu\text{m}$.

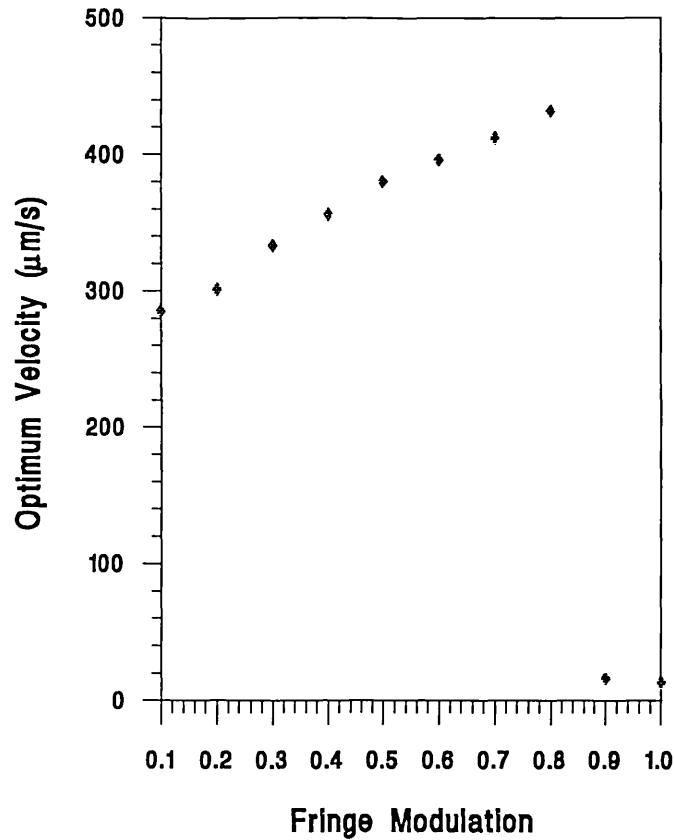


Fig. 4.8. The experimental results of the optimum fringe velocity versus the fringe modulation.

At small fringe modulation ($m = 0.1$), the optimum fringe velocity was experimentally measured to be $290 \pm 10 \text{ }\mu\text{m/s}$. According to Eq. (4.8), it should be $262 \text{ }\mu\text{m/s}$. Considering that the material parameters vary slightly with different specimens, this difference is probably not significant.

At large fringe modulations, we can see that as the fringe modulation increases the optimum fringe velocity increases as well. At a fringe modulation of $m = 0.2$, the optimum fringe velocity is 1.03 times that at $m = 0.1$ i.e. small fringe modulation. At a fringe modulation of $m = 0.6$, the optimum fringe velocity is 1.39 times. At a fringe modulation of $m = 0.9$ there are two fringe velocities which yield peaks in the

diffraction efficiency. One is at a higher velocity, 1.5 times the $m = 0.1$ figure; another is at a much lower velocity, 0.055 in relative units. These are compared with the numerical results in Figs. 4.2-4.4, and they are presented in table 4.1. It can be seen that they are in good agreement except for the lower velocity peak in Fig. 4.3 (0.2 in relative units). This peak was not observed in our experiments.

Table 4.1. Numerical and experimental results of fringe velocity at peaks of space-charge field.

m	$(v/v_{opt})_{\text{peak 1}}$		$(v/v_{opt})_{\text{peak 2}}$	
	Num.	Exp.	Num.	Exp.
0.2	1.03	1.03	—	—
0.6	1.38	1.39	0.2	—
0.9	1.5	1.5	0.05	0.055

Key: Num. denotes numerical results, Exp. denotes experimental results.

We are also interested in the situation with a fringe modulation of $m = 1$. Experiments show that the optimum fringe velocity is very low and well determined to be only 0.045 in relative units. The optimum fringe velocity drops abruptly from a high to a low value as the fringe modulation approaches unity. Thus a sudden drop in the optimum fringe velocity appears.

The variation of the optimum fringe velocity with the fringe modulation in Fig. 4.8 can be summarized as follows: as the fringe modulation increases, the optimum fringe velocity increases as well; then a sub-optimum fringe velocity (yielding another peak of the diffraction efficiency) appears at a low fringe velocity; as the fringe modulation increases further, the optimum and sub-optimum fringe velocities increase and decrease, respectively; as the fringe modulation approaches unity the peak of the diffraction efficiency at high velocities disappears, and a sudden drop in the optimum fringe velocity occurs.

4.4.4 Nonlinear Enhancement of The Diffraction Efficiency

Fig. 4.9 shows the enhancement of the diffraction efficiency by a moving grating, as a function of the ratio of intensities of the writing beams. The adopted grating recording conditions are $I_0 = 5\text{mW/cm}^2$, and $E_0 = 6.25\text{kV/cm}$. Three curves correspond to fringe spacings of $30\ \mu\text{m}$, $20\ \mu\text{m}$ and $10\ \mu\text{m}$ respectively. According to Eq. (4.11), the optimum fringe spacing should be $\Lambda = 9.46\ \mu\text{m}$. Therefore we expected that $\Lambda = 10\ \mu\text{m}$ would yield the highest enhancement.

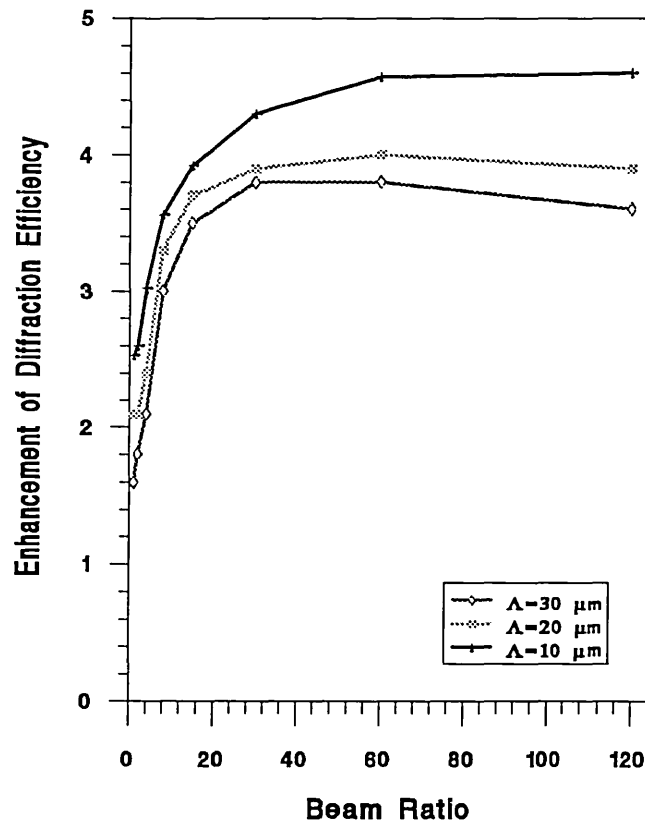


Fig. 4.9. The experimental results of the enhancement of the diffraction efficiency at optimum fringe velocity versus the beam ratio.

We can see from Fig. 4.9 that when the beam ratio is 1, corresponding to a fringe modulation of 1, a 1.6, 2.1 and 2.5 times enhancement of the diffraction efficiency for different fringe spacings is achieved. As the beam ratio increases the enhancement of the diffraction efficiency increases rapidly at the initial stage, and then it increases

smoothly. This phenomenon is qualitatively predicted by Au and Solymar's numerical results.

In comparison with Brost's numerical results, choosing the $\Lambda = 20 \mu\text{m}$ experimental curve for coincidence with the numerical results, we can see that when the beam ratio is 2.5, corresponding to a fringe modulation of 0.9, the enhancement of the diffraction efficiency is 2.2, which is higher than that given in Fig. 4.4. When the beam ratio is 9, corresponding to a fringe modulation of 0.6, the enhancement of the diffraction efficiency is 3.4, which is also higher than that given in Fig. 4.3. When the beam ratio is 98, corresponding to a fringe modulation of 0.2, the enhancement of the diffraction efficiency is 4.0, which is comparable with that given in Fig. 4.2. Table 4.2 presents this comparison.

Table 4.2. Comparison in the enhancement of the diffraction efficiency G.

m		0.2	0.6	0.9
G	Num.	4.51	1.37	1.23
	Exp.	4.0	3.4	2.2

Key: Num. denotes numerical results, Exp. denotes experimental results.

Fig. 4.9 also shows that the enhancement of the diffraction efficiency varies with the grating spacing. The $\Lambda = 10 \mu\text{m}$ curve gives the highest enhancement of the diffraction efficiency, as expected. In fact, by measuring the enhancement of the diffraction efficiency we found the optimum fringe spacing to be about $9.4 \mu\text{m}$, in good agreement with Eq. (4.11).

4.4.5 The Influence on the Absolute Diffraction Efficiency

Fig. 4.10 shows the variation of the absolute diffraction efficiency with the fringe modulation. The "Normal" curve is obtained with a stationary grating. We can see that the diffraction efficiency varies approximately as the square of the fringe modulation, which gives a higher quality reconstruction of the recorded image. The

"M.G." curve is obtained with moving grating at optimum fringe velocity. It seems to be approximately linear within the fringe modulation range 0.3 to 0.9.

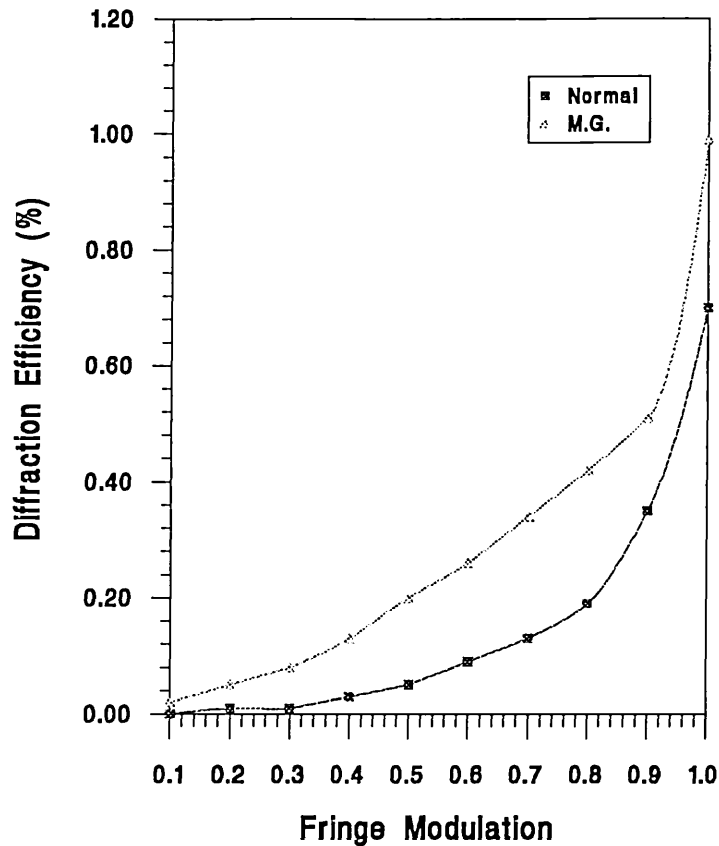


Fig. 4.10. The experimental results of the diffraction efficiency versus the fringe modulation with (M.G.) and without (Normal) moving grating.

Because the intensity distribution of an image on the holographic plane is not uniform and the diffraction efficiency does not vary as the square of the fringe modulation with a moving grating, we can only obtain a reconstructed image which is somewhat distorted from the original image. The distortion becomes more serious in the case of Fourier transform holography, because the Fourier power spectrum of most images varies severely with spatial frequency, and the difference could be several orders in intensity.

4.4.6 The Dependence of the Optimum Fringe Velocity on the Applied Field

From small fringe modulation theory, the optimum fringe velocity is inversely proportional to the applied electric field when $E_0 \gg E_M$ [see Eq. (4.8)]. Fig. 4.11 presents the experimental curve of the optimum velocity versus the inverse applied electric field at large fringe modulation. The adopted recording conditions are $\Lambda = 20 \mu\text{m}$, $I_0 = 5\text{mW/cm}^2$, and $m = 0.94$. The formula of the curve is given by:

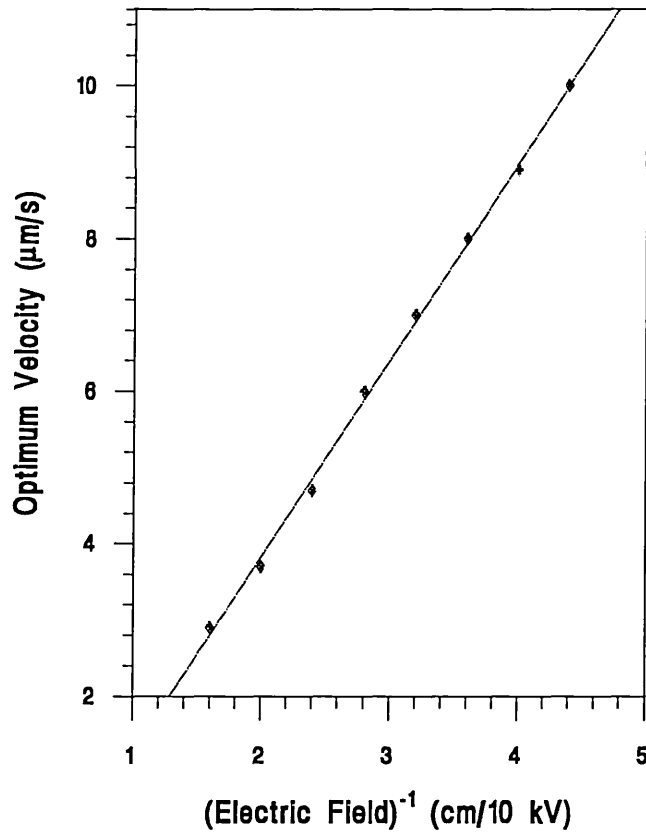


Fig. 4.11. The experimental results of the optimum fringe velocity versus the applied electric field.

$$v_{\text{opt}} = -1.33 + 2.58 \left(\frac{1}{E_0} \right) \quad (4.17)$$

where v_{opt} is in $\mu\text{m/s}$ unit and the inverse electric field $\frac{1}{E_0}$ is in $\text{cm}/10\text{ kV}$ unit. We

can see that the linear relationship between the optimum fringe velocity and the inverse applied electric field is still valid at large fringe modulations. It is not surprising that the optimum fringe velocity is very low in this curve, because the fringe modulation is very high.

4.4.7 The Dependence of the Optimum Fringe Velocity on the Writing Beam Intensity

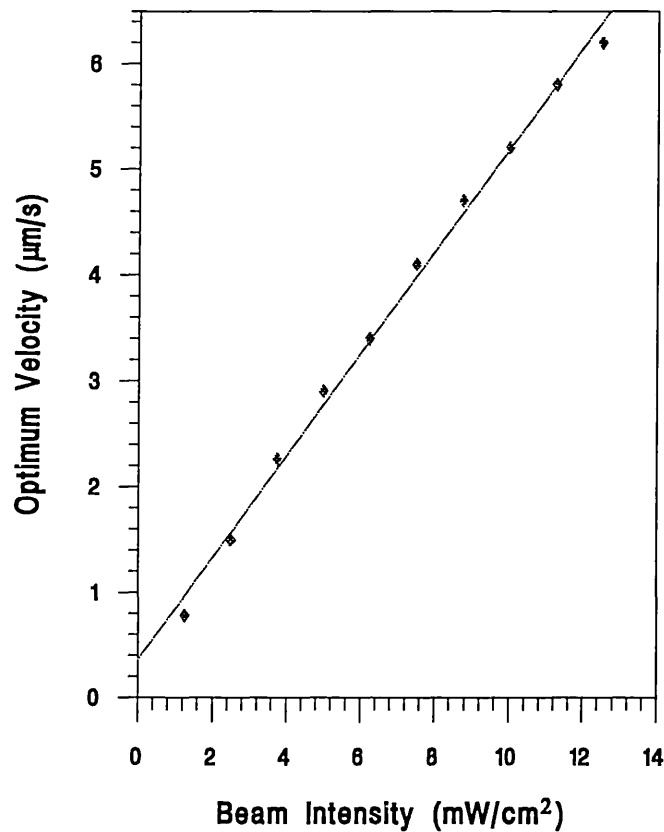


Fig. 4.12. The experimental results of the optimum fringe velocity versus the total beam intensity.

Substituting the expression for τ_M in Eq. (3.12) into Eq. (4.8) we can see that the optimum fringe velocity is proportional to the total incident beam intensity at small fringe modulation. Fig. 4.12 presents the experimental curve of the optimum fringe velocity versus the writing beam intensity at large fringe modulation. The recording

conditions are $\Lambda = 20 \mu\text{m}$, $E_0 = 6.25 \text{ kV/cm}$ and $m = 0.94$. The formula of the curve is given by:

$$v_{\text{opt}} = 0.358 + 0.464 I \quad (4.17)$$

where v_{opt} is again in $\mu\text{m/s}$ unit and the total writing beam intensity I is in mW/cm^2 unit. The linear relationship between the optimum fringe velocity and the total writing beam intensity would appear to be still valid at large fringe modulations.

4.5 Conclusions

From the above experimental results, we can draw a number of conclusions concerning moving gratings at large fringe modulations:

1. The resonance effect of moving gratings in BSO has the effect of suppressing the random fluctuations of the diffracted beam caused by the transient energy transfer between writing beams. This could be explained by the phase conversion factor γ becoming zero. When a $\frac{\pi}{2}$ phase shift between the interference pattern and the dynamic grating takes place, γ has zero value and the transient energy transfer ceases.
2. The optimum fringe velocity not only depends on the applied voltage, fringe spacing and total incident light intensity, which is predicted by small fringe modulation theory, but also depends on the fringe modulation itself. As the fringe modulation increases the optimum fringe velocity increases as well, and then a second peak appears at low fringe velocity. As the fringe modulation increases further the first peak deteriorates and the second peak shifts towards lower fringe velocity.
3. For a particular applied voltage, the enhancement of the diffraction efficiency is fringe-spacing dependent. There is an optimum fringe spacing at which the maximum enhancement can be obtained. The optimum fringe spacing is predicted by the small fringe modulation theory.
4. The enhancement of the diffraction efficiency is also fringe modulation dependent. This causes the reconstructed image to be "distorted". To create a relatively uniform

fringe modulation so as to achieve a less "distorted" reconstruction, Fresnel transforms are preferable in the case of holography with a moving grating.

5. The linear dependence of the optimum fringe velocity on the inverse applied electric field and on the total writing beam intensity based on small fringe modulation theory is still valid at large fringe modulations.

References:

4.1. H. Rajbenbach, J.P. Huignard and B. Loiseaux, "Spatial frequency dependence of the energy transfer in two-wave mixing experiments with BSO crystals", *Opt. Comm.* **48** (1983) 247-252.

4.2. H. Rajbenbach, J.P. Huignard, and Ph. Refregier, "Amplified phase-conjugate beam reflection by four-wave mixing with photorefractive $\text{Bi}_{12}\text{SiO}_{20}$ crystals", *Opt. Lett.*, **9** (1984) 558-560.

4.3. G. Hamel de Monchenault, B. Loiseaux and J.P. Huignard, "Amplification of high bandwidth signals through two-wave mixing in photorefractive $\text{Bi}_{12}\text{SiO}_{20}$ crystals", *Appl. Phys. Lett.*, **50** (1987) 1794-1796.

4.4. S. Mallick, B. Imbert, H. Ducollet, J.P. Herriau and J.P. Huignard, "Generation of spatial subharmonics by two-wave mixing in a nonlinear photorefractive medium", *J. Appl. Phys.*, **63** (1988) 5660-5663.

4.5. G. Hamel de Monchenault and J.P. Huignard, "Two-wave mixing with time modulated signal in $\text{Bi}_{12}\text{SiO}_{20}$ theory and application to homodyne wavefront detection", *J. Appl. Phys.*, **63** (1988) 624- 627.

4.6. L.B. Au and L. Solymar, "Space-charge field in photorefractive materials at large modulation", *Opt. Lett.*, **13** (1988) 660-662.

4.7. L.B. Au and L. Solymar, "Higher harmonic gratings in photorefractive materials at large modulation with moving fringes", *J. Opt. Soc. Am. A*, **7** (1990) 1554-1561.

4.8. F. Vachss and L. Hesselink, "Nonlinear photorefractive response at high modulation depths", *J. Opt. Soc. Am. A*, **5** (1988) 690-701.

4.9. G. A. Brost, "Numerical analysis of the photorefractive response with moving gratings", presented at the Photorefractive Materials, Effects and Devices PRM'93, Kiev, Ukraine, 11-15 August 1993.

Chapter 5. The Effects of Optical Bias on Moving Gratings in BSO at Large Fringe modulation

We have seen that holographic recording in BSO can be enhanced by the moving grating technique. However, the dependence of the optimum fringe velocity on the fringe modulation limits its applications. In fact, we can normally only use a fixed fringe velocity which would be suitable only for a certain range of fringe modulations. The difficulty occurs at fringe modulations close to unity where the optimum fringe velocity decreases two orders of magnitude with respect to that at smaller fringe modulations. With the scanning velocity appropriate to smaller fringe modulations, the diffraction efficiency of the gratings with fringe modulations close to unity drops rapidly. There are two strategies to solve this problem: 1. adjusting the recording beam ratios to avoid fringe modulations close to unity; 2. applying optical bias, e.g. additional uniform white-light illumination, to reduce the actual fringe modulations.

Optical bias has been used to enhance the transient formation of gratings in BSO^{5.1}, and found applications in novelty filtering^{3.4} and intensity correlation^{5.2}. It has been demonstrated that the optical bias has two effects on the transient grating formation: 1. the additional light intensity reduces the fringe modulation, and so reduces the diffraction efficiency at steady state; 2. as the diffraction efficiency at steady state decreases, the ratio of the transient peak to the steady value increases, i.e. transient enhancement is achieved. Correspondingly, we expect that while optical bias overcomes the difficulty of the sudden decrease in the optimum fringe velocity when the fringe modulation is close to unity, it will enhance the diffraction efficiency with a moving grating compared to that with a stationary grating.

In this chapter we presents several experimental results concerning applying optical bias to moving gratings. It is not only a development of the moving grating technique in the way of offering effective control over the optimum fringe velocity, but also reveals a further insight into the fundamental nature of the grating formation in photorefractive materials.

5.1. Analysis

With white-light illumination, the variables of light intensity I and the resulting photoelectron density n in Eqs. (4.1) and (4.3), which are valid at small fringe modulations, should contain a term corresponding to the optical bias, and should be expressed as:

$$I = I_{ob} + I_0 + \frac{1}{2} \{ I_0 m \exp[iK(x - vt)] + cc \} \quad (5.1)$$

$$n = n_{ob} + n_0 + \frac{1}{2} \{ n_1 \exp[iK(x - vt)] + cc \} \quad (5.2)$$

where I_{ob} is the intensity of optical bias and n_{ob} is the number of the photoelectrons generated by optical bias. It is clear that other variables, N_D^+ , J and E in Eqs. (4.2), (4.4) and (4.5) are not affected by optical bias, and the expressions would remain unchanged.

Substituting Eqs. (4.2), (4.4), (4.5) (5.1) and (5.2) into Kukhtarev's differential equations and considering the stationary case only, we will obtain a solution for the space-charge field as:

$$|E_{sc}| = \frac{m' E_0}{\left[\left(Kv\tau_M' - \frac{E_0}{E_Q} \right)^2 + \left(1 + Kv\tau_M' \frac{E_0}{E_M} \right)^2 \right]^{\frac{1}{2}}} \quad (5.3)$$

$$m' = \frac{2(I_1 I_2)^{1/2}}{I_{ob} + I_0} = \frac{m}{(1+k)} \quad (5.4)$$

$$\tau_M' = \frac{\epsilon \gamma_R N_A}{e \mu s (I_0 + I_{ob}) N_D} = \frac{\tau_M}{(1+k)} \quad (5.5)$$

where $k = I_{ob}/I_0$, and $m = 2(I_1 I_2)^{1/2}/I_0$ as defined in Eq. (3.6). For convenience we define the fringe modulation as the parameter m . Obviously the parameter m' is the

actual fringe modulation, and k is regarded as the intensity of the optical bias in "relative units". Correspondingly, the optimum fringe velocity should be rewritten as:

$$v_{\text{opt}} = \frac{-E_M E_0}{K\tau_M'(E_M^2 + E_0^2)} \quad (5.6)$$

$$= \frac{-(1+k)E_M E_0}{K\tau_M(E_M^2 + E_0^2)}$$

which contains the optical bias term in the way of a factor $(1+k)$. This can be regarded as the influence of the total intensity of the writing beams on the optimum fringe velocity as described in Eq. (4.8).

Substituting Eq.(5.6) into Eq.(5.3) we can obtain an expression for the enhancement of the diffraction efficiency to be obtained with a moving grating:

$$G = \frac{\eta_{\text{at optimum velocity}}}{\eta_{\text{at zero velocity}}} = \frac{E_0^4 E_Q^2}{E_0^2(E_0^2 + E_Q E_M)^2 + E_M^4 E_Q^2} \quad (5.7)$$

which contains no reference to any terms derived from the optical bias. Obviously, Eqs.(5.6) and (5.7) are only valid at small fringe modulation.

For large fringe modulations, as we mentioned in chapter 4, higher harmonics of the variables should be considered and only numerical results can be obtained. The influence of the optical bias at large fringe modulations is thus referred to section 4.3, where the fringe modulation plays a significant role on the optimum fringe velocity and on the enhancement of the diffraction efficiency.

5.2. Experimental Configuration

The experimental set-up is shown in Fig. 5.1, which is the same as Fig. 4.5 except for a white-light (W.L.) source being used. The recording conditions of the grating for the following measurements are: $E_0 = 6.25$ kV/cm, $I_0 = 25$ mW/cm² and $\Lambda = 20$ μm .

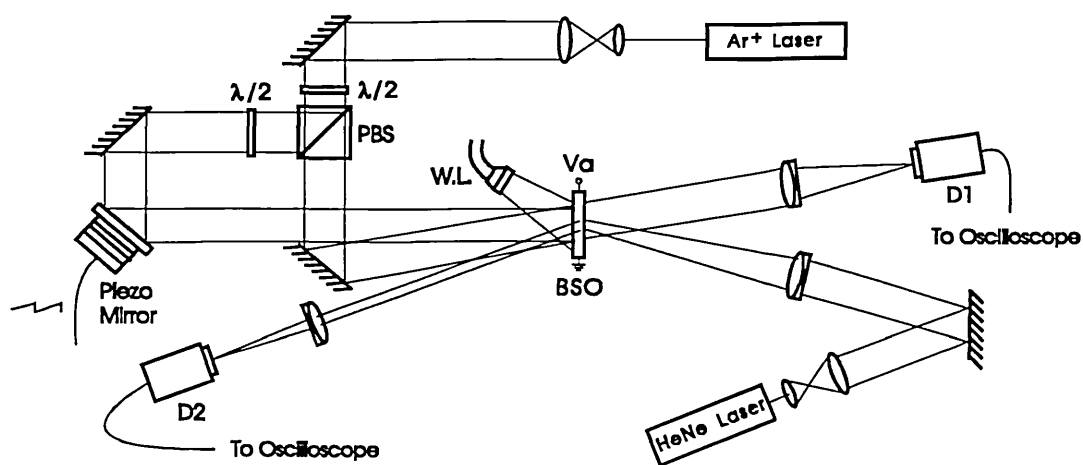


Fig. 5.1 The experimental system used for investigating the effects of optical bias on moving gratings.

Light intensity is usually measured with a power meter. In this experiment, however, such a measurement is invalid. There are two matters which should be taken into account: first, the result of the white-light illumination is the creation of additional photoelectrons, second the white-light source is a multi-spectrum source but the crystal response is spectrum dependent. Therefore we calibrate the white-light intensity by means of the measurement of the photocurrent induced, and scale it in units relative to the photocurrent induced by the writing laser beams, i.e. the white-light intensity is quoted in "relative units". More details about the scaling of the white-light intensity and the measurement of the resulting photocurrent are mentioned in reference 5.3.

5.3. Experimental Results

The experiments concentrated on the following aspects: the influence of the optical bias on the optimum fringe velocity, on the absolute diffraction efficiency, and on the enhancement of the diffraction efficiency.

5.3.1. The Influence of Optical Bias on the Optimum Fringe Velocity

The main purpose of the optical bias is to overcome the difficulty of the sudden drop in the optimum fringe velocity. Fig. 5.2 presents the experimental results of the optimum fringe velocity versus the white-light intensity. Two curves correspond to

the fringe modulation $m=0.9$ and $m=1$, respectively. We chose $m=0.9$ and $m=1$, because the sudden drop in the optimum fringe velocity occurs around those values.

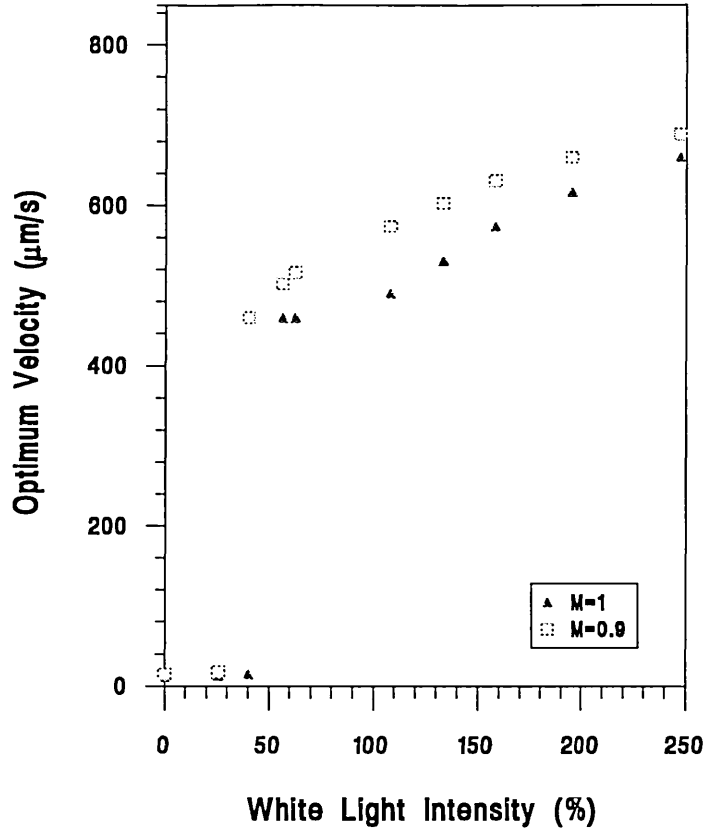


Fig. 5.2. The experimental results of the optimum fringe velocity versus the white-light intensity.

We can see from Fig. 5.2 that for the $m=0.9$ curve the optimum fringe velocity jumps to a high value ($459\mu\text{m/s}$) when the white-light intensity increases to 40 % in relative units, and for the $m=1$ curve it jumps to a high value when the white-light intensity increases to 56 % in relative units. This implies that adopting white-light illumination as a bias with an intensity of 56 % in relative units, we will be able to eliminate the sudden drop in the optimum fringe velocity.

Fig. 5.3 presents the experimental results for the optimum fringe velocity versus the fringe modulation with ("With W.L." curve) and without ("No W.L." curve) white-light illumination. The white-light intensity is set to be 56 % in relative units.

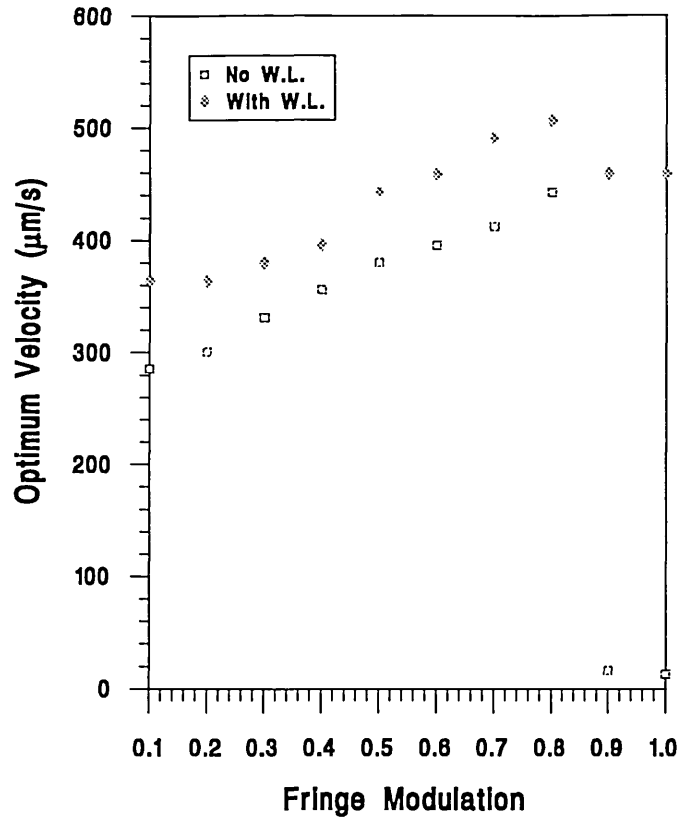


Fig. 5.3. The experimental results of the optimum fringe velocity versus the fringe modulation.

It can be seen from Fig. 5.3 that there is a sudden drop in the optimum fringe velocity at $m = 0.9$ in the case where there is no white-light illumination. This is the nonlinear effect of a moving grating at large fringe modulation. Due to the drop in the optimum fringe velocity, we cannot adopt a fixed fringe velocity to satisfactorily enhance the diffraction efficiency of gratings with different fringe modulations. In the case with white-light illumination, the sudden drop in the optimum fringe velocity is greatly reduced. This is because the optical bias reduces the actual fringe modulation [according to Eq. (5.4), the actual fringe modulation for $m = 1$ point is about 0.64 with optical bias]. Therefore an average fringe velocity of $440\mu\text{m/s}$ in this case, can be used to satisfactorily enhance the diffraction efficiency of all gratings of different spatial periods.

5.3.2. The Influence of Optical Bias on The Absolute Diffraction Efficiency

We expect that as the white-light intensity increases the absolute diffraction efficiency decreases monotonically for both a moving grating and a stationary grating because the actual fringe modulation, which determines the diffraction efficiency in both cases, is reduced by the optical bias. However, there is something unexpected in our experiments. Fig. 5.4 presents the experimental results of the absolute diffraction efficiency versus white-light intensity. "Normal" denotes a stationary grating, while "M.G." denotes a moving grating. The fringe modulation is chosen to be 0.7. We will see that there is no obvious difference in the variation behaviours of the curves with different fringe modulations.

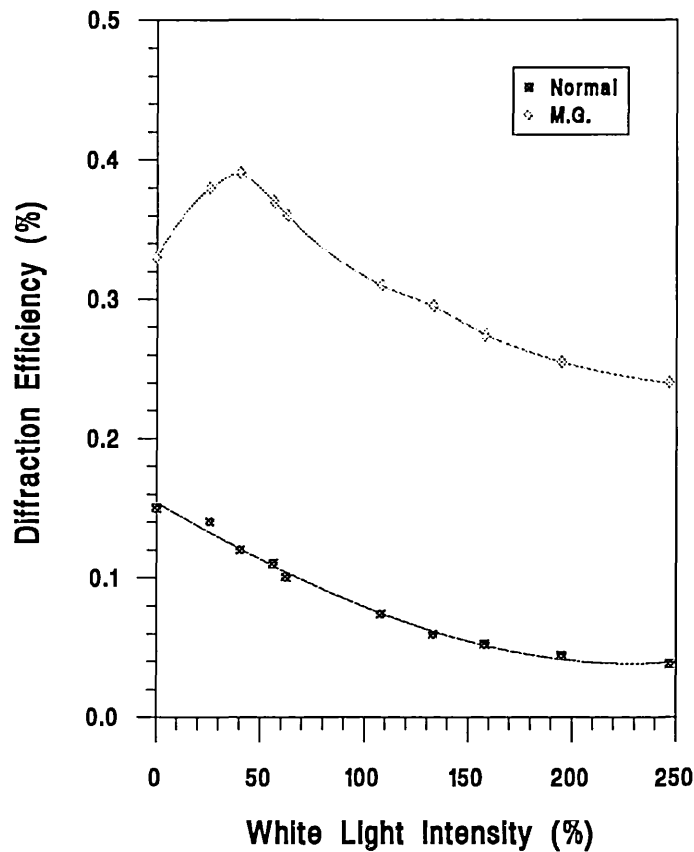


Fig. 5.4. The experimental results of the diffraction efficiency versus the white-light intensity.

We can see that with a stationary grating, the diffraction efficiency drops monotonically and rapidly as the white-light intensity increases. The situation is more complicated with a moving grating. In lower optical bias range, as the white-light intensity increases the diffraction efficiency increases as well, until it reaches its peak value at a white-light intensity of 40 % in relative units. This is not expected by consideration of its influence on the actual fringe modulation. This phenomenon implies that with suitable optical bias and moving gratings the signal-to-noise ratio can be further improved. In the higher optical bias range, as the white-light intensity increases the diffraction efficiency decreases monotonically. However the decrease is much less than that with a stationary grating. For instance when the white-light intensity is 200 % in relative units, the diffraction efficiency drops 67 % compared to that without white-light illumination in the case of stationary grating, while it only drops 24 % in the case of a moving grating.

To see whether the characteristics of the curve in Fig. 5.4 are more general, Fig. 5.5 presents the experimental results of the absolute diffraction efficiency versus the white-light intensity with a moving grating for different fringe modulations. Four curves represent the fringe modulation of 0.3, 0.5, 0.7 and 0.9, respectively.

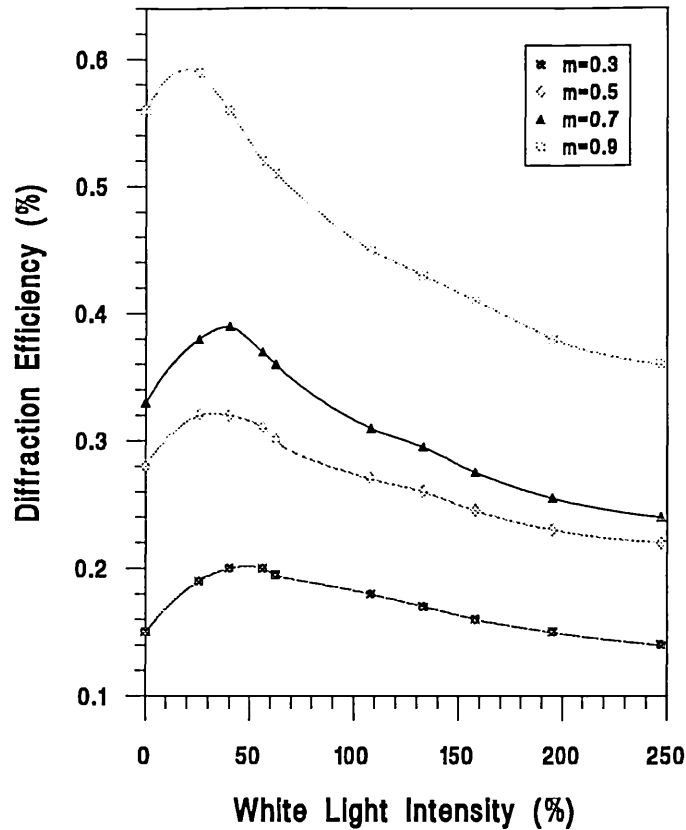


Fig. 5.5. The experimental results of the diffraction efficiency versus the white light intensity for different fringe modulations.

We can see that their variations are very similar: as the white-light intensity increases from zero, the diffraction efficiency increases until it reaches its peak value, and then as the white-light intensity increases further the diffraction efficiency decreases monotonically. It is a common characteristic of the four curves that a peak value appears at a certain non-zero white-light intensity. This phenomenon may reveal some further details of the moving grating formation in photorefractive materials.

Fig. 5.6 presents the experimental results of the diffraction efficiency versus the fringe modulation with and without white-light illumination. These curves provide a general idea of the reconstruction of a recorded object. "Normal", "M.G.", and "M.G.+W.L." denote the stationary grating, the moving grating, and the moving grating with white-light illumination, respectively. The white-light intensity is again chosen to be 56 % in relative units to overcome the sudden drop in the optimum fringe velocity.

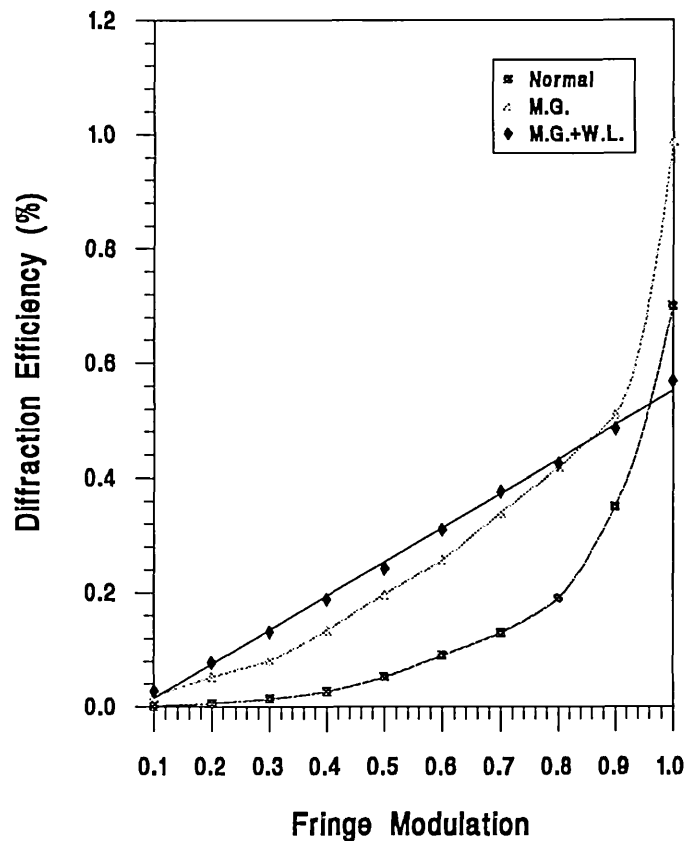


Fig. 5.6. The experimental results of the diffraction efficiency versus fringe modulation

The variation of the "Normal" curve approximately obeys the square power law i.e. the diffraction efficiency is proportional to the square of the fringe modulation when the fringe modulation is less than 0.6^{3,8}. The square power law enable us to adopt a linear holographic recording where the intensity of the diffraction is proportional to the intensity of the recorded image, and a linear reconstruction could be achieved. The curve "M.G.+W.L." seems to be a straight line. The linear variation of the diffraction efficiency as the fringe modulation would be expected to yield a reconstruction of the

recorded image according to a square root power, which is a distorted reconstruction. However in some particular applications this feature would be an advantage. For instance if we want to manifest the amplitude, rather than the intensity, distribution of an image the reconstruction of the square root power of the recorded image will give the amplitude distribution of the original image directly.

It can also be seen that the "M.G.+W.L." curve is beyond the "Normal" and the "M.G." curves for a wide range of the fringe modulation, i.e the highest diffraction efficiency is achieved by adopting additional white-light illumination to a moving grating. This implies that while a suitable optical bias, e.g. 56 % in this case, eliminates the sudden drop in the optimum fringe velocity, it also further enhances the diffraction efficiency.

5.3.3. The Influence of Optical Bias on Enhancement of The Diffraction Efficiency

Fig. 5.4 has shown that the decrease in absolute diffraction efficiency due to white-light illumination with a moving grating is much smaller than that with a stationary grating. Therefore the application of optical bias will increase the enhancement of the diffraction efficiency. Fig. 5.7 presents the experimental results. Three curves correspond to the fringe modulations $m = 0.8$, $m = 0.6$, and $m = 0.4$, respectively.

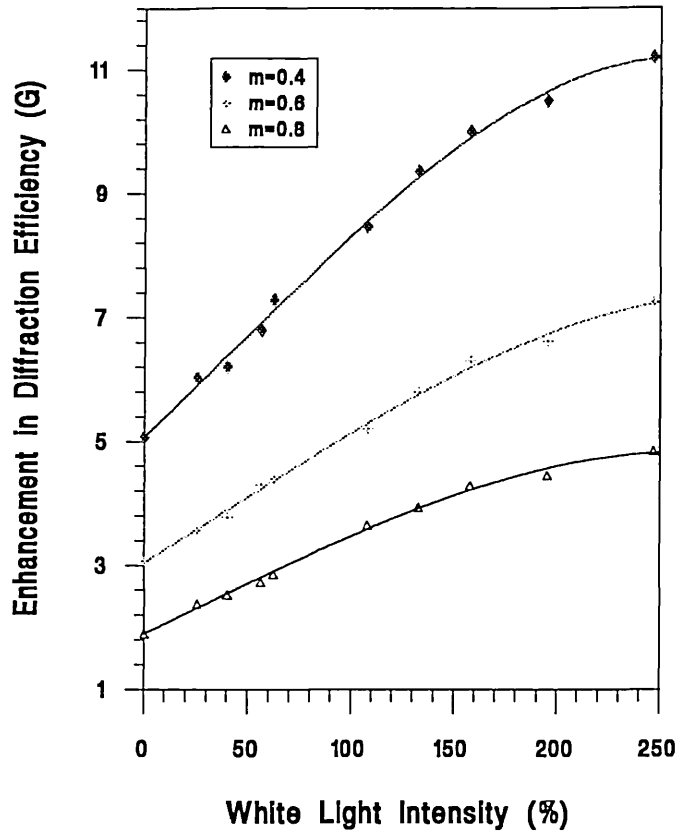


Fig. 5.7. The experimental results of the enhancement of the diffraction efficiency versus the optical bias.

We can see that as the white-light intensity increases, the enhancement of the diffraction efficiency increases as well. This can be explained by the nonlinearity of moving gratings at large fringe modulations: the optical bias decreases the actual fringe modulation, and the smaller the fringe modulation is, the higher the enhancement of the diffraction efficiency. In the adopted white-light intensity range the three curves can be fit by polynomials as:

$$G = 5.07 + 3.17 x + 0.3 x^2 \quad (5.8)$$

$$G = 3.04 + 2.08 x + 0.1 x^2 \quad (5.9)$$

$$G = 1.89 + 1.81 x + 0.1 x^2 \quad (5.10)$$

for $m = 0.4$, $m = 0.6$ and $m = 0.8$ respectively, where x denotes the white-light intensity in relative unit. For a comparison, if we choose the white-light intensity to be 200 % in relative units the enhancements are 5.5, 7.6 and 12.6 for $m = 0.8$,

$m = 0.6$ and $m = 0.4$, respectively. They are 1.9, 3.0 and 5.1 in the case without a white-light illumination.

5.4 Conclusions

From the above experimental results we can draw some conclusions about applying optical bias to a moving grating:

1. With a suitable white-light intensity, the sudden drop in the optimum fringe velocity at fringe modulations close to unity can be eliminated, which is beneficial to the holographic reconstruction in the case of gratings with different fringe modulations.
2. The influence of the optical bias on the absolute diffraction efficiency is complicated: as the white-light intensity increases from zero, the diffraction efficiency increases as well until it reaches its maximum value at a specific point. In this range, the diffraction efficiency is higher than that without white-light illumination. This cannot be explained by simply considering the influence of actual fringe modulation on the diffraction efficiency. As the white-light intensity increases further, the diffraction efficiency decreases. However the decrease is not as serious as compared to the case of a stationary grating.
3. With a suitable white light illumination, the diffraction efficiency seems linearly dependent on the fringe modulation which causes a distorted reconstruction. However, it may find applications for some particular cases.
4. By applying optical bias, we can increase the ratio of the diffraction efficiency with a moving grating to that with a stationary grating.

References:

- 5.1. C. Soutar, W.A. Gillespie and C.M. Cartwright, "The effect of optical bias on grating formation dynamics in photorefractive BSO", *Opt. Commun.*, **90** (1992) 329-334.

5.2. C. Soutar, Z.Q. Wang, W.A. Gillespie, and C.M. Cartwright, "A novelty-filtered optical intensity correlator using photorefractive BSO", *Optik*, **94** (1993) 16-22.

5.3. C. Soutar, "Optical information processing using photorefractive BSO", Ph.D. thesis, Dundee Institute of Technology, Dundee, (1991).

Chapter 6. Development of a Real-Time Intensity Correlator using BSO

6.1. Introduction

Since Vander Lugt holographically fabricated the matched spatial filter in 1964^{6.1}, coherent optical correlators have dominated optical pattern recognition. Coherent correlators deal with a complex signal, where the processing of both phase and amplitude information is significant in many cases. However, most actual objects are usually either incoherently illuminated or self-luminous, and an incoherent optical system is therefore more suitable for actual object inputs. The incoherent optical system has the obvious advantage of no coherent noise and so an output of reasonable quality can be expected. Furthermore, the restrictions on the alignment accuracy of the incoherent system are relaxed, which is beneficial to a real-time processing system, perhaps in an industrial context.

An incoherent correlator which uses a Fourier transform filter was first proposed by Lohmann and Werlich^{6.2}. Then Mu et al. alternatively used a Fresnel transform filter^{6.3}. From a sampling point of view, a Fresnel transform filter performs as well as a Fourier transform filter. However, in our case a Fresnel transform is preferable because it produces a more uniform light distribution which yields a more effective diffraction area, reduces the demands on the dynamic range of the recording material, and alleviates the distortion when the moving grating technique is used. Recent developments of intensity correlation include rotation invariant correlation^{6.4, 6.5}, the use of a laser diode array as an input device^{6.6} and the use of a BSO as the real-time holographic recording material^{3.5}.

Although reference 3.5 has presented the results of real-time intensity correlation using BSO, there are still two problems which need to be considered. First, the discrimination is inherently low. For example, if we consider the correlation of a one-dimensional rectangular function of width "1", in the coherent case the full width at half maximum intensity of the auto-correlation peak, which is a measure of the discrimination, is approximately 0.6, whereas it is 1 in the case of intensity correlation. Fig. 6.1 shows the coherent and the intensity correlation of one-dimensional rectangular function.

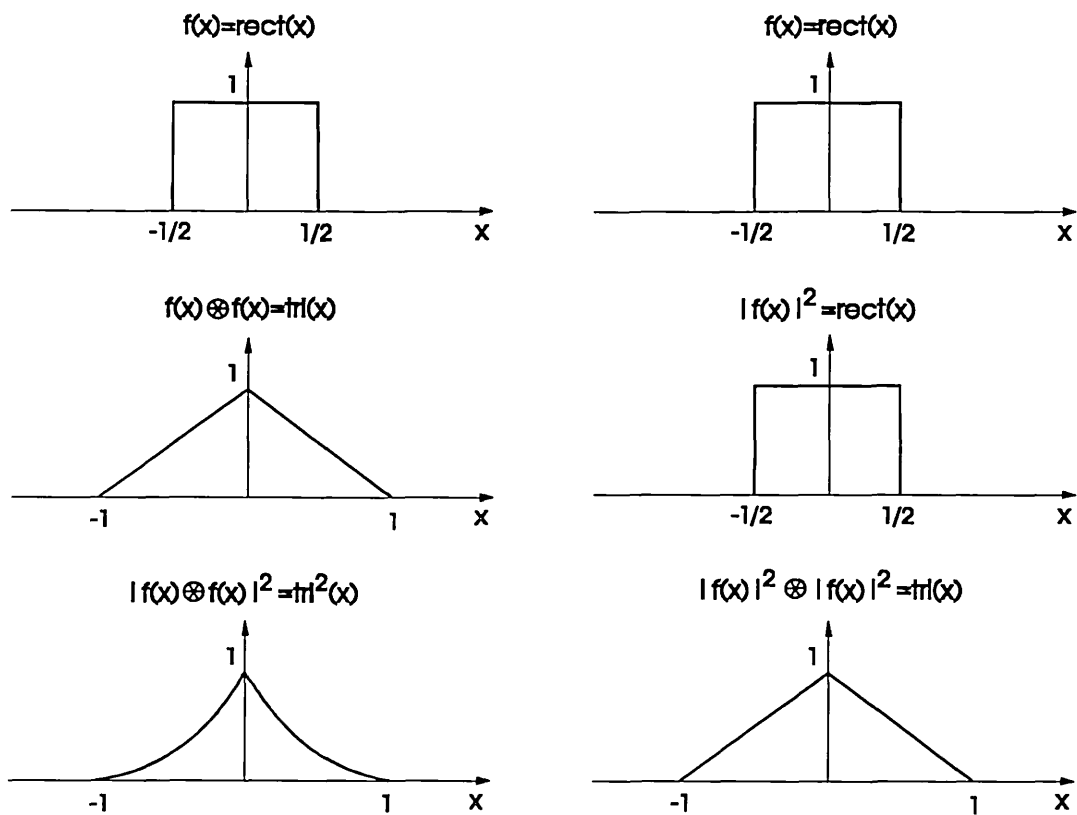


Fig. 6.1. The coherent (left) and the intensity (right) correlation of an one-dimensional rectangular function.

In Fig. 6.1 the rectangular function is defined as:

$$\text{rect}\left(\frac{x}{a}\right) = \begin{cases} 0 & |x| > \frac{a}{2} \\ 1 & |x| \leq \frac{a}{2} \end{cases} \quad (6.1)$$

and the triangle function is defined as:

$$\text{tri}\left(\frac{x}{a}\right) = \begin{cases} 0 & |x| > a \\ 1 - \frac{|x|}{a} & |x| \leq a \end{cases} \quad (6.2)$$

where "a" is a constant. We can see from Fig. 6.1 that the intensity distribution of the coherent correlation I_c is given by:

$$I_c = \text{tri}^2(x) \quad (6.3)$$

and the half maximum intensity points can be deduced to be at $x = \pm \left(1 - \frac{\sqrt{2}}{2}\right)$, which

has an approximately full width of 0.6. On the other hand, the intensity distribution of the intensity correlation I_i is given by:

$$I_i = \text{tri}(x) \quad (6.4)$$

and the half maximum intensity points can be deduced to be at $x = \pm \frac{1}{2}$, which has a full width of 1. We can see that the full width of the half maximum intensity of the coherent auto-correlation peak is 0.6 that of the intensity auto-correlation peak.

Second, the diffracted light fluctuates due to the random energy transfer between writing beams with a dynamic grating. The instability of the output intensity causes difficulty in setting the threshold.

This chapter presents further developments on real-time intensity correlators using BSO relating to the problems mentioned above. Two topics are involved: real-time edge-enhanced intensity correlation and real-time intensity correlation enhanced by a moving grating.

6.2. Basic Intensity Correlator using a Fresnel Transform Filter

Chapter 2 described an optical system performing a Fresnel transform where the input plane is at the front focal plane of the transform lens and the transform plane is arbitrarily selected (Fig. 2.3). For a more general case the distances between the input plane and the transform lens, and between the transform lens and the transform plane both can be selected arbitrarily. The Fresnel transform of a signal is a mixture of the properties of the space and frequency distributions of the signal. With a different selection of the distances between the optical elements, the Fresnel spectrum will be

totally different. This offers flexibility in controlling the size and the uniformity of the Fresnel spectrum.

Chapter 2 also described an optical correlator using a Fresnel transform filter where two transform lenses were used (Fig. 2.4). If a convergent reference beam is used to record the spatial filter, the optical correlator can be a more compact system with only a single transform lens. The analysis below is based on the above considerations.

6.2.1. Fabrication of the Fresnel Transform Filter

Fig. 6.2 is the configuration of the holographic recording system used for the fabrication of the Fresnel transform filter. P1 is the input plane. L2 is the transform lens whose focal length is f . P2 is the Fresnel plane where a photosensitive plate is placed to record the filter. A convergent reference beam is focused to the point B in plane P3. The distances between P1 and L2, between L2 and P2, and between P2 and P3 are d_1 , d_2 , and d respectively.

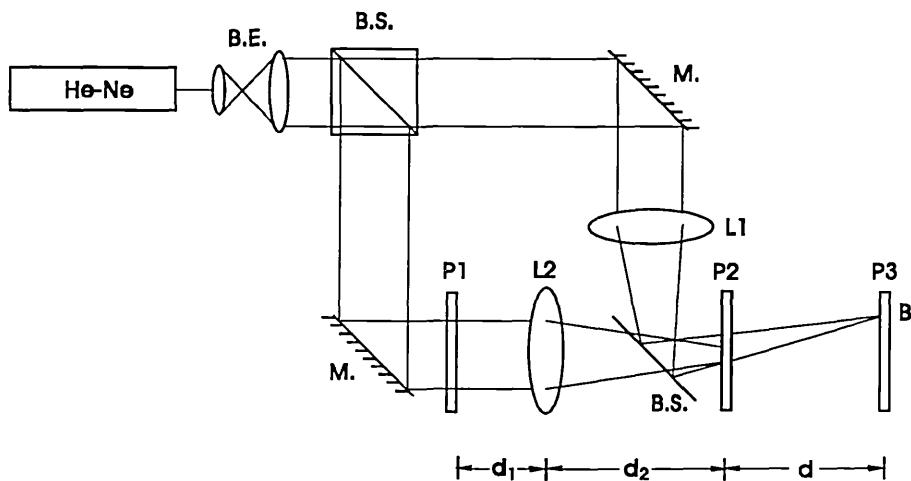


Fig. 6.2. The optical system for fabricating a Fresnel transform filter.

Suppose the input is expressed as $f(x,y)$. With in the Fresnel approximation the complex light distribution in the plane P2 can be written as:

$$\begin{aligned}
O(\alpha, \beta) &= \iiint_{-\infty}^{\infty} \iiint_{-\infty}^{\infty} f(x, y) \exp\left\{\frac{i\pi}{\lambda d_1} [(\xi - x)^2 + (\eta - y)^2]\right\} \exp\left[\frac{-i\pi}{\lambda f} (\xi^2 + \eta^2)\right] \\
&\quad \exp\left\{\frac{i\pi}{\lambda d_2} [(\alpha - \xi)^2 + (\beta - \eta)^2]\right\} dx dy d\xi d\eta \\
&= \iint_{-\infty}^{\infty} f(x, y) \exp\left[\frac{i\pi}{\lambda f_{\text{eff}}} \left(\frac{f - d_1}{f}\right) (\alpha^2 + \beta^2)\right] \exp\left[\frac{i\pi}{\lambda f_{\text{eff}}} \left(\frac{f - d_2}{f}\right) (x^2 + y^2)\right] \\
&\quad \exp\left[\frac{-i2\pi}{\lambda f_{\text{eff}}} (x\alpha + y\beta)\right] dx dy
\end{aligned} \tag{6.5}$$

which is a Fourier transform of the input with a quadratic phase factor, where $f_{\text{eff}} = (d_1 f + d_2 f - d_1 d_2) / f$ is the effective focal length as compared with f in the standard Fourier transform [see Eqs. (2.8) and (2.9)], and (ξ, η) and (α, β) are the coordinate systems of L2 and P2, respectively. The convergent reference beam can be written as:

$$R(\alpha, \beta) = \exp\left\{\frac{-i\pi}{\lambda d} [(\alpha - h_0)^2 + \beta^2]\right\} \tag{6.6}$$

where h_0 is the distance between the convergent point B and the origin of plane P3. The intensity distribution due to the interference between the object and the reference beams is given by:

$$I(\alpha, \beta) = |O(\alpha, \beta) + R(\alpha, \beta)|^2 \tag{6.7}$$

After exposure and development the Fresnel transform filter is fabricated. If the exposure takes place at the linear region of the T-E curve of the photosensitive plate^{6,7}, the amplitude transmittance of the recorded filter will be proportional to the light intensity distribution, which has three diffraction terms. The term relating to the correlation output is given by:

$$t(\alpha, \beta) = O^*(\alpha, \beta) R(\alpha, \beta) \tag{6.8}$$

6.2.2. Optical Intensity Correlation using a Fresnel Transform Filter

The optical intensity correlator using a Fresnel transform filter is shown in Fig. 6.3 where a rotating diffuser D is used to transform the coherent laser beam into time-averaged spatially incoherent. L is the transform lens. P_1 , P_2 and P_3 are the input plane, filter plane and output plane, respectively. We assume that the focal length of L , and the distances between P_1 and L , between L and P_2 , and between P_2 and P_3 are f , d_1 , d_2 , and d , respectively, as in the recording system, to ensure that the Fresnel spectrum of the input has the same scale as the fabricated filter.

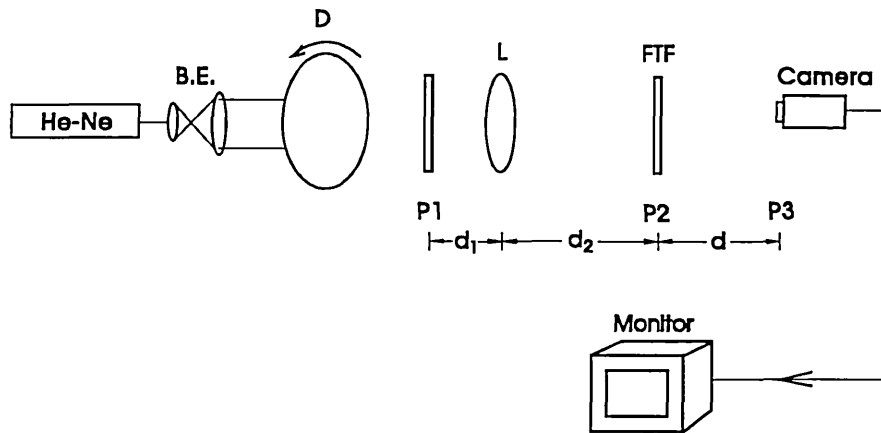


Fig. 6.3. The optical intensity correlator using a Fresnel transform filter.

To calculate the impulse response of the optical system we suppose an input impulse $\delta(x - x_0, y - y_0)$ being at P_1 . The complex light distribution at P_2 induced by the input impulse is given by the Fresnel integration:

$$\begin{aligned}
E(\alpha, \beta) &= \iint_{-\infty}^{\infty} \exp\left\{\frac{i\pi}{\lambda d_1} [(\xi - x_0)^2 + (\eta - y_0)^2]\right\} \exp\left[\frac{-i\pi}{\lambda f} (\xi^2 + \eta^2)\right] \\
&\quad \exp\left\{\frac{i\pi}{\lambda d_2} [(\alpha - \xi)^2 + (\beta - \eta)^2]\right\} d\xi d\eta \\
&= \exp\left[\frac{i\pi}{\lambda f_{\text{eff}}} \left(\frac{f - d_1}{f}\right) (\alpha^2 + \beta^2)\right] \exp\left[\frac{i\pi}{\lambda f_{\text{eff}}} \left(\frac{f - d_2}{f}\right) (x_0^2 + y_0^2)\right] \\
&\quad \exp\left[\frac{-i2\pi}{\lambda f_{\text{eff}}} (x_0 \alpha + y_0 \beta)\right]
\end{aligned} \tag{6.9}$$

This light field is then modified by the function of Eq. (6.8), and the complex light distribution in P3, which is the impulse response, is given by:

$$h(x', y'; x_0, y_0) = \iint_{-\infty}^{\infty} E(\alpha, \beta) t(\alpha, \beta) \exp\left\{\frac{i\pi}{\lambda d} [(x' - \alpha)^2 + (y' - \beta)^2]\right\} d\alpha d\beta \tag{6.10}$$

where (x', y') is the coordinate system of P3. Substituting Eqs. (6.5), (6.6), (6.8) and (6.9) into Eq. (6.10), and completing the integration, we get the impulse response of the optical system as:

$$h(x', y'; x, y) = C(x', y'; x, y) f^*(x + ax' - ah_0, y + ay') \tag{6.11}$$

where $a = f_{\text{eff}}/d$ is a scale factor, and $C(x', y'; x, y)$ is a complex constant. The intensity impulse response is given by the square of the modulus of the impulse response, yielding:

$$h_i(x', y'; x, y) = |f(x + ax' - ah_0, y + ay')|^2 \tag{6.12}$$

Suppose an optical signal with intensity distribution $|f'(x, y)|^2$ is at P1, the output intensity at P3, according to the optical linear system theory, is given by the integration:

$$I(x', y') = \iint_{-\infty}^{\infty} |f'(x, y)|^2 |f(x + ax' - ah_0, y + ay')|^2 dx dy \quad (6.13)$$

which is the intensity correlation of the input signal with the reference signal.

The Fresnel transform possesses no shift invariance (see chapter 2). A shift in the input signal causes not only an additional phase factor but also a displacement in its Fresnel spectrum. Thus with coherent illumination, the Fresnel spectrum of a shifted input cannot overlap with the filter area, and the output pattern is therefore input position dependent. With spatially incoherent illumination, the situation is different. In this case the light distribution of a shifted input at the filter plane still covers the filter, therefore the position of the input signal has no influence in the output pattern except for a corresponding displacement.

6.3 Real-Time Intensity Correlator using BSO

The real-time intensity correlator using BSO is shown in Fig. 6.4. In the writing part, the collimated argon-ion laser beam is split into two beams; one beam is used to illuminate a transparency, input 1, and the other acts as the reference beam. L1 forms the Fresnel transform of input 1 onto the crystal. The focal length of L1 is f , and the distances between input 1 and L1, and between L1 and the crystal are d_g and d_g' , respectively. In the reading part, a He-Ne laser is used to illuminate the rotating diffuser D by which an incoherent light source is obtained. Input 2 is the reference object, and L2 is the transform lens. The focal length of L2 is f' , and the distances between input 2 and L2, and between L2 and the crystal are d_r and d_r' , respectively. The reconstructed image is detected via a video camera positioned at the back focal plane of the transform lens L3. The focal length of L3 is f'' . An interference filter IF and a polaroid P were used to suppress the background noise.

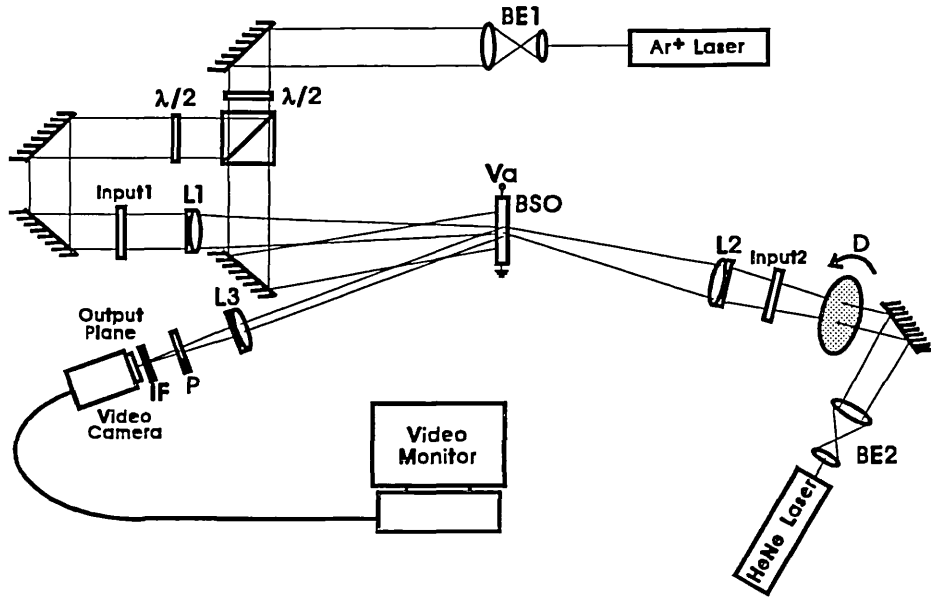


Fig. 6.4 The experimental configuration of the real-time intensity correlator using a BSO crystal.

Again suppose that input 1 is expressed as $f(x,y)$, the complex light distribution at the crystal plane can be expressed, referring to Eq. (6.5), as:

$$O(\alpha, \beta) = \iint_{-\infty}^{\infty} f(x, y) \exp \left[\frac{i\pi}{\lambda_{514} f_{\text{eff}}} \left(\frac{f - d_g}{f} \right) (\alpha^2 + \beta^2) \right] \exp \left[\frac{i\pi}{\lambda_{514} f_{\text{eff}}} \left(\frac{f - d_g'}{f} \right) (x^2 + y^2) \right] \exp \left[\frac{-i2\pi}{\lambda_{514} f_{\text{eff}}} (x\alpha + y\beta) \right] dx dy \quad (6.14)$$

where $f_{\text{eff}} = (d_g f + d_g' f - d_g d_g') / f$, (x, y) , (ξ, η) and (α, β) are the coordinate systems of the planes of input 1, the lens L1 and the crystal, respectively, and λ_{514} is the wavelength of the writing argon laser. The reference beam is a plane wave and can be described by:

$$R(\alpha, \beta) = R_0 \exp \left(\frac{-i2\pi}{\lambda_{514}} \alpha \sin \vartheta_0 \right) \quad (6.15)$$

where ϑ_0 is the external angle that the reference beam makes with the normal to the crystal plane. Assuming that the object and reference beams are of parallel polarization, the intensity pattern in the crystal plane will be given by:

$$I(\alpha, \beta) = |O(\alpha, \beta) + R(\alpha, \beta)|^2 \quad (6.16)$$

This light distribution forms a space-charge field which is proportional to the inhomogeneous light illumination [see Eq. (3.14) where the space-charge field E_{sc} is proportional to the fringe modulation]. Considering only the term that is associated with the correlation output of the system, the space-charge field can be expressed as:

$$E_{sc}(\alpha, \beta) \propto O(\alpha, \beta)R^*(\alpha, \beta) \quad (6.17)$$

The photo-induced space-charge field modulates the refractive index of the crystal via the linear electro-optic effect. The change in the refractive index is given by [see Eq. (3.23)]:

$$\Delta n(\alpha, \beta) = n_0^3 r_{41} E_{sc}(\alpha, \beta) \quad (6.18)$$

which yields a phase modulation:

$$\varphi(\alpha, \beta) = \frac{2\pi}{\lambda_{633}} T \Delta n(\alpha, \beta) \quad (6.19)$$

where λ_{633} is the wavelength of the readout He-Ne laser, and T is the thickness of the crystal. The amplitude transmittance of the crystal is then given by:

$$\begin{aligned} t(\alpha, \beta) &= \exp[i\varphi(\alpha, \beta)] \\ &\approx 1 + i\gamma O(\alpha, \beta)R^*(\alpha, \beta) \end{aligned} \quad (6.20)$$

where $\gamma = \frac{2\pi}{\lambda_{633}} T n_0^3 r_{41}$ is a constant. The final expression in Eq. (6.20) is valid for small phase modulation, which is true for the hologram recorded in BSO.

To calculate the intensity impulse response of the optical system, we suppose that an impulse $\delta(x - x_0, y - y_0)$ is at the plane of input 2. The induced complex light distribution at the crystal plane, referring to Eq (6.9), can be expressed as:

$$E(\alpha, \beta) = \exp\left[\frac{i\pi}{\lambda_{633}f_{\text{eff}}'}\left(\frac{f' - d_r}{f'}\right)(\alpha^2 + \beta^2)\right] \exp\left[\frac{i\pi}{\lambda_{633}f_{\text{eff}}'}\left(\frac{f' - d_r'}{f'}\right)(x_0^2 + y_0^2)\right] \exp\left[\frac{-i2\pi}{\lambda_{633}f_{\text{eff}}'}(x_0\alpha + y_0\beta)\right] \quad (6.21)$$

where $f_{\text{eff}}' = (d_r f' + d_r' f' - d_r d_r')/f'$. To ensure that the Fresnel transforms are formed at the crystal at the appropriate scales, d_r , d_r' and f' were all chosen to accommodate the change in wavelength, i.e.

$$d_r = \frac{514}{633}d_g, \quad d_r' = \frac{514}{633}d_g', \quad f' = \frac{514}{633}f. \quad (6.22)$$

This light field is filtered by the recorded hologram, and the complex light distribution at the output plane (x', y') will be given by the Fourier transform:

$$h(x', y'; x_0, y_0) = \iint_{-\infty}^{\infty} E(\alpha, \beta) t^*(\alpha, \beta) \exp\left[\frac{-i2\pi}{\lambda_{633}f''}(\alpha x' + \beta y')\right] d\alpha d\beta \quad (6.23)$$

The conjugate transmission function, $t^*(\alpha, \beta)$, is encountered by this beam because it is counter-propagating to the writing beams. Substituting Eqs. (6.20) and (6.21) into Eq. (6.23) and performing the integration we can obtain the impulse response of the system as:

$$h(x', y'; x_0, y_0) = C(x', y'; x_0, y_0) f^*(x_0 + ax' + f_{\text{eff}} \sin \vartheta_0, y_0 + ay') \quad (6.24)$$

where $a = f_{\text{eff}}'/f''$ is the scale factor. We can see that the scale of the impulse response can be changed by choosing different values of d_r , d_r' , f' and f'' . If they

are chosen such that $f_{\text{eff}}' = f''$, unity magnification can be obtained. With a further assumption that $f'' = \frac{514}{633} f$, the impulse response function can be simplified as:

$$h(x', y'; x_0, y_0) = C(x', y'; x_0, y_0) f^*(x_0 + x' + f \sin \vartheta_0, y_0 + y') \quad (6.25)$$

The intensity impulse response function is then given by:

$$h_i(x', y'; x, y) = |f(x + x' + f \sin \vartheta_0, y + y')|^2 \quad (6.26)$$

If an optical signal with an intensity distribution of $|f'(x, y)|^2$ is input 2, the intensity distribution at the output plane will be given by the integration:

$$I(x', y') = \iint_{-\infty}^{\infty} |f'(x, y)|^2 |f(x + x' + f \sin \vartheta_0, y + y')|^2 dx dy \quad (6.27)$$

which is recognized as the intensity correlation.

6.4 Real-Time Edge-Enhanced Intensity Correlation with BSO

To improve the discrimination of the intensity correlator, the edge-enhancement technique can be adopted. Especially in a correlator using BSO, the edge-enhancement can be performed in real-time by nonlinear holographic recordings. Coherent edge enhancement using BSO has been previously reported by Huignard and Herriau^{6.8}. By reversing the conventional object-to-reference beam ratio (O/R) during holographic recording (i.e. making the object beam intensity much greater than the reference beam intensity), an edge-enhanced image was obtained. This phenomenon has been analysed by Feinberg^{6.9}. Connors et al. have applied coherent edge enhancement to optical correlation using four-wave mixing architecture in photorefractive materials^{3.2}. The results of references 3.2, 6.8 and 6.9 can be extended to an incoherent system. By reversing the object-to-reference beam ratio, the real-time edge-enhancement operation as well as the intensity correlation itself can be achieved using BSO.

6.4.1. Incoherent Edge-Enhancement using a BSO

Suppose that input 1 in Fig. 6.4 is expressed as $f(x,y)$. The interference pattern between the Fresnel transform of $f(x,y)$ and the uniform reference beam will generate a periodic array of refractive index grating planes within the volume of the crystal. The modulation depth of this volume grating, which directly determines the diffracted beam intensity, is described by [see Eq. (3.6)]:

$$m(\alpha, \beta) = \frac{2|O(\alpha, \beta)||R(\alpha, \beta)|}{|O(\alpha, \beta)|^2 + |R(\alpha, \beta)|^2} \quad (6.28)$$

where $O(\alpha, \beta)$ and $R(\alpha, \beta)$ are the object (Fresnel spectrum) and the reference beams at the crystal plane, respectively.

In the case of conventional holographic conditions ($O/R \sim 1/2$) it is clear that in all regions of the crystal $|R(\alpha, \beta)| > |O(\alpha, \beta)|$, and so a linear recording of the object is possible. Under these conditions, the intensity impulse response of the optical system is given by Eq. (6.26)

In the case of nonlinear recording, on the other hand (i.e. with the reversed object-to-reference beam ratio, $O/R \gg 1$), at the bright and dark regions of the Fresnel spectrum, $|O(\alpha, \beta)| \gg |R(\alpha, \beta)|$ and $|O(\alpha, \beta)| \ll |R(\alpha, \beta)|$, respectively. Thus within these regions $m(\alpha, \beta)$ is very small. It is evident that $m(\alpha, \beta)$ takes its maximum value of unity only in the regions where the intensity of the Fresnel spectrum is equal to that of the reference beam. There is a direct intensity relationship between the Fresnel spectrum and the input: the high intensity regions of the Fresnel spectrum correspond directly to the transmissive regions of the input transparency. Therefore, the maximum modulation of the grating will occur at the regions corresponding to the transition between the bright and dark portions of the input object; i.e. at the edges of the object. Thus, with nonlinear holographic recording in the BSO crystal, the intensity impulse response of the optical system should be modified as:

$$h_i(x', y'; x, y) = |f_{ed}(x' + x + f \sin \vartheta_0, y' + y)|^2 \quad (6.29)$$

where the subscript "ed" denotes the edge-enhanced signal.

If input 2 is a pinhole at the origin, to simulate a delta function, the output intensity will be given by the convolution of this delta function with the intensity impulse response. This yields as the output of the system:

$$I(x', y') = |f_{ed}(x' + fsin \vartheta_0, y')|^2 \quad (6.30)$$

which is the incoherent edge-enhanced version of the input object.

6.4.2 Intensity Edge-Enhanced Correlation

The principle of the intensity edge-enhanced correlation using nonlinear recording in BSO differs from that of the previously reported coherent version. In the coherent correlator the nonlinearly recorded hologram acts as a high-pass spatial filter, ensuring that only the high-frequency content of the Fourier spectrum of input 2 will contribute to the output. In the intensity correlator, however, due to the spatially incoherent readout, this coherent filtering does not take place any more. Therefore, if input 2 is described by $f(x,y)$, then the output intensity is given by the convolution of $|f'(x,y)|^2$ with the intensity impulse response given in Eq. (6.29), yielding:

$$I(x', y') = \iint_{-\infty}^{\infty} |f'(x, y)|^2 |f_{ed}(x' + x + fsin \vartheta_0, y' + y)|^2 dx dy \quad (6.31)$$

which is the intensity cross-correlation of the full image of input 2 with the edge-enhanced version of the image of input 1. In order that the edge-enhanced auto-correlation is obtained, input 2 must also be the edge-enhanced version of the object. As input 2 can be treated as the reference signal in the arrangement of Fig. 6.4 (input 1 is the unknown object to be recognized in this case), some pre-processing of input 2 can take place without jeopardising the operation speed of the system. The edge-enhanced version of input 2 is thus easily obtained by using computer image processing beforehand. Consequently, the output intensity becomes:

$$I(x', y') = \iint_{-\infty}^{\infty} |f'_{ed}(x, y)|^2 |f_{ed}(x' + x + f \sin \vartheta_0, y' + y)|^2 dx dy \quad (6.32)$$

which is the edge-enhanced intensity correlation, as desired.

6.4.3 Experiments and Results

In the experiment, the crystal orientation is as Fig. 3.2, to obtain the maximum diffraction efficiency. The argon laser was expanded and adjusted to be 5 mW/cm^2 at the crystal. The applied electric field across the crystal is 6.25 kV/cm . The angle ϑ_0 was adjusted so that the average spatial period of the holographic fringes in the crystal was $20 \text{ }\mu\text{m}$. The setting of the fringe spacing at $20 \text{ }\mu\text{m}$ is a compromise between achieving as large a fringe spacing as possible (to maximize the Bragg acceptance angle) and allowing the zero-order and the diffracted image to be spatially separated within the confines of the system. The He-Ne laser used in the readout part was adjusted to be 15 mW .

Fig. 6.5 shows the image to be recognised, which is used as input 1. For conventional correlation, it is also the reference image and used as input 2.

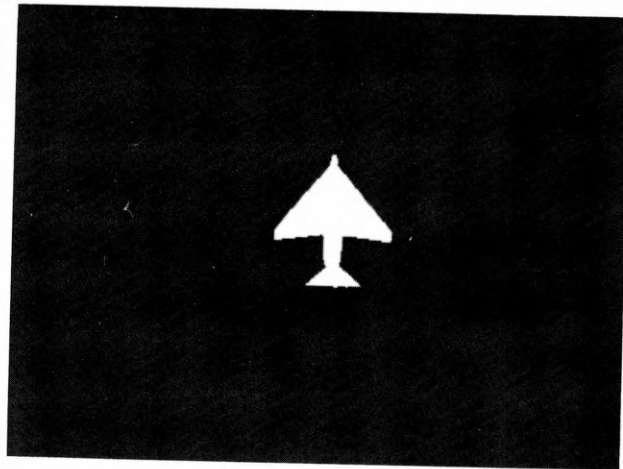


Fig. 6.5. The image to be recognised, which is used as input 1 and input 2 for conventional intensity correlation.

Fig. 6.6 shows the intensity auto-correlation result obtained with the optical system shown in Fig. 6.4 under the conditions of normal holographic recording (the object-to-reference beam ratio is about 1:2). It can be seen that the correlation peak is fairly wide.



Fig. 6.6. The intensity correlation result obtained with conventional holographic recording in BSO (O/R = 1/2 in average).

In order to obtain edge-enhanced auto-correlation, the reference image should be edge-enhanced version, and can be generated by computer pre-processing. Fig. 6.7 shows such an image which is the edge-enhanced version of Fig. 6.5 and is used as input 2. The unknown image is input 1.

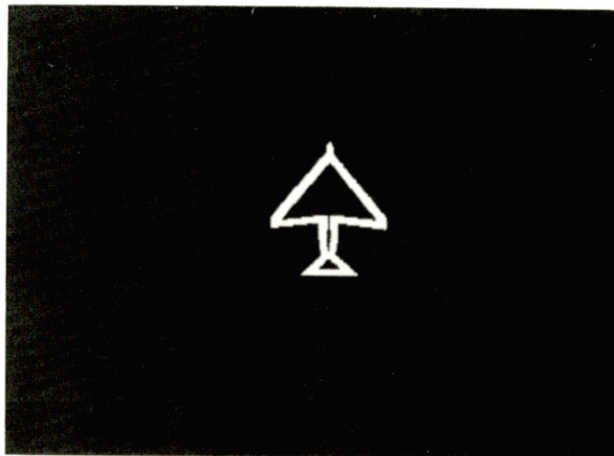


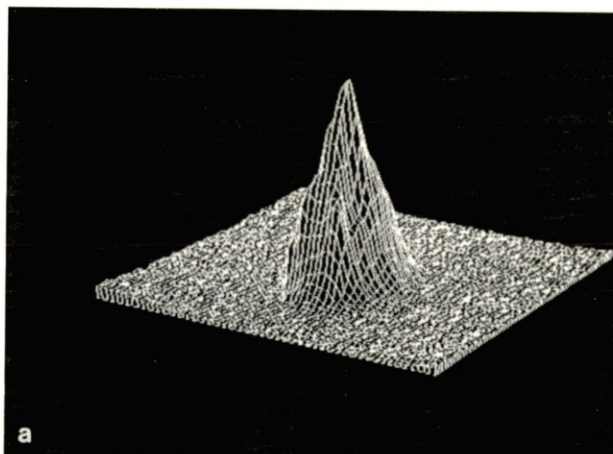
Fig. 6.7. The computer-generated edge-enhanced image used as input 2 in the intensity correlator.

Fig. 6.8 shows the real-time edge-enhanced intensity auto-correlation result when the object of Fig. 6.5 is fed into the optical system. The object-to-reference beam ratio is chosen to be about 10:1 for nonlinear holographic recording. It is clear that the correlation peak is much sharper.

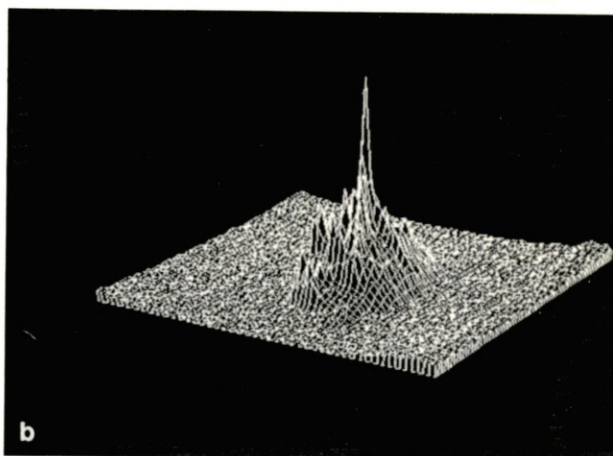


Fig. 6.8. The intensity correlation result obtained with nonlinear holographic recording in BSO (O/R = 10/1) in average).

In order that a quantitative comparison can be obtained, 3-D plots of Fig. 6.6 and Fig. 6.8 were generated and shown in Fig. 6.9 (a) and (b), respectively. This was done by detecting the optical correlation pattern with a video camera and then feeding the signal into an image processing computer where a surface plot of the image is plotted with normalized values.



(a) with conventional holographic recording.



(b) with nonlinear holographic recording.

Fig. 6.9. 3-D plots of the intensity correlation results.

It was noted that the full width at half maximum intensity of the auto-correlation peak in Fig. 6.9 (b) is one-fifth of that in Fig. 6.9 (a); i.e. a significant improvement in the discrimination (see section 7.4.1) of the intensity correlator has been achieved by the edge-enhancement operation.

6.5. Improved Real-Time Intensity Correlation by Moving Gratings

6.5.1 Factors Concerning The Application of a Moving Grating

It has been demonstrated in chapter 4 that the stability and the efficiency of the diffraction from gratings recorded on BSO can be considerably improved by means of a moving grating. For actual applications, however, two factors should be taken into account: first, the enhancement of the diffraction efficiency is fringe modulation dependent (Fig. 4.9); second, the optimum fringe velocity is also fringe modulation dependent (Fig. 4.8), and is proportional to the total intensity of the writing beams (Fig. 4.12). As the intensity distribution of an input on the holographic plane is usually not uniform, the fringe modulation and the total intensity of the writing beams are not uniform as well. These cause problems in the image reconstruction. In fact, with a fixed fringe velocity, the enhancement of the diffraction efficiency for different parts (or different spatial frequencies) of the recorded image is different. Thus the reconstructed image is somewhat distorted. The situation becomes more serious in Fourier transform holography, for the maximum of the Fourier power spectrum of most images is the dc peak, and the spectrum drops by several orders of magnitude at high spatial frequencies. If we choose a fringe velocity suitable for the high spatial frequency components, the diffraction from the low spatial frequency components will be suppressed seriously, and vice versa.

There are two strategies to alleviate this situation: first by adopting the Fresnel transform, and second by using edged objects. The Fresnel spectrum has a relatively uniform light distribution and can be easily controlled by selecting different Fresnel planes. The edged object has a less pronounced dc peak and so the large variations in Fourier power spectrum are avoided. However, with a coherent system, the Fresnel transform has no space invariant property, which causes object positioning problems. Also the actual objects are normally not edge-enhanced and the edge enhancement pre-processing may bring about further problems. Fortunately, with incoherent illumination the space variance of the Fresnel transform places no restrictions on the object positioning, and with a photorefractive crystal for dynamic holographic recording, edge enhancement can be realized by means of nonlinear recording in real-time. Therefore the moving grating technique is immediately appropriate to applications in real-time intensity correlation.

6.5.2. Real-Time Intensity Correlation by Moving Gratings

The configuration is the same as Fig. 6.4, except that a piezomirror is inserted in the path of the reference beam to obtain frequency detuning. Because of the nonlinear response to different parts of input 1, when the grating is moving, the intensity impulse response of the optical correlator given by Eq.(6.26) should be modified to:

$$h_i(x', y'; x, y) = |f_d(x' + x + f \sin \vartheta_0, y' + y)|^2 \quad (6.33)$$

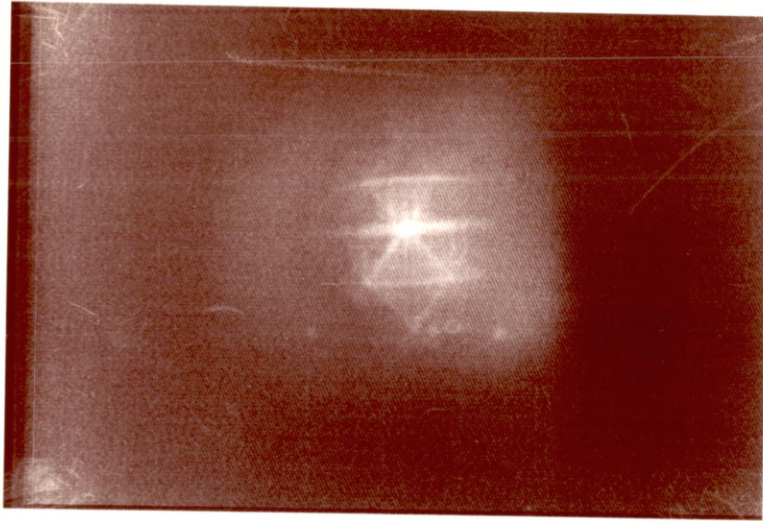
where the subscript "d" denotes the distorted image. Thus we can only obtain a cross-correlation in output when the input 2 is the same as the input 1:

$$I(x', y') = \iint_{-\infty}^{\infty} |f(x, y)|^2 |f_d(x' + x + f \sin \vartheta_0, y' + y)|^2 dx dy \quad (6.34)$$

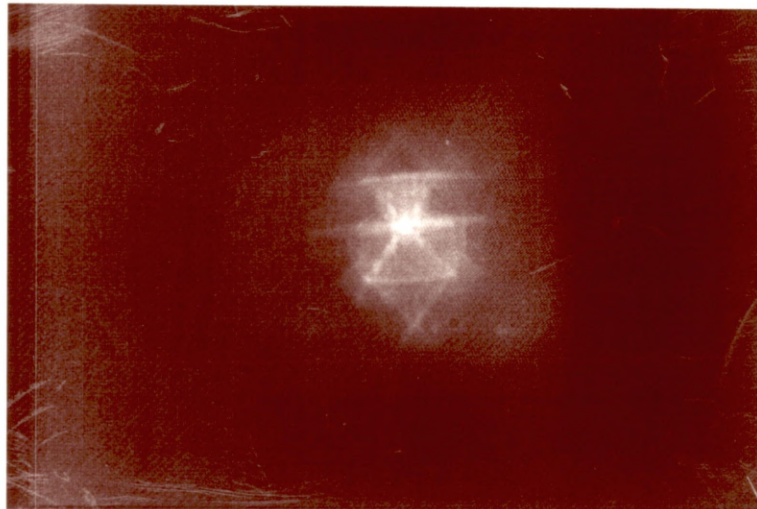
We will see that by using the Fresnel transform and an edged object, there is no obvious difference between the cross-correlation given by Eq. (6.34) and the auto-correlation of the object.

6.5.3 Experiments and Results

Although real-time edge-enhanced intensity correlation can be achieved as demonstrated in section 6.4, in this experiment we use an edged object and adopt conventional holographic recording for initial demonstrations. The edge-enhanced object is shown in Fig. 6.7. Fig. 6.10 presents the intensity correlation results, (a) is obtained with a stationary grating, while (b) is obtained with a moving grating.



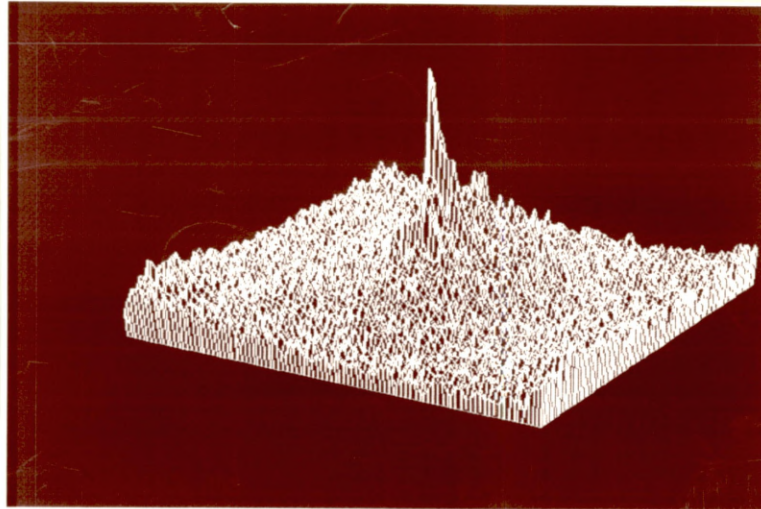
(a) with a stationary grating.



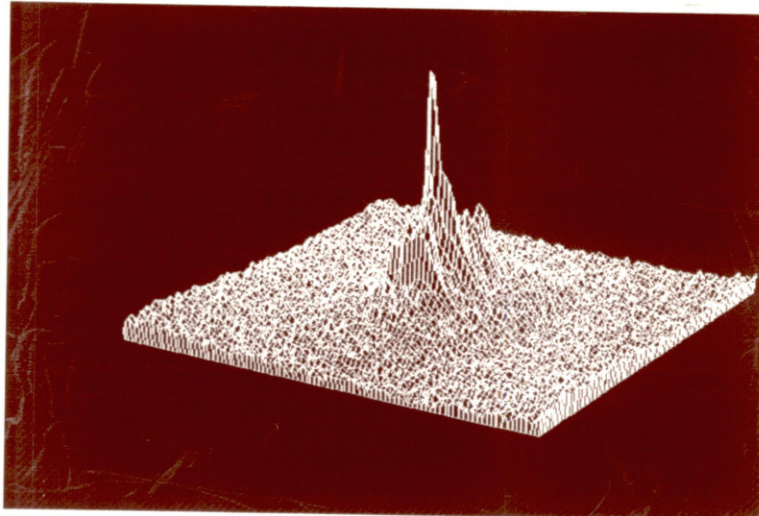
(b) with a moving grating.

Fig. 6.10. The real-time intensity correlation results with BSO crystal.

We suspect that the background noise in (b) is much lower than that in (a), showing the enhancement of the diffraction efficiency by a moving grating. To show this more clearly, Fig. 6.11 presents three-dimensional plots of Fig. 6.10. Again (a) corresponds to a stationary grating while (b) corresponds to a moving grating.



(a) Corresponding to stationary grating.



(b) Corresponding to moving grating.

Fig. 6.11. 3-D plots of the intensity correlations corresponding to Fig. 6.10.

We can see that the height of the background noise in (b) is about one-third that in (a). The enhanced signal-to-noise ratio in the output is a significant advantage in the case of noisy environments. We can also see that there is no obvious difference in the sharpness of the correlation peak between (a) and (b), although the former corresponds to the auto-correlation of the object while the latter corresponds to the

cross-correlation given in Eq. (6.34). This is because the use of the Fresnel transform filter and the edged object in this experiment alleviates the problems mentioned above.

The improvement in the stability of the peak correlation intensity is significant, in common with the data shown in Fig. 4.7 where the temporal variations of the diffracted beam are provided for both with a moving grating and with a stationary grating.

6.6. Conclusions

We have proposed a purely optical edge-enhanced intensity correlation by nonlinear holographic recording in BSO. There are alternative edge-enhancement techniques such as computer pre-processing^{6.10} and holographic derivative filtering^{6.11}. However, with a hybrid computer-optical system, the high-speed processing advantage of the optical processor is restricted by the operating speed of the computer. On the other hand, with a holographic derivative filter, the light efficiency of the optical system is quite low due to the use of two sequential optical diffraction elements. By comparison the proposed technique has the advantages of high speed processing and high light efficiency. These are of practical significance.

The dynamic holographic recording in BSO can be improved by the moving grating technique. However the dependence of the enhancement of the diffraction efficiency on the fringe modulation, and the dependence of the optimum fringe velocity on the fringe modulation and on the writing beam intensity cause a distorted reconstruction. To alleviate this effect, a Fresnel transform hologram and edge-enhanced object should be used. For normal object input, the real-time edge enhancement technique can be adopted.

The Fresnel transform in the real-time intensity correlator has the advantages of producing a more effective diffraction area within the BSO, reducing the demands on the dynamic range of the material, and alleviating the distorted reconstruction by a moving grating.

References:

- 6.1. A.Vander Lugt, "Signal detection by complex spatial filtering", IEEE Trans. Inf. Theory, **IT-10** (1964) 139-146.
- 6.2. A.W. Lohmann and H.W. Werlich, "Incoherent matched filter with Fourier holograms", Appl. Opt., **7** (1968) 561-563.
- 6.3. G.G. Mu, Z.Q. Wang, D.Q. Chen and F.X. Wu, "A new technique for pattern recognition using Fresnel hologram and extended source", Optik, **75** (1987) 97-100.
- 6.4. E. Elizur and A.A. Friesem, "Rotation-invariant correlation with incoherent light", Appl. Opt., **30** (1991) 4175-4178.
- 6.5. A.W. Lohmann and D. Mendlovic, "Circular harmonic filters for a rotation-invariant incoherent correlator", Appl. Opt., **31** (1992) 6187-6189.
- 6.6. E.G. Paek, A.V. Lehman, J.R. Wullert II and R. Martin, "Compact and robust incoherent holographic correlator using a surface-emitting laser diode array", Opt. Lett., **16** (1991) 937-939.
- 6.7. F.T.S. Yu, "Optical Information Processing", Chapter 5, John Wiley & Sons, New York, 1983.
- 6.8. J.P. Huignard and J.P. Herriau, "Real-time coherent object edge reconstruction with $\text{Bi}_{12}\text{SiO}_{20}$ crystals", Appl. Opt., **17** (1978) 2671-2672.
- 6.9. J. Feinberg, "Real-time edge enhancement using the photorefractive effect", Opt. Lett., **5** (1980) 330-332.
- 6.10. Z.Q. Wang, W.A. Gillespie, C.M. Cartwright and C. Soutar, "Real-time computer-aided multiplexed optical intensity correlator using Fresnel holographic filters and a liquid crystal television", Opt. Comm., **86** (1991) 19-24.
- 6.11. G.G. Mu, Z.Q. Wang, W.Z. Chen, "Optical intensity correlator with high discrimination", Optik, **84** (1990) 23-27.

Chapter 7 Applications of a Liquid Crystal Television in a Real-Time Optical Correlator

For a real-time optical processor the choice of a real-time input device, as well as the real-time holographic recording medium, is significant. As a type of spatial light modulator, the liquid crystal television (LCTV) has the advantages of being commercially available, inexpensive and having a colour display, and has been widely used in optical data processing^{7.1}, pattern recognition^{7.2, 7.3}, speckle metrology^{7.4}, white-light image processing^{7.5} and optical neural networks^{7.6}. As the device keeps improving in terms of resolution, contrast ratio and surface flatness, it is found to have more and more applications.

In this chapter we demonstrate that a colour LCTV can be used as a real-time input device in an intensity correlator to realize colour object recognition, and that the Epson liquid crystal display can be used to display a computer-generated synthetic discriminant function in the real-time intensity correlator to realize multi-class object recognition. Then we suggest a further research topic: using the Epson liquid crystal display to implement a new amplitude-only spatial filter, the quantized amplitude-compensated matched filter^{7.7}, in the 4-f optical system.

7.1 Optical Properties of Twisted Nematic Liquid Crystals

Fig. 7.1 shows the construction of a transmissive type, twisted nematic liquid crystal cell. It consists of two glass substrates coated on their inner surfaces with the transparent electrode, and separated by several microns from each other. A nematic liquid crystal material fills the space between the two substrates. On the inner surfaces of the substrates, an oriented fine groove structure is formed, which orients the direction of the liquid crystal molecules (director) on the surfaces. The two substrates are arranged such that the molecular directors on the surfaces are perpendicular to each other, which causes a gradual twist in orientation of the liquid crystal molecules between the substrates. To the outer surfaces of the glass substrates are attached a linear polarizer and a linear analyzer associated with the incident light and the emerging light, respectively. For the parallel arrangement, the polarization

direction of the polarizer is coincident with the molecular director on the incident surface, and the polarization direction of the analyzer is parallel to that of the polarizer.

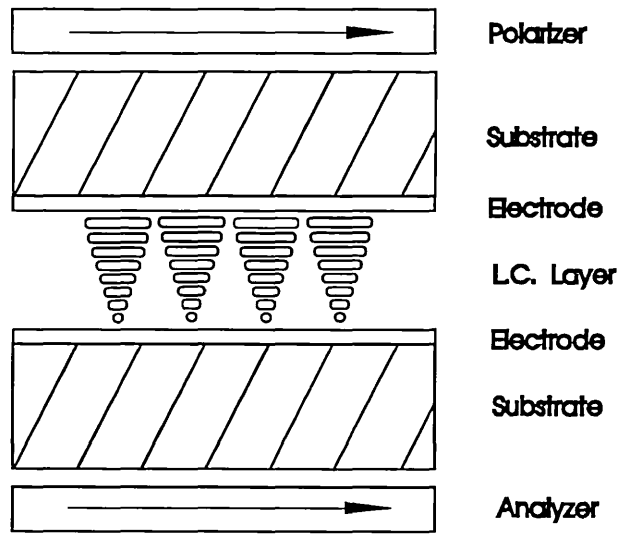


Fig. 7.1. Twisted nematic liquid crystal cell in the case without an electric field.

With no voltage applied across the liquid crystal layer, the incident polarized light, as it transverse the liquid crystal layer, is gradually twisted in its polarization direction by the liquid crystal molecules. This is the twisted nematic effect. When the light reaches the back of the cell, its polarization direction is rotated by 90° and becomes perpendicular to that of the analyzer, and the light is blocked. This is the fully "off" condition of the liquid crystal cell.

When a voltage is applied across the liquid crystal layer the direction of the molecules in the layer tends to be oriented along the direction of the applied field, as shown in Fig. 7.2. The twisted nematic effect of the liquid crystal molecules becomes weaker, and the polarization direction of the light emerging form the liquid crystal cell will not be fully perpendicular to that of the analyzer. This is "on" condition of the liquid crystal cell.

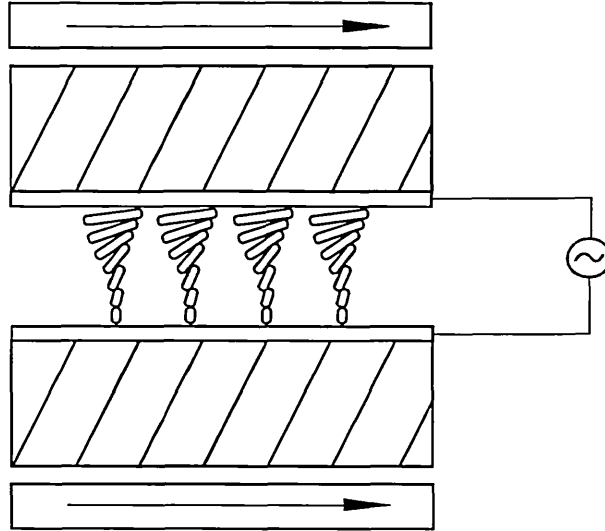


Fig. 7.2. Twisted nematic liquid crystal cell in the case with an electric field.

With a non-zero angle between the polarization direction of the polarizer and the molecular director on the incident surface, a controlled birefringence effect is involved, giving rise to the term "hybrid field effect". The voltage-dependent intensity transmission of the twisted nematic liquid crystal cell can be expressed, for the parallel polarizer and analyzer, as^{7,8}:

$$T_i = 1 - P_R^{(TN)} \left[1 - \sin^2(2\psi) \sin^2\left(\frac{\Delta\phi}{2}\right) \right] \quad (7.1)$$

where ψ is the angle between the polarization direction of the polarizer and the molecular director on the incident surface, $\Delta\phi$ is the phase retardation acquired in the liquid crystal cell, and $P_R^{(TN)}$ is the rotatory power associated with the twisted nematic effect which is given by^{7,9}:

$$P_R^{(TN)} = 1 - \frac{\sin^2\left[\frac{\pi}{2}(1+U^2)^{1/2}\right]}{1+U^2} \quad (7.2)$$

where

$$U = 2T(\Delta n)/\lambda, \quad (7.3)$$

λ is the wavelength of the incident light, T is the thickness of the liquid crystal cell, and Δn is the birefringence. The phase retardation $\Delta\phi$ is a function of the applied voltage V , and can be expressed by^{7.10}:

$$\Delta\phi = \begin{cases} \alpha\phi_m(V/V_0 - 1) & \text{when } (V/V_0 - 1) \ll 1 \\ \phi_m(1 - \beta/V) & \text{when } (V/V_0 - 1) \gg 1 \end{cases} \quad (7.4)$$

where V_0 is the threshold voltage, α and β are known functions of the elastic constants and the dielectric anisotropy of the liquid crystal, and $\phi_m = 2\pi T(n_o - n_e)/\lambda$ is the maximum phase shift with n_o and n_e being the ordinary and extraordinary refractive indexes of the liquid crystal, respectively.

7.2 Colour Image Intensity Correlation with a Colour LCTV

Colour image correlation by optical techniques is an attractive topic since all visible signals are strictly polychromatic and may not be completely described by the shape information alone. As a matter of fact, the colour information of a signal may prove more significant in distinguishing the signal from others. Therefore the extension of optical correlation from monochromatic to polychromatic signals would further enhance the capability of optical pattern recognition. The earlier works on colour image correlation were based on multiplexed volume holograms, and were carried out by Shi^{7.11}, Case^{7.12}, and Ishii and Murata^{7.13}. Their techniques have two major drawbacks: low diffraction efficiency due to multi-exposure holography, and colour cross-talk due to the spatially overlapped subholograms. Then, Yu and Chao^{7.14} proposed a grating based colour signal correlation. Their correlator possesses no colour cross talk since the subholograms for three primary colours are spatially separated. However the use of the diffraction grating reduces the light efficiency. Afterwards, Mu et al^{7.15} used a multi-wavelength Fresnel transform filter in an intensity correlator to realize colour image correlation. Mu's processor has the advantages of high light efficiency and no colour cross-talk.

For real-time colour image processing, a colour spatial light modulator is required. Most spatial light modulators have only a monochrome display, and so cannot be applied to a colour image input directly. Recently colour liquid crystal televisions have been commercially available and have been used in coherent correlators. Yu et al applied a colour LCTV to the matched filter based correlator^{7.16} and the joint transform based correlator^{7.17} for colour pattern recognition. However the colour LCTV has a serious drawback, in the coherent optical system, of the lack of space invariance even after it has been immersed in a liquid gate. This is caused by the inhomogeneity of the transparent electrodes and of the colour filter in the liquid crystal display, and by the coupled phase modulation of the liquid crystal molecules. This difficulty can be overcome by using an optical intensity correlator, where the phase variation of the LCTV, additive to the input signal, does not play a rôle. In this section we present such an optical system which uses the colour LCTV in a multi-wavelength Fresnel-transform-based intensity correlator. It possesses high light efficiency, no colour cross talk, and space invariant correlation.

7.2.1 Synthesis of a Multi-Wavelength Fresnel Transform Filter

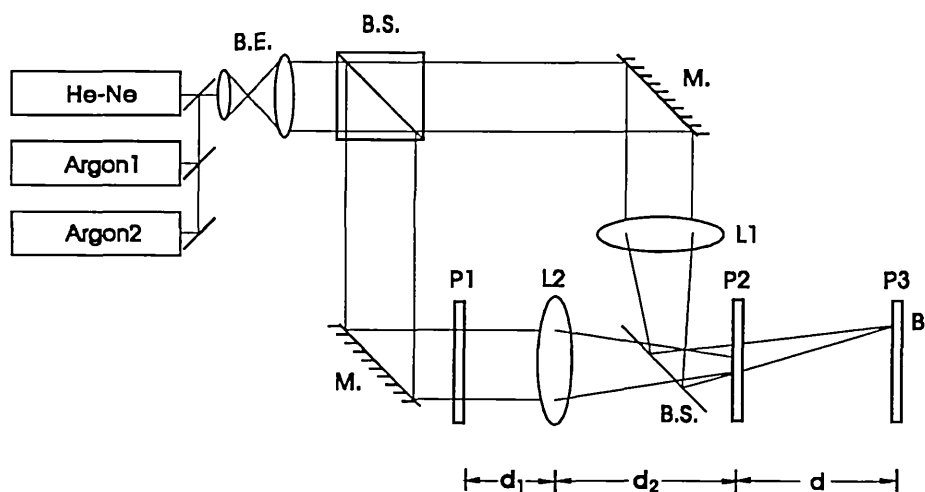


Fig. 7.3. The optical system to synthesize the multi-wavelength Fresnel holographic filters.

The optical system to synthesise the multi-wavelength Fresnel Transform filter is shown in Fig. 7.3, which is the same as Fig. 6.2, except that three primary colour lasers (red, green, and blue) are employed for the holographic recordings. A colour object is placed at the input plane P1, and a photographic plate sensitive to the three primary

colours is placed at P2. The multi-wavelength Fresnel transform filter is fabricated by sequential holographic recordings at each wavelength. With each exposure the corresponding illuminating laser beam has a suitable tilt angle to ensure that the Fresnel spectra of the three primary colour signals are spatially separated. All parameters are the same as in Fig. 6.2.

Suppose that the colour object is expressed by:

$$f(x, y) = f_r(x, y) + f_g(x, y) + f_b(x, y) \quad (7.5)$$

where the subscript r, g, and b denote the red, green, and blue colours respectively. We consider the subhologram recording process for the red information. Assume that the tilt angle of the red illuminating beam is ϑ_r . The Fresnel transform of the red signal $f_r(x, y)$ is given, similar to Eq. (6.5), by:

$$O_r(\alpha, \beta) = \iint_{-\infty}^{\infty} \exp\left(\frac{i2\pi}{\lambda_r} x \sin \vartheta_r\right) f_r(x, y) \exp\left[\frac{i\pi}{\lambda_r f_{\text{eff}}}\left(\frac{f-d_1}{f}\right)(\alpha^2 + \beta^2)\right] \exp\left[\frac{i\pi}{\lambda_r f_{\text{eff}}}\left(\frac{f-d_2}{f}\right)(x^2 + y^2)\right] \exp\left[\frac{-i2\pi}{\lambda_r f_{\text{eff}}}(x\alpha + y\beta)\right] dx dy \quad (7.6)$$

where λ_r denotes the wavelength of red laser, $\exp\left(\frac{i2\pi}{\lambda_r} x \sin \vartheta_r\right)$ denotes the tilted illuminating red laser beam. The tilt angle ϑ_r determines the location of the Fresnel spectrum at P2. As a matter of fact, Eq. (7.6) denotes a Fourier transform of a function with a linear phase shift, and the linear phase shift brings about a positional displacement in the Fourier spectrum which is also the Fresnel spectrum of the original signal.

The converging reference beam can be expressed as:

$$R_r(\alpha, \beta) = \exp\left[\frac{-i\pi}{\lambda_r d}\left[(\alpha - h_0)^2 + \beta^2\right]\right] \quad (7.7)$$

where h_0 is again the distance between the point B and the origin of P3.

After recording, the desired spatial filter for the red colour information is created. The transmittance function of the filter associated with the correlation output is given by:

$$T_r(\alpha, \beta) = O_r^*(\alpha, \beta)R_r(\alpha, \beta) \quad (7.8)$$

Similarly, the spatial filters for the green and blue information can be recorded with different tilt angles of the illuminating beams, ϑ_g and ϑ_b . The corresponding transmittances $T_g(\alpha, \beta)$ and $T_b(\alpha, \beta)$ are given by:

$$T_g(\alpha, \beta) = O_g^*(\alpha, \beta)R_g(\alpha, \beta) \quad (7.9)$$

$$T_b(\alpha, \beta) = O_b^*(\alpha, \beta)R_b(\alpha, \beta) \quad (7.10)$$

We note that by choosing suitable tilt angles of the illuminating beams, the three subholograms would be spatially separated and three primary colour filters can be correspondingly inserted in front of them. Thus high diffraction efficiency can be obtained and colour cross-talk can be eliminated.

7.2.2. Real-Time Colour Image Intensity Correlator

The real-time optical colour image correlator is shown in Fig. 7.4. A colour CCD detector views the coloured object and feeds the signal received to the colour LCTV which is illuminated by three primary colour laser beams. Lens L1 images the colour image on the LCTV onto a rotating diffuser D. L2 is the transform lens. Three primary colour filters CF are inserted in front of the three corresponding subholograms. The output signal is received by a colour CCD detector and displayed on a colour monitor.

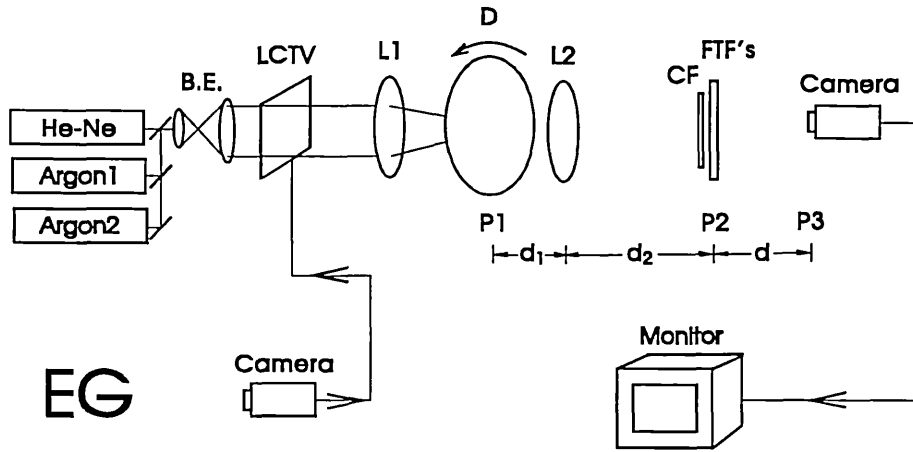


Fig. 7.4. The real-time colour image intensity correlator.

Suppose that a red input impulse $\delta_r(x - x_0, y - y_0)$ is at plane P1. With the same deduction in section 6.2.2, we can obtain the intensity impulse response which is similar to Eq. (6.12):

$$h_{ri}(x', y'; x, y) = |f_r(x + ax' - ah_0, y + ay')|^2 \quad (7.11)$$

We note that the tilt angle of the illuminating beam, ϑ_r , does not appear in the intensity impulse response. We conclude that while the tilt angles of the illuminating beam, ϑ_r , ϑ_g and ϑ_b , successfully separate three subholograms with each other, the tilt angle has no influence on the intensity impulse response.

Similarly the green intensity impulse response $h_{gi}(x', y'; x, y)$ and the blue intensity impulse response $h_{bi}(x', y'; x, y)$ can be written as:

$$h_{gi}(x', y'; x, y) = |f_g(x + ax' - ah_0, y + ay')|^2 \quad (7.12)$$

$$h_{bi}(x', y'; x, y) = |f_b(x + ax' - ah_0, y + ay')|^2 \quad (7.13)$$

For an input colour object with the intensity transmittance:

$$|f'(x, y)|^2 = |f'_r(x, y)|^2 + |f'_g(x, y)|^2 + |f'_b(x, y)|^2 \quad (7.14)$$

the output intensity at plane P3 will be given by:

$$I(x', y') = \iint \left[|f'_r(x, y)|^2 |f_r(x + ax' - h_0, y + ay')|^2 + |f'_g(x, y)|^2 |f_g(x + ax' - h_0, y + ay')|^2 + |f'_b(x, y)|^2 |f_b(x + ax' - h_0, y + ay')|^2 \right] dx dy \quad (7.15)$$

which is the colour image intensity correlation. It can be seen that there are no colour cross-talk terms in Eq. (7.15). This is because that three primary colour filters inserted in front of the corresponding subholograms filter out the redundant colour information.

7.2.3. Experimental Results

In the experiments we chose the bichromatic signal of a red "E" and a green "G" shown in Fig. 7.5 as the colour image. The extent of the two primary coloured Fresnel spectra of the colour signal was about 3.0 mm. Their spatial separation was about 1.0 mm. Agfa Gevaert 8E75 holographic plates and a bleaching process were employed for the multi-wavelength Fresnel transform filter recordings. A diffraction efficiency over 30 % was obtained. A Citizen T530 colour LCTV was used as the real-time input device. The pixel number of the LCTV screen ($5.4 \times 4.2 \text{ cm}^2$) was measured, using a travelling microscope, to be about 220×160 . With the projection of He-Ne laser light through the TV screen the contrast ratio was measured to be 10:1 (defined as the ratio of the intensities for a fully "on" pixel to a fully "off" pixel of the input).

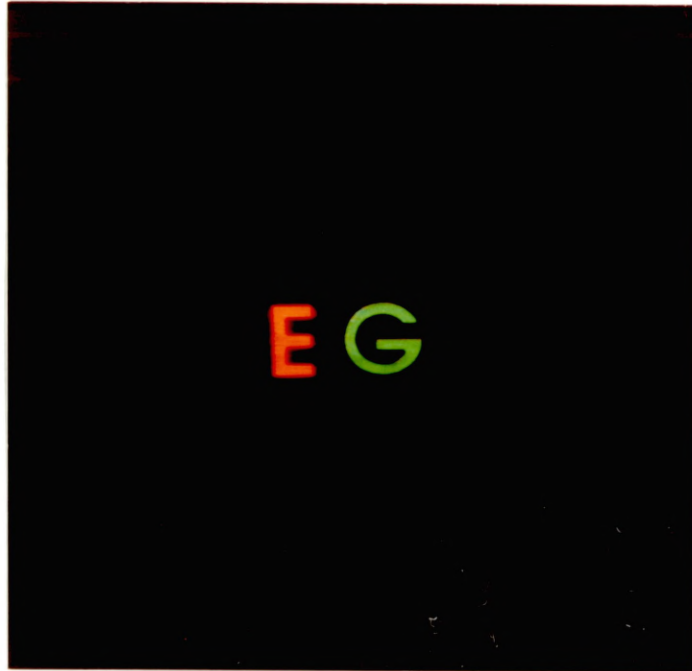


Fig. 7.5. The colour object used for the synthesis of the multi-wavelength Fresnel transform filter.

Fig. 7.6 shows the auto-correlation result when the same colour image is fed into the correlator of Fig. 7.4. There is a bright yellow colour spot in the centre. If only a red "E" or a green "G" is fed into the correlator, a red or green spot will be in the centre. Suppose a bichromatic signal of a green "E" and a red "G" is fed into the colour LCTV, which has same shape but different colour distribution with respect to the reference bichromatic signal. The red colour filter, which is in front of the subhologram recorded for "E" in the reference signal, will block the light coming from the green "E", and the green colour filter, which is in front of the subhologram recorded for "G" in the reference signal, will block the light coming from the red "G". Thus we can only get a composite of the cross-correlation of "E" and "G" in red colour and in green colour yielding a yellow cross-correlation pattern, and no bright centre spot appears in the output plane at all. Therefore the real-time correlator recognizes the colour information as well as the shape information in an object.

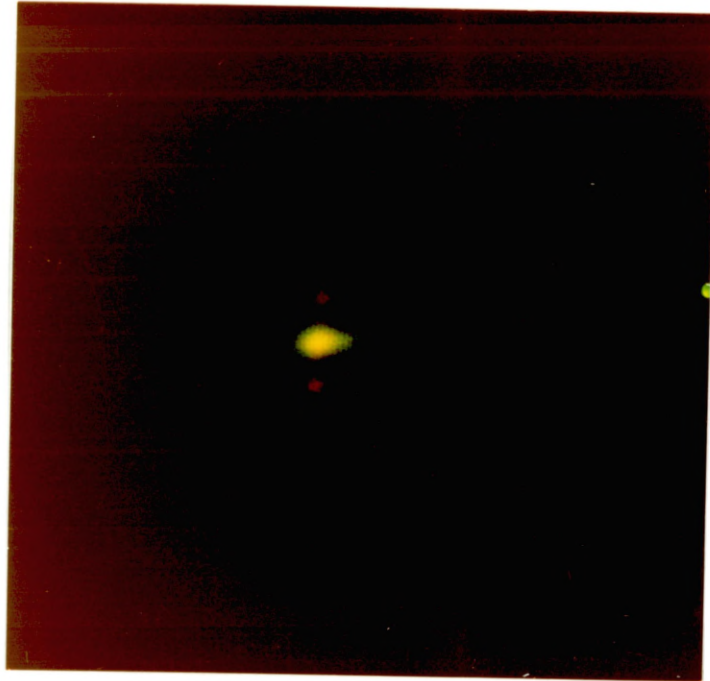


Fig. 7.6. The auto-correlation result of the colour object. The combination of the red and the green signal yields a bright yellow correlation peak.

For a complicated colour object, the colour of the auto-correlation peak lies on a specific point of the CIE chromaticity diagram^{7.18}. The object is distinguished uniquely by the combined measurements of the intensity and the chromaticity coordinates of the correlation peak. Although in our experiment three primary colour lasers were used in the correlator, an extended white-light source can be employed. In this case three narrow band colour filters^{6.3} should be employed and the rotating diffuser can be removed. We noted that the shift of the colour image in the LCTV screen, caused by the displacement of the input object, had no influence on the output correlation. By comparison, when using a coherent optical processor and an LCTV the shift usually causes severe problems due to the spatial phase variation of the LCTV screen, and a phase conjugation technique has to be employed^{7.19}.

In summary, we chose the LCTV as the real-time input device to realize colour image correlation because it is a colour spatial light modulator and is commercially available. Considering that most spatial light modulators are only monochrome

devices, the colour LCTV could play an important role in colour signal processing. However the inhomogeneity in the transparent electrodes, in the liquid crystal molecular distribution, and in the colour filters incorporated into the liquid crystal display brings about arbitrary phase variations in the input signal. We overcome this difficulty by adopting an incoherent optical system. At this stage real-time colour image holographic recording was not used, but it can be realized by using a white laser as light source, and a combination of photorefractive crystals, e.g. BSO for green and blue signals, and BTO for red signal, as the recording media.

7.3. Real-Time Intensity Correlation Using a Synthetic Discriminant Function Filter

Because of the poor contrast ratio and limited linear modulation range of the Citizen T530 LCTV, it was used to display only a binary input object. To meet the requirements for displaying a more complicated signal, such as a synthetic discriminant function (SDF), a better liquid crystal display is required. Recently, the Epson liquid crystal display projector, which has a much better modulation property^{7.20}, has become commercially available. In this section we further investigate the modulation properties of the Epson liquid crystal display, and then use it to display the synthetic discriminant function in the real-time intensity correlator to realize multi-class object recognition.

7.3.1. Modulation Properties of the Epson Liquid Crystal Display

The Epson liquid crystal display used is active-matrix addressed, with 320×220 pixel elements. The sandwich-like structure, i.e. the polarizer, the liquid crystal cell and the analyzer, of the original Epson liquid crystal display is arranged such that the polarization direction of the polarizer is parallel to the molecular director on the incident surface of the liquid crystal cell, and the analyzer is aligned so that its polarization direction is parallel to that of the polarizer. This is in fact a coupled amplitude and phase modulation mode, i.e. amplitude and phase both vary with the drive signal.

Fig. 7.7 shows the coupled modulation effect. The bright and dark horizontal lines on the right half of the field of view correspond to pixel values 255 and 0, respectively. The curved vertical interference fringes on the left half of the field of view were

obtained with a Mach-Zehnder interferometer, showing the effect of the coupled phase and amplitude modulation.

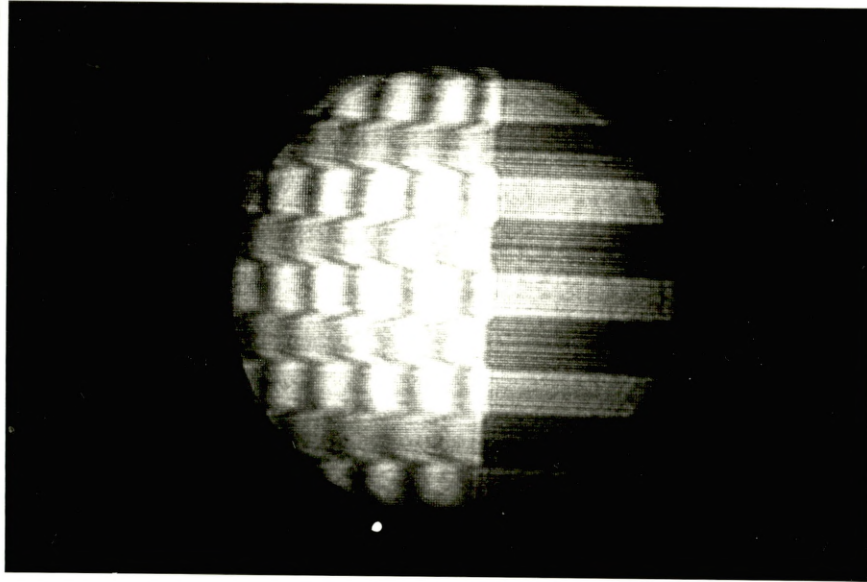


Fig. 7.7. The coupled phase and amplitude modulation characteristics of the Epson liquid crystal display in normal operation mode.

For coherent processing this coupled amplitude and phase modulation should be generally avoided (unless taken into account in the filter design), and so-called phase-mostly modulation and amplitude-mostly modulation modes have been developed^{7.21}.

It is obvious that by removing the analyser in the original arrangement, the device performs phase-mostly modulation. The maximum phase shift between an "on" and an "off" pixel depends on the setting of the bias voltage (the brightness control). Fig. 7.8 provides the achievable phase shift of the Epson liquid crystal display versus video level with the bias voltage setting yielding the maximum phase shift^{7.20}. It can be seen that the maximum phase shift is about 1.87π .

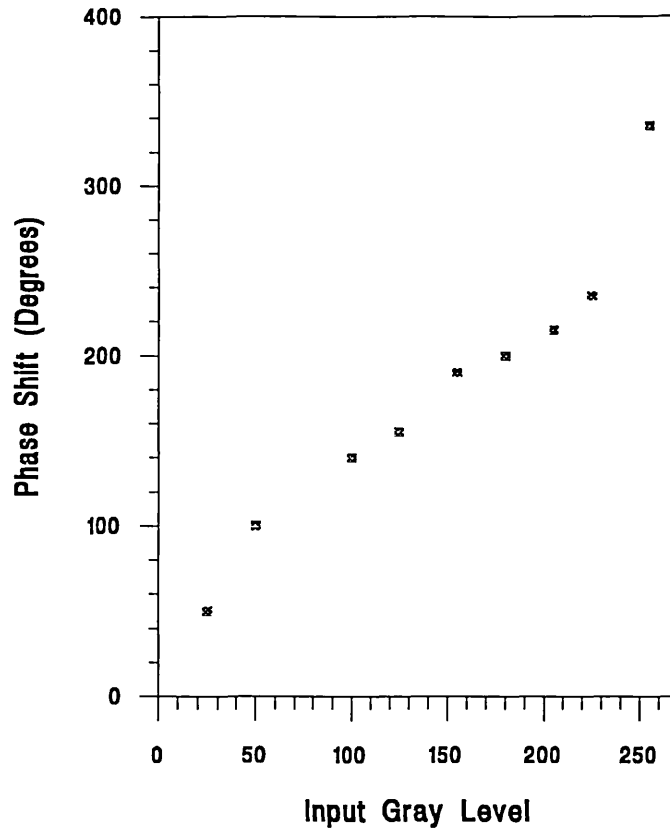


Fig. 7.8. Plot of phase shift of the Epson liquid crystal display versus video level (ref. 7.20).

The arrangement for the amplitude-mostly modulation is as follows: the polarization direction of the polarizer is perpendicular to the molecular director on the incident surface of the liquid crystal cell, and the analyzer is aligned parallel to the polarizer. This in fact displays the image with contrast reversal. Fig. 7.9 shows the effect of the amplitude-mostly modulation. The bright and dark horizontal lines on the right half now correspond to pixel values of 0 and 255, respectively. The left half of Fig. 7.9 was obtained with the Mach-Zehnder interferometer, showing the phase modulation characteristics. It can be seen that the vertical interference fringes are only slightly distorted, implying only small phase modulation.

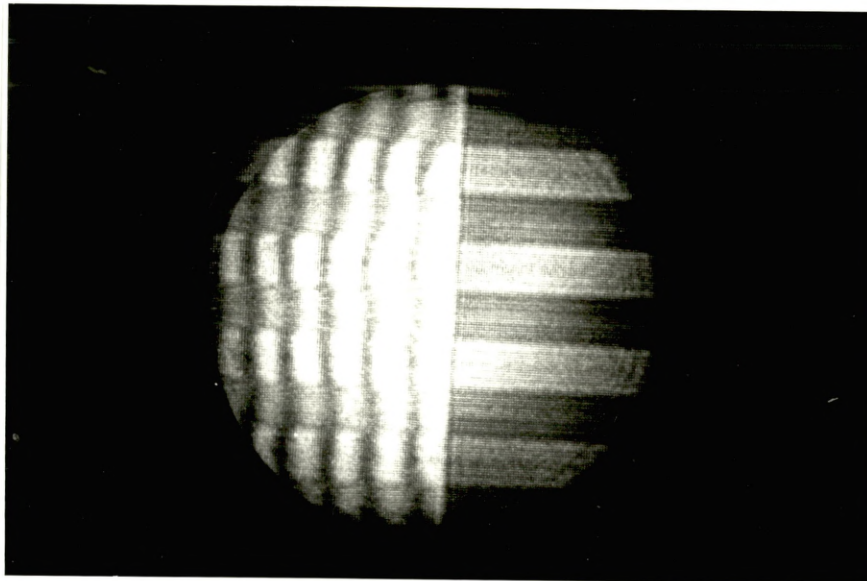


Fig. 7.9. The modulation characteristics of the Epson liquid crystal display in amplitude-mostly modulation mode.

Fig. 7.10 presents the variations of the intensity transmittance as a function of pixel value when working in the amplitude-mostly modulation mode. Three curves were obtained with different "brightness" control, B, and "contrast" control, C settings on the projector front panel. For our purpose, the best curve is with the settings of $B = 5$ and $C = 10$. It can be seen that the contrast ratio and the linear intensity modulation range of the device are poorer. For instance, the best curve has a linear relationship from grey level 45 to grey level 115 (70 grey levels of linear dynamic range) and the contrast ratio, defined as the ratio of the maximum intensity to the minimum intensity in the linear range, of 2:1.

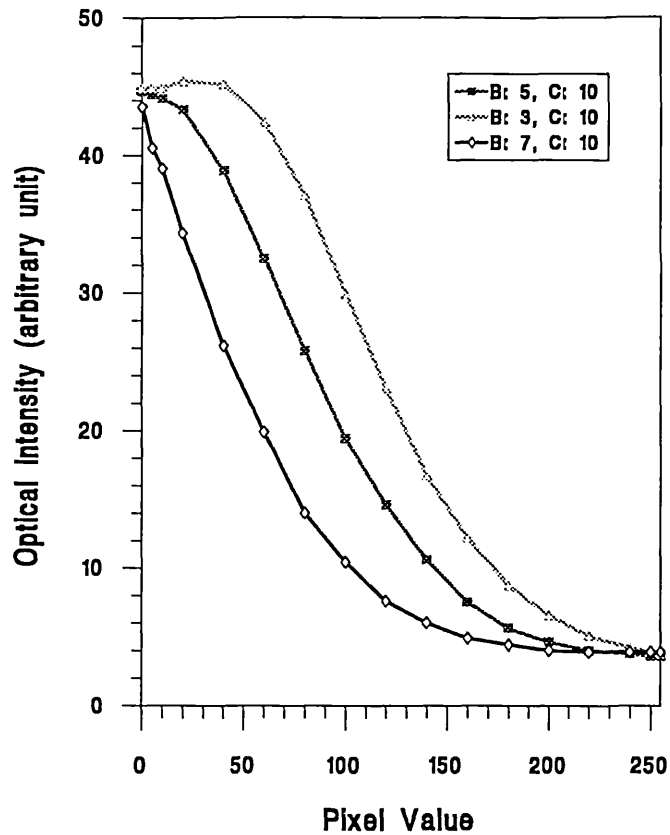


Fig. 7.10. The output intensity of the Epson liquid crystal display versus pixel value in the amplitude-mostly modulation mode.

As a comparison, Fig. 7.11 presents the measurements made with the Epson liquid crystal display operating in its normal mode. The best curve now corresponds to $B = 5$ and $C = 6.5$. The linear range is from grey level 60 to grey level 230 (170 grey levels of linear dynamic range) and the contrast ratio is 8:1. It is not surprising that the contrast ratio presented here is much smaller than that presented in reference 7.20. The definition of the contrast ratio used there is the ratio of the intensity with a fully "on" drive pixel to that with a fully "off" drive pixel.

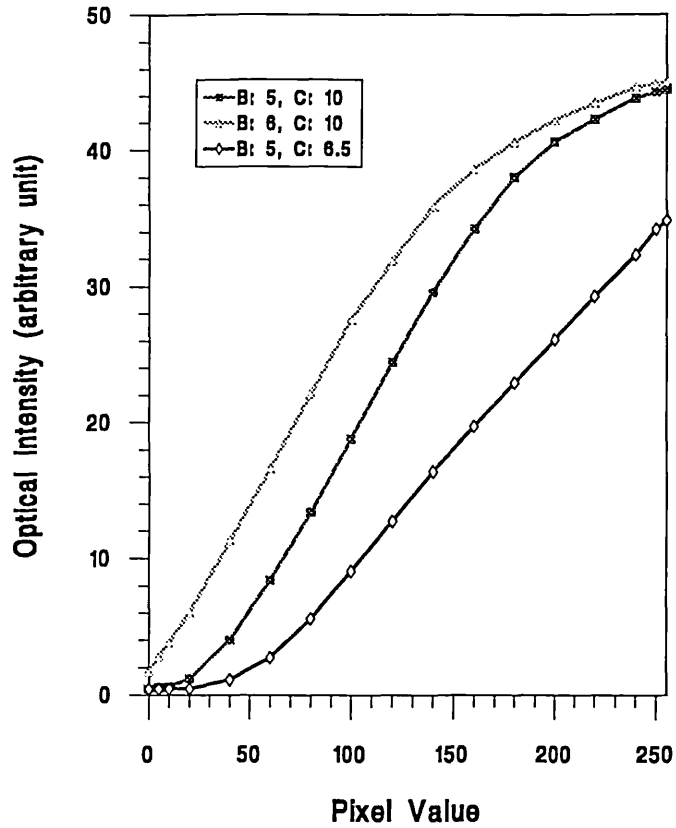


Fig. 7.11. The output intensity of the Epson liquid crystal display versus pixel value in the normal operation mode.

It is clear in comparison of Fig. 7.10 with Fig. 7.11 that the amplitude-mostly modulation mode is achieved at the cost of a deterioration in the contrast ratio and the linear modulation range of the device.

For incoherent processing, it is only the intensity of the input image that plays a role, and as such the coupled modulation of amplitude and phase has no significance. Thus we can take the advantages of the high contrast ratio and large linear intensity modulation range of the Epson liquid crystal display operating in its normal mode.

7.3.2. The Synthetic Discriminant Function

The SDF concept was originally introduced by Hester and Casasent in the context of coherent correlation^{7.22}, and since then a number of papers have been published^{7.23-7.27}. For a class of objects, the coherent SDF is formed from a weighted linear combination of the complex amplitude distribution of these objects. On the other hand, the incoherent SDF is formed from a weighted linear combination of the **intensity** distribution of these objects. The basic property of the SDF is that it possesses the same peak response for any input which belongs to the class.

Let $I_1(x, y)$, $I_2(x, y)$, ..., $I_N(x, y)$ denote the intensity distributions of a class of objects. The SDF is a composite function $s(x, y)$ such that the intensity correlation of any of these objects with the function has the same value at the origin:

$$s(x, y) = \sum_{i=1}^N a_i I_i(x, y) \quad (7.16)$$

$$s(x, y) \otimes I_i(x, y) \Big|_{\text{at origin}} = c \quad (7.17)$$

where a_i , $i = 1, 2, \dots, N$, are the appropriate coefficients, and c is a constant. To calculate this function, we seek a set of orthogonal basis functions which are linear combinations of the intensity distributions of the objects:

$$\Phi_i(x, y) = \sum_{j=1}^N b_{ij} I_j(x, y) \quad (7.18)$$

$$\Phi_i(x, y) \otimes \Phi_j(x, y) \Big|_{\text{at origin}} = \begin{cases} 0 & \text{when } i \neq j \\ 1 & \text{when } i = j \end{cases} \quad (7.19)$$

where b_{ij} , $i = 1, 2, \dots, N$ and $j = 1, 2, \dots, N$ are the coefficients which can be calculated by the Gram-Schmidt expansion approach^{7.28}. The SDF is now expressed in terms of the basis functions:

$$s(x, y) = \sum_{i=1}^N c_i \Phi_i(x, y) \quad (7.20)$$

where c_i are the coefficients which can be calculated, considering Eq. (7.19), by:

$$c_i = s(x, y) \otimes \Phi_i(x, y) \Big|_{\text{at origin}} \quad (7.21)$$

Eq. (7.21) yields, using Eqs. (7.17) and (7.18):

$$c_i = \sum_{j=1}^N c b_{ij}(x, y) \quad (7.22)$$

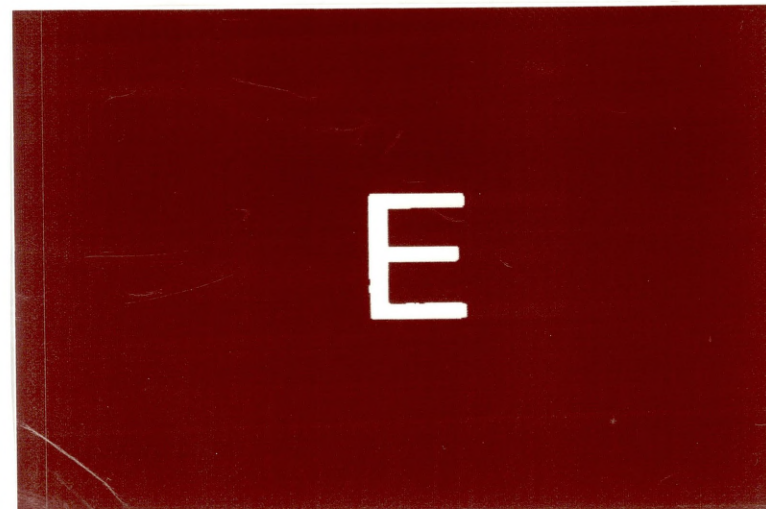
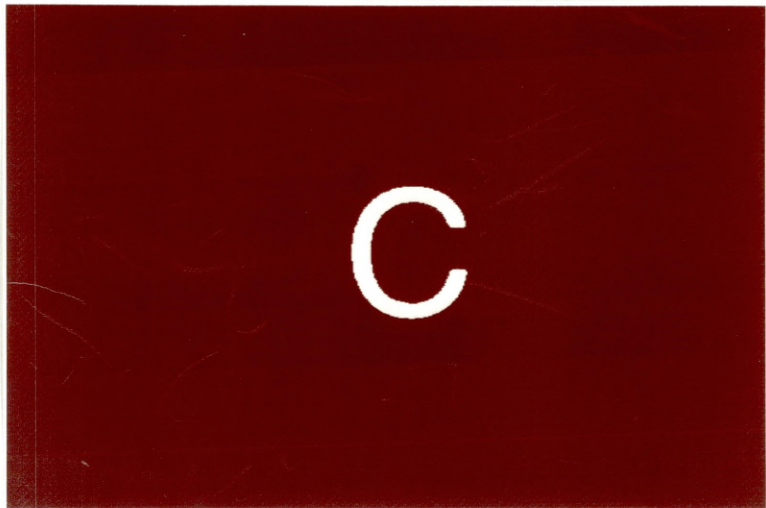
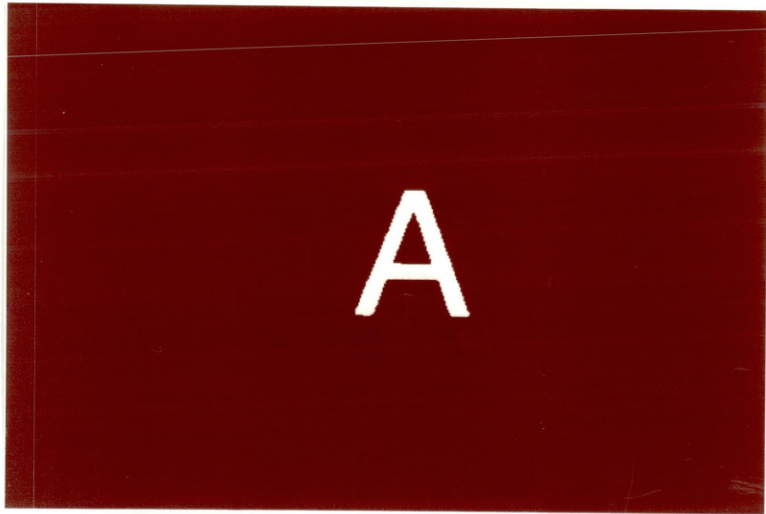
Substituting Eqs. (7.18) and (7.22) into Eq. (7.20), the SDF now can be expressed in terms of the original objects:

$$s(x, y) = \sum_{i=1}^N \sum_{j=1}^N \sum_{k=1}^N c b_{ij} b_{ik} I_k(x, y) \quad (7.23)$$

The computed SDF data are then fed into the Epson liquid crystal display incorporated in the real-time intensity correlator to produce the optical reference signal.

7.3.3. Experiments

To calculate the SDF of a class of objects, a VAXstation 3200 computer and IDL image processing software was used. The class of objects comprises five English letters "A", "C", "E", "R" and "S", as shown in Fig. 7.12. Each image consists of a 256×256 pixel array.



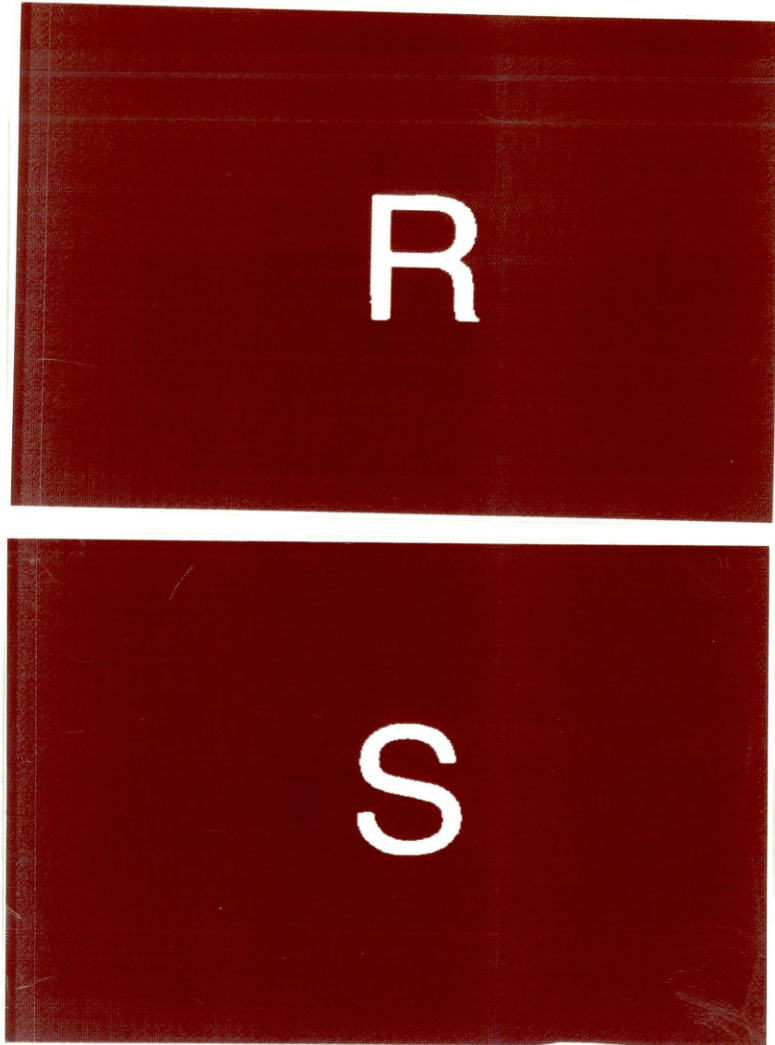


Fig. 7.12. A class of objects: five English letters.

By the procedure described in section 7.3.2, the SDF of the original objects was computed. Usually there are negative pixel values appearing in the SDF data. To overcome this difficulty, and to accommodate the linear intensity modulation range of a spatial light modulator e.g. the liquid crystal display in our case, an appropriate bias level L_1 and a scaling factor L_2 were used to modify the computed data:

$$s'(x, y) = L_1 + L_2 s(x, y) \quad (7.24)$$

where $s'(x, y)$ is the modified SDF data. L_1 and L_2 depend on the minimum and maximum pixel values in the original SDF data and the linear dynamic range of the

spatial light modulator used. When the modified SDF is fed into an intensity correlator the output intensity at the origin will be:

$$I_{\text{out}}(0,0) = L_1 \iint_{-\infty}^{\infty} I_{\text{in}}(x,y) dx dy + L_2 \iint_{-\infty}^{\infty} I_{\text{in}}(x,y) s(x,y) dx dy \quad (7.25)$$

where $I_{\text{in}}(x,y)$ is the intensity distribution in the input object. The second term in equation (7.25) satisfies the SDF requirements. The first term, however, is signal energy dependent and does not satisfy the SDF requirements. Fortunately, by measuring the total input energy, it can be subtracted from the output intensity at the origin. We should emphasize that the strategy of using an appropriate bias level and a scaling factor cannot be applied to the coherent correlator. With coherent processing, the linear physical parameter in equation (7.24) should be the complex amplitude rather than the intensity, but the detectable physical parameter is only the intensity. With a coherent optical system, the negative pixel values in the SDF data and the accommodation of the SDF data to a real spatial light modulator can be overcome by other techniques, such as incorporating the phase and amplitude cross coupling in the filter-generation algorithms^{7.29}.

The computed SDF for the five English letters, modified with a bias level and a scaling factor based on Eq. (7.24), is shown in Fig. 7.13. Obviously it is a six grey level image in this demonstration.

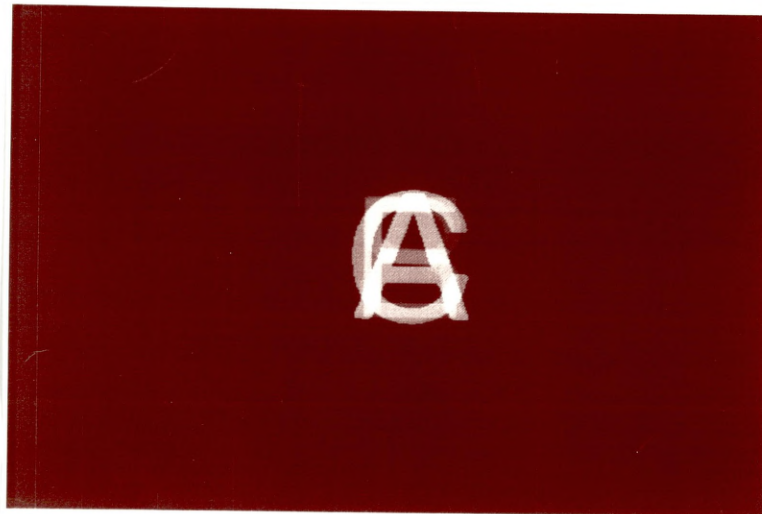


Fig. 7.13. The computed synthetic discriminant function.

The real-time intensity correlator using an Epson liquid crystal display and BSO crystal is shown in Fig. 7.14. The system is the same as Fig. 6.4 except for the liquid crystal display and the third half-wave plate were used in the writing portion. After passing through the first half-wave plate, the argon laser beam is split into two by the polarizer cube. One beam passes through the second half-wave plate, which makes the polarization direction of the beam parallel to the molecular director on the front surface of the liquid crystal cell. The Epson liquid crystal display operates in its normal operation mode. The SDF data acting as the reference signal are electronically fed into the liquid crystal display. The third half-wave plate makes the polarization direction of the beam emerging from the liquid crystal display the same as that of the second beam. L1 forms the Fresnel transform of the object. The second beam acts as the reference beam. The object to be recognized is at input 2. The system parameters are referred to Fig. 6.4.

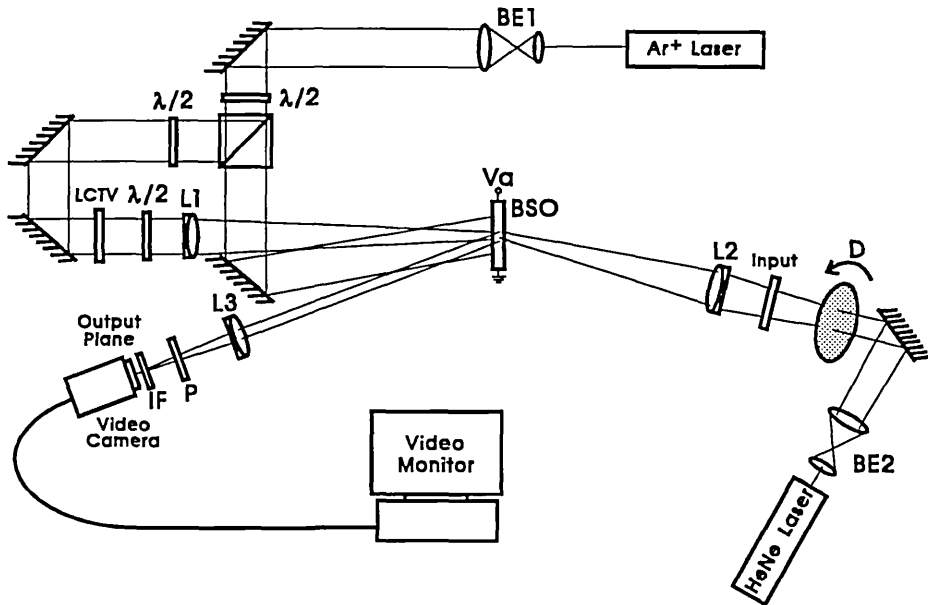


Fig. 7.14. Experimental configuration for the real-time intensity correlator using BSO crystal and Epson liquid crystal display.

The intensity impulse response of the optical system, when the SDF data is fed to the liquid crystal display, is given by [refer to Eq.(6.26)]:

$$h_i(x', y'; x, y) = s'(x' + x + f \sin \vartheta_0, y' + y) \quad (7.26)$$

Therefore when an input $I_{in}(x, y)$ is fed into the system as the input 2, the output intensity will be given by the intensity correlation of the input with the modified SDF:

$$I_{out}(x', y') = \iint_{-\infty}^{\infty} I_{in}(x, y) s'(x' + x + f \sin \vartheta_0, y' + y) dx dy \quad (7.27)$$

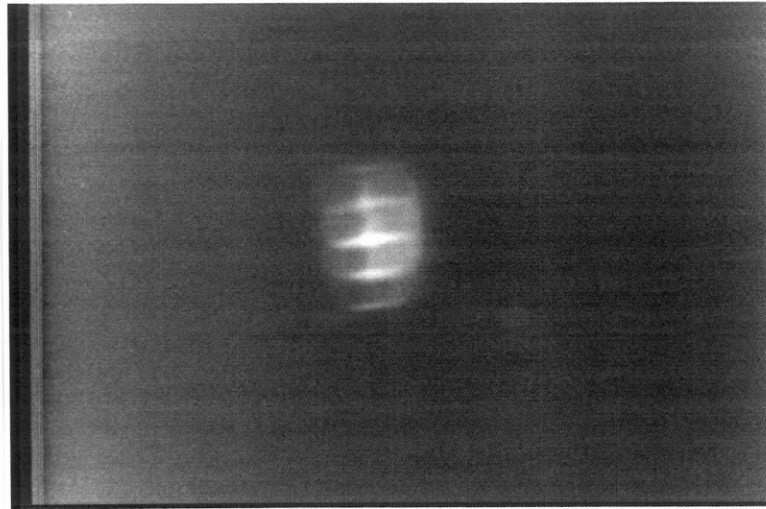
Fig. 7.15 presents the results of the intensity correlation obtained with the optical system of Fig. 7.14 when the input object belongs to the class. (a), (b), (c), (d) and (e) correspond to the input object of letter "A", "C", "E", "R" and "S", respectively. In these results we are more interested in the two dimensional distributions of the correlation patterns, which show how the optical correlator operates.



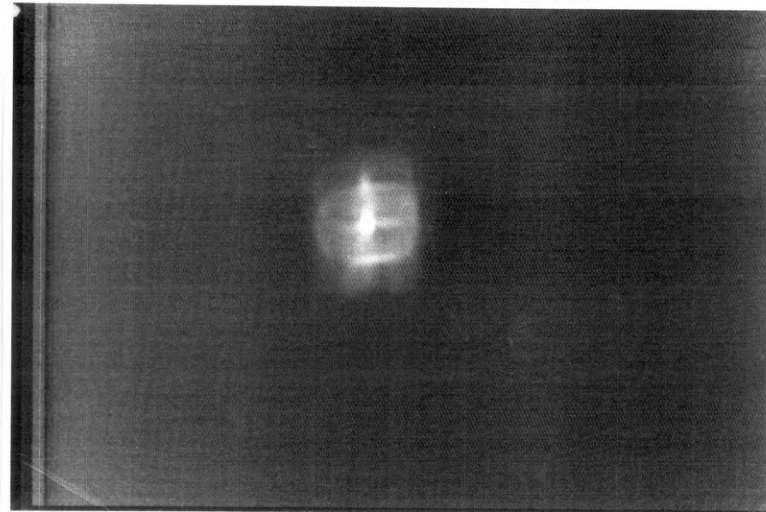
(a) Corresponding to the input of "A".



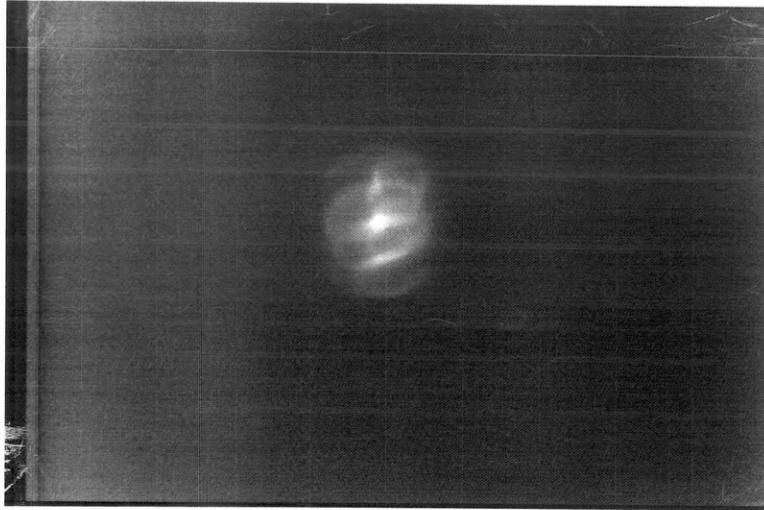
(b) Corresponding to the input of "C".



(c) Corresponding to the input of "E".



(d) Corresponding to the input of "R".



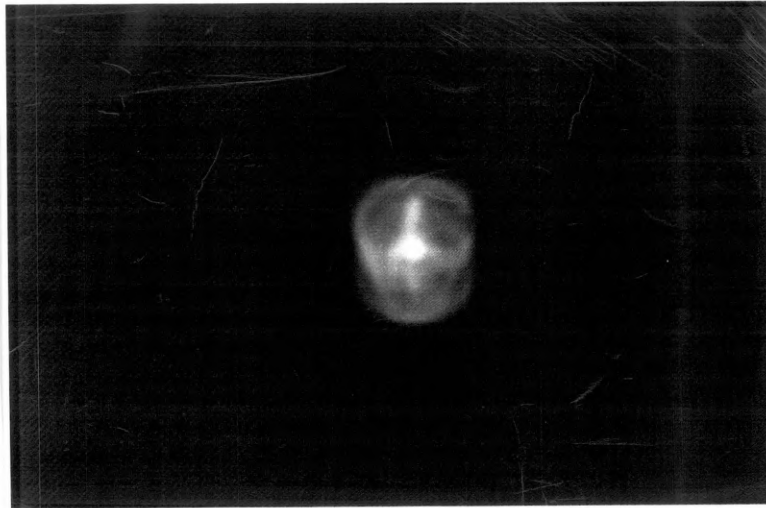
(e) Corresponding to the input of "S".

Fig. 7.15. The experimental correlation results using synthetic discriminant function.

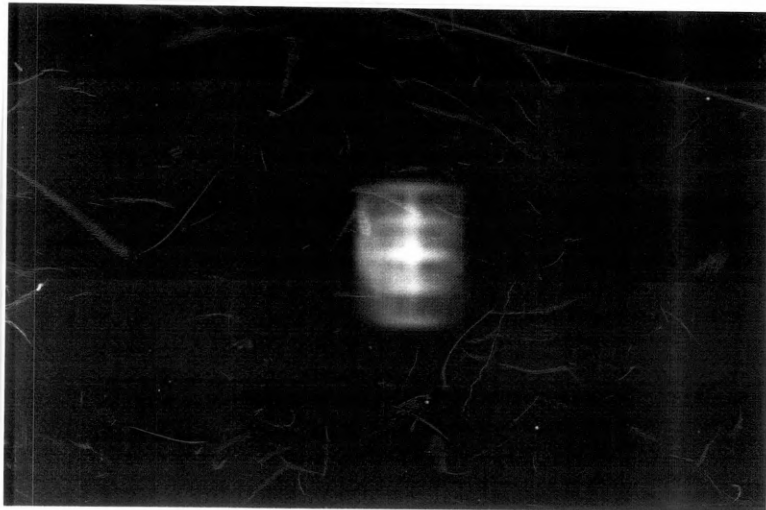
To show how the experiments are expected, Fig. 7.16 presents the computer simulation results. (a), (b), (c), (d) and (e) correspond to the input object of letter "A", "C", "E", "R", and "S", respectively. It can be seen that the optical correlation results are quite satisfactory, in agreement with the computer simulation results.



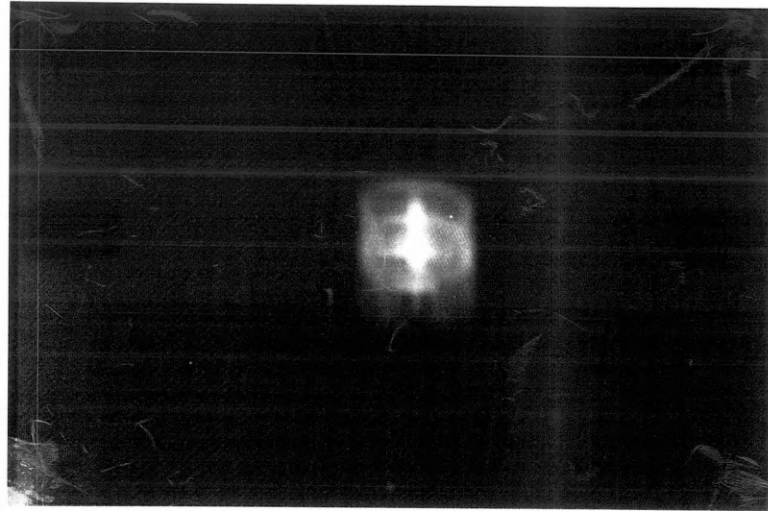
(a) Corresponding to the input of "A".



(b) Corresponding to the input of "C".



(c) Corresponding to the input of "E".



(d) Corresponding to the input of "R".



(e) Corresponding to the input of "S".

Fig. 7.16. The computer simulation results using synthetic discriminant function.

In summary, we have experimentally demonstrated real-time intensity correlation using an SDF filter. An Epson liquid crystal display operating in its normal mode was employed to display the SDF filter. It has been shown that the Epson liquid crystal display is more appropriate to the incoherent optical system, because the coupled amplitude and phase modulation in the normal operation mode has no influence in this

case, and the advantages of high contrast ratio and large linear modulation range in this operation mode can be realized.

There are two difficulties in displaying an SDF filter with a spatial light modulator: the negative pixel values in the SDF data and the accommodation to the linear dynamic range of the spatial light modulator. With a coherent system these difficulties can be overcome by incorporating the phase and amplitude cross coupling in the filter-generation algorithms. With an incoherent system these difficulties can be simply overcome by using an appropriate bias level and a scaling factor to modify the computed SDF data.

The shortcoming of the wider correlation peak in the intensity correlator can be improved by means of non-linear recording in a BSO crystal as described in chapter 6. In this case, the Epson liquid crystal display should be in the reading part to display an edge-enhanced SDF filter, and the input object should be in the writing part. The input object used in this experiment was a transparency. By using a second Epson liquid crystal display in the optical system, real-time operation could be realised.

7.4. Further Research: The Application of The LCTV to a Quantized Amplitude-Compensated Matched Filter.

We have adopted the photorefractive crystal BSO as a real-time recording material to record an optically addressed spatial filter. However, more effective spatial filters can be designed with a computer, and an electronically addressed device is required to record such a spatial filter in real time. The LCTV meets the requirement of electronic addressing, and has been used to display a matched spatial filter and a phase-only filter^{7.30, 7.31}. As further research we suggest the use of the Epson liquid crystal display operating in the amplitude-mostly modulation mode to realize a new spatial filter, the quantized amplitude-compensated matched filter.

The historical development of spatial filters are mainly in two aspects. The first aspect is aimed at simplifying the filter structure to accommodate a spatial light modulator for real-time applications. The main results are the phase-only and binary phase-only filters^{7.32-7.36}, and the amplitude encoded phase-only filter^{7.37}. The second aspect is aimed at improving the filter performance such as discrimination. The main results are the optimal binary phase-only filters^{7.38}, the optimal binary phase

and amplitude filters^{7.39}, the ternary phase amplitude filter^{7.40-7.42}, and the amplitude-compensated matched filter^{7.43, 7.44}.

The amplitude-compensated matched filter yields a discrimination superior to that of the phase-only filter and the matched spatial filter. However the filter function is a combination of the Fourier phase spectrum with an approximately inverse Fourier amplitude spectrum, and cannot be implemented with a single-parameter-modulated (phase or amplitude) spatial light modulator. The quantized amplitude-compensated matched filter is designed to overcome this difficulty. Two procedures are involved in the filter creation: first, translating the phase function of the amplitude-compensated matched filter into a two-bit amplitude; second, quantizing the amplitude function into several grey levels. Thus the new spatial filter is amplitude-modulation only with discrete levels.

7.4.1 Performance Criteria of Spatial Filters

To assess and choose a spatial filter for certain optical pattern recognition tasks, suitable criteria of filter performance is required. The first criterion is the discrimination which determines the chance of an error in pattern recognition. Horner defined the discrimination as the difference between the absolute auto-correlation and cross-correlation peak intensities. Awwal^{7.45} defined it as the difference between the normalized auto-correlation and cross-correlation peak intensities:

$$\Delta = \frac{NPI_{\text{in autocorrelation}} - NPI_{\text{in cross-correlation}}}{NPI_{\text{in autocorrelation}}} \quad (7.28)$$

where Δ denotes the discrimination and NPI denotes the normalized peak intensity. This definition is more attractive since the normalized peak intensity more effectively represents the sharpness of the correlation peak.

The second criterion is the light efficiency of the spatial filter which was first proposed by Horner. He defined it as the ratio of the total energy transferred to output plane to the energy in the input object. Caulfield^{7.46} modified the definition by using only the correlation peak intensity rather than the total energy:

$$\eta_H = \frac{\text{correlation peak intensity}}{\text{total energy in input}} \quad (7.29)$$

This modification is reasonable because it is the correlation peak intensity, rather than the total output intensity, that should be detectable. In the noisy circumstances the light efficiency becomes more critical.

The third criterion is the additive noise tolerance. It is usually assumed that the input signal is noise-free whereas in practice additive noise is inevitable. If the input noise reaches a certain level, the correlation peak will be embedded in the noise and the signal becomes undiscriminated. Therefore an optical correlator has a certain additive noise tolerance depending on the nature of the spatial filter. We define the additive noise tolerance, σ_t , as:

$$\sigma_t = \frac{\text{input noise level}}{\text{signal level}} \quad (7.30)$$

where the input noise level is that value that produces an output noise level which is less than 75 % of the correlation peak intensity.

7.4.2 Different Types of Spatial Filters

Consider the optical correlator shown in Fig. 2.2. Its performance merits depend on the spatial filter used. The matched spatial filter takes the form of the complex conjugate of the Fourier spectrum of a signal:

$$H_M(p, q) = |F(p, q)| \exp[-i\phi(p, q)] \quad (7.31)$$

where $|F(p, q)|$ is the Fourier amplitude spectrum and $\exp[i\phi(p, q)]$ is the Fourier phase spectrum. Because the energy transmission of the filter is proportional to the power spectrum of the signal, the matched spatial filter possesses highest noise tolerance. However, its discrimination and light efficiency are poor.

The phase-only filter takes the form of only the phase factor in Eq. (7.31):

$$H_p(p, q) = \exp[-i\varphi(p, q)] \quad (7.32)$$

Obviously the filter function is simpler and can be realized with a phase-modulated spatial light modulator. The phase-only filter operates without energy absorption, therefore it possesses the highest light efficiency. If an object $f(x,y)$ is fed into the optical correlator, the complex light distribution just behind the filter will be $|F(p,q)|$ compared with $|F(p,q)|^2$ in the case of a matched spatial filter. Both are a wavefront which is uniform in phase and varies in amplitude. It is the variation in the amplitude that causes a broader correlation peak in the output. Because that the variation of a function is smoother than that of its quadratic, the phase-only filter yields a sharper correlation peak which is related to a higher discrimination.

A binary phase-only filter is obtained by a sine or a cosine transform of the object. It takes the form, if using cosine transform:

$$H_{BP} = \begin{cases} +1 & \text{when } \cos[\varphi(p, q) + C(p, q)] \geq 0 \\ -1 & \text{when } \cos[\varphi(p, q) + C(p, q)] < 0 \end{cases} \quad (7.33)$$

where $C(p,q)$ is a frequency carrier. The cosine transform filter introduces a correlation term and a convolution term in the output. The correlation term is located at the coordinates corresponding to the phase factor $C(p,q)$, while the convolution term is located at the coordinates corresponding to $C(-p,-q)$. The discrimination and the light efficiency of the binary phase-only filter are lower than that of the phase-only filter, since some phase information is omitted, and an extra diffraction term is introduced. However, the filter function is further simplified and a binary phase-modulated spatial light modulator can be accommodated.

The amplitude-encoded phase-only filter takes the form:

$$H_{AE}(p, q) = \frac{1}{2} \{1 + \cos[\varphi(p, q) + C(p, q)]\} \quad (7.34)$$

It is an amplitude-only spatial filter. Compared with phase-only filter, a frequency carrier and a dc bias are introduced. The amplitude-encoded phase-only filter

produces three diffraction terms at the output: a correlation term at the position corresponding to $C(p,q)$, a convolution term at the position corresponding to $C(-p,-q)$, and a dc bias term at the origin. The correlation term has the same contour as that obtained with the phase-only filter. Therefore it possesses the same discrimination as the phase-only filter. However the light efficiency shows a big reduction due to two extra diffraction terms. Obviously, this filter is appropriate to an amplitude-modulated spatial light modulator.

The amplitude-encoded binary phase-only filter has the form:

$$H_{\text{AEB}}(p, q) = \frac{1}{2} [1 + H_{\text{BP}}(p, q)] \quad (7.35)$$

The filter only has the amplitude values of 0 and 1. The impulse response of this filter is the same as that of the binary phase-only filter except for a delta function at the origin in output plane. Therefore the amplitude encoding procedure deteriorates the light efficiency alone. However the filter function is very simple, and a binary amplitude-modulated spatial light modulator can be used.

The amplitude-compensated matched filter is a type of approximate inverse filter, which consists of two different filtering functions. It takes the form of a phase-only filter where the modulus of the Fourier amplitude spectrum is lower than a threshold value, and takes the form of an inverse filter where the modulus of the Fourier amplitude spectrum is higher than the threshold value:

$$H_{\text{AC}}(p, q) = \begin{cases} H_p(p, q) & \text{when } |F(p, q)| < F_0 \\ \frac{F_0}{|F(p, q)|} H_p(p, q) & \text{when } |F(p, q)| \geq F_0 \end{cases} \quad (7.36)$$

where F_0 is the threshold value. If an object of $f(x,y)$ is fed into the optical correlator, the filtered wavefront will be not only uniform in phase but also with reduced variations in amplitude, which makes the correlation peak much sharper. This type of filter is inherently energy absorptive, and the total signal energy transferred to the output plane is much lower than that with any other type of filters. Therefore the

noise tolerance is poor. However, the correlation performance does not suffer seriously because the absorption mainly takes place at the region of low spatial frequency which has less energy contribution to the correlation peak^{7.47}.

7.4.3. A New Quantized Amplitude-Compensated Matched Filter

Applying the concept of the Fourier amplitude compensation into the amplitude-encoded binary phase-only filter, we might create a new spatial filter, the amplitude-compensated and amplitude-encoded binary phase-only filter, which has the form:

$$H_{ACBP}(p, q) = \begin{cases} H_{AEB}(p, q) & \text{when } |F(p, q)| \leq F_0 \\ F_0 H_{AEB}(p, q) / |F(p, q)| & \text{otherwise} \end{cases} \quad (7.37)$$

It takes the form of the amplitude encoded binary phase-only filter when the Fourier amplitude is less than a threshold value F_0 , and it has an inverse Fourier amplitude absorptive factor otherwise. This filter can be realized by an amplitude-modulated spatial light modulator.

To further simplify the filter function, the inverse Fourier amplitude spectrum can be quantized into several discrete levels, i.e. the quantized amplitude-compensated matched filter. In this simulation we adopted four-level quantization:

$$H_{QAC}(p, q) = \begin{cases} H_{AEB}(p, q) & \text{when } |F(p, q)| \leq F_1 \\ F_1 H_{AEB}(p, q) / F_2 & \text{when } F_1 < |F(p, q)| \leq F_2 \\ F_1 H_{AEB}(p, q) / F_3 & \text{when } F_2 < |F(p, q)| \leq F_3 \\ 0 & \text{otherwise} \end{cases} \quad (7.38)$$

where F_1 , F_2 and F_3 are the threshold values which were chosen by examining the histogram of the Fourier amplitude spectrum of the object. Note that $H_{AEB}(p, q)$ is an amplitude filter with the values of 0 and 1, therefore the quantized amplitude-compensated matched filter is a four-grey-level amplitude filter.

We verify the performance merits of the quantized amplitude-compensated matched filter by means of computer simulations. Two very similar English letters shown in Fig. 7.17 were created and used as the objects, each of 48×96 pixels. This is because we adopted a 256×256 pixel computation, and the correlation plane is two-fifths of the output plane. The restricted object size ensures that the correlation peak can be separated from the zero order diffraction. The letter "G" was used as the original object, from which different types of filters were created. The auto-correlation of the letter "G" and the cross-correlation of the letter "G" with the letter "C" were then computed, and the performance merits of different type of filters were compared.

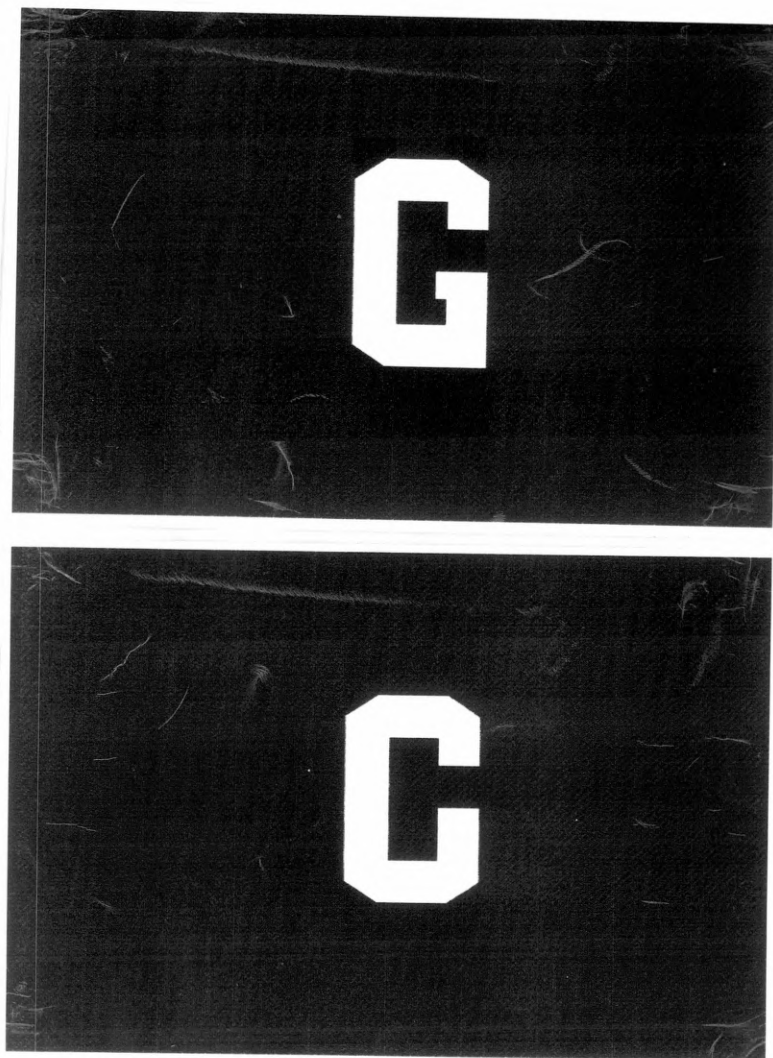


Fig. 7.17. The objects used for computer simulation. Letter "G" was used to form different type of spatial filters.

We compared the performance merits among the binary phase-only filter (BPOF), the amplitude encoded binary phase-only filter (AEBPOF), the amplitude-compensated matched filter (ACMF), the amplitude-compensated and amplitude-encoded binary phase-only filter (ACAEBPOF), and the quantized amplitude-compensated matched filter (QACMF). The threshold values were selected according to the requirements of discrimination and light efficiency, and by checking the histogram of the Fourier amplitude spectrum of the object. For the amplitude-compensated matched filter and the amplitude-compensated and amplitude-encoded binary phase-only filter in this simulation, the threshold F_0 is one-thirtieth of the maximum Fourier amplitude spectrum of the object. The thresholds of F_1 , F_2 and F_3 for the quantized amplitude-compensated matched filter are one-thirtieth, one-tenth and one-third of the maximum Fourier amplitude spectrum of the object respectively.

Table 1 shows the simulation results. Column 2 lists the type of the spatial filters. Column 3-8 list the total output energy (TOE), the absolute peak correlation intensity (APCI), the normalized peak correlation intensity (NPCI), the light efficiency η_H , the discrimination Δ , and the noise tolerance σ_t respectively. The total output energy and the absolute peak correlation intensity were normalized by setting the absolute peak correlation intensity in row 4 as one. The normalized peak correlation intensity, which represents the sharpness of the correlation peak, were obtained by dividing the absolute peak correlation intensity by the total energy in the correlation plane (part of the output plane) and then scaling it to 0-255 levels.

Table 7.1. Computer Simulation Results with Different Spatial Filters

Row	Filter	TOE	APCI	NPCI	$\eta_H(\%)$	$\Delta(\%)$	σ_T
1	BPOF	336.9	7.29	11.7	2.06	17.4	1.2
2	AEBPOF	184.8	1.82	11.3	0.52	17.1	1.2
3	ACAEBPOF	21.5	1.14	54.4	0.32	25.7	1.0
4	QACMF	16.2	1.00	61.2	0.28	25.7	1.0
5	ACMF	42.9	11.16	66.4	3.16	26.6	1.5

Key: BPOF: binary phase-only filter; AEBPOF: amplitude encoded binary phase-only filter; ACAEBPOF: amplitude-compensated and amplitude-encoded binary phase-only filter; QACMF: quantized amplitude-compensated matched filter; ACMF: amplitude-compensated matched filter.

The comparison of the performance of the amplitude encoded binary phase-only filter (row 2) with binary phase-only filter (row 1) shows the effects of the amplitude encoding procedure of the phase. The total output energy in row 2 drops by 45 % from that in row 1, while the absolute peak correlation intensity drops by 75 %. This is caused by the additional zero diffraction as well as the filter absorption. However, the normalized peak correlation intensity only changes slightly, which indicates that the sharpness of the correlation peak is preserved. Also the light efficiency drops from 2.06 % to 0.52 % while the discrimination keeps the same value.

The comparison of the performance of the amplitude-compensated and amplitude-encoded binary phase-only filter (row 3) with the amplitude encoded binary phase-only filter (row 2) shows the effects of the amplitude compensation procedure. The absolute peak correlation intensity in row 3 drops by 37 % from that in row 2. Considering the loss in the total output energy, which drops by 88 %, the loss in the absolute peak correlation intensity is not serious. The normalized peak correlation intensity, on the other hand, increases by 381 %, which is a significant improvement. Also the discrimination increases from 17.1 % to 25.7 %, while the light efficiency drops from 0.52 % to 0.32 % and the noise tolerance drops slightly.

The comparison of the performance of the quantized amplitude-compensated matched filter (row 4) with the amplitude-compensated and amplitude-encoded binary phase-only filter (row 3) shows the effects of the amplitude quantization procedure. We note that the filter performance has no noticeable deterioration. The light efficiency only drops from 0.32 % in row 3 to 0.28 % in row 4, and the discrimination and the noise tolerance maintain the same values.

In a comparison of the quantized amplitude-compensated matched filter (row 4) with the amplitude-compensated matched filter (row 5), we can see that there is a bigger drop in the total output energy and the absolute peak correlation intensity from row 5 to row 4. These are caused by the amplitude encoding procedure as well as the binarization procedure. However the normalized peak correlation intensity drops slightly. Also, the discrimination is preserved, with the quantized amplitude-compensated matched filter, but the light efficiency and the noise tolerance deteriorate. As a remedy to the poor light efficiency, a better output detector with higher sensitivity should be used.

In summary, the new quantized amplitude-compensated matched filter, is characterized as discrete-amplitude modulation only, and an amplitude-modulated spatial light modulator could be used. Compared with the amplitude-compensated matched filter, which cannot be realized with a single-parameter modulated spatial light modulator, the discrimination is preserved. Compared with the performance of the amplitude encoded binary phase-only filter, the improvement in the discrimination is very attractive. Therefore the quantized amplitude-compensated matched filter would be a reasonable choice for both good performance merits and real-time realization.

7.4.4 Application of The Epson Liquid Crystal Display to The Quantized Amplitude-Compensated Matched Filter

As we have seen in section 7.3 that the Epson liquid crystal display can perform amplitude-mostly modulation with contrast reversal. Fig. 7.10 presented the intensity modulation characteristics in this operation mode, which shows that the contrast ratio is poor in the linear modulation range. However, for the discrete four-level amplitude modulation, we can always set the pixels which give the maximum and the minimum outputs of the liquid crystal display as the highest and the lowest transmittances in the

filtering function, and set the pixels which gives the outputs corresponding to another two transmittances in the filtering function, without consideration of the linear modulation range. In this way the Epson liquid crystal display, even if working in the amplitude-mostly modulation mode, can provide a higher contrast ratio for displaying the quantized amplitude-compensated matched filter.

Fig. 7.18 shows a possible coherent optical correlator which uses the Epson liquid crystal display to generate a quantized amplitude-compensated matched filter. It is essentially the 4-f optical correlation system.

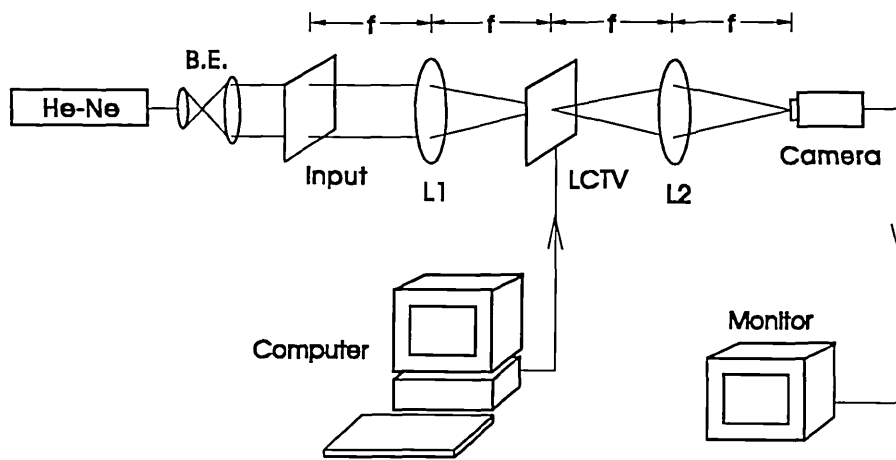


Fig. 7.18. An optical correlator using Epson liquid crystal display to generate a quantized amplitude-compensated matched filter.

In Fig. 7.18, L1 and L2 are the transform lenses. An Epson liquid crystal display is placed at the back focal plane of L1 acting as a spatial light modulator, and a CCD detector is placed at the back focal plane of L2 acting as an output receiver. The computed quantized amplitude-compensated matched filter data are electronically fed into the Epson liquid crystal display, operating in the amplitude-mostly modulation mode, resulting in corresponding transmittances. L1 forms the Fourier transform of the input onto the liquid crystal display, and L2 forms the inverse Fourier transform of the filtered complex light field onto the CCD detector. The correlation output is then fed into a monitor where the input object can be recognized by a suitable threshold setting of the device.

7.5 Conclusions

We have demonstrated that colour image recognition can be realized by using a normal colour LCTV as the real-time input device in an intensity correlator. If a photorefractive crystal or a combination of crystals and a white-light laser are used in the system, real-time colour image holographic recording can also be realized^{7,48}.

Multi-class object recognition can be achieved by using a synthetic discriminant function filter displayed on an Epson liquid crystal display in the real-time intensity correlator. This is, to our knowledge, the first optical realization of the synthetic discriminant function. We have shown a specific application of the real-time intensity correlation using BSO and liquid crystal display. The established optical system has immediate applications to optical neural networks.

The proposed quantized amplitude-compensated matched filter possesses good discrimination and can be implemented with an Epson liquid crystal display operating at its amplitude-mostly modulation mode. This is an interesting research topic in optical pattern recognition.

References:

- 7.1. H.K.Liu, J.A. Davis and R.A. Lully, "Optical-data-processing properties of a liquid-crystal television spatial light modulator", *Opt. Lett.*, **10** (1985) 635-637.
- 7.2. D.A. Gregory, "Real-time pattern recognition using a modified liquid crystal television", *Appl. Opt.*, **25** (1986) 467-469.
- 7.3. F.T.S. Yu, S. Jutamulia, T.W. Lin and D.A. Gregory, "Adaptive real-time pattern recognition using a liquid crystal TV based joint transform correlator", *Appl. Opt.*, **26** (1987) 1370-1372.
- 7.4. B. Bates and P.C. Miller, "Liquid crystal television in speckle metrology", *Appl. Opt.*, **27** (1987) 2816-2817.

- 7.5. F.T.S. Yu, S. Jutamulia and X.L. Huang, "Experimental application of low-cost liquid crystal TV to white-light optical signal processing", *Appl. Opt.*, **25** (1986) 3324-3326.
- 7.6. F.T.S. Yu, T. Lu, X.Y. Yang and D.A. Gregory, "Optical neural network with pocket-size liquid-crystal televisions", *Opt. Lett.*, **15** (1990) 863-865.
- 7.7. Z.Q. Wang, C.M. Cartwright, W.A. Gillespie and C. Soutar, "An optical matched filter using a quantized amplitude compensation technique"; *Optik*, **94** (1993) 78-82.
- 7.8. U. Efron, S.T. Wu and T.D. Bates, "Nematic liquid crystals for spatial light modulators: recent studies", *J. Opt. Soc. Am. B*, **3** (1986) 247.
- 7.9. C.H. Gooch and H.A. Tarry, "The optical properties of twisted nematic liquid crystal structures with twist angle $\leq 90^\circ$ ", *J. Phys. D: Appl. Phys.*, **8** (1975) 1575-1584.
- 7.10 F.J. Kahn, "Electric-field-induced orientational deformation of nematic liquid crystals: tuneable birefringence", *Appl. Phys. Lett.*, **20** (1972) 199-201.
- 7.11. N.K. Shi, "Color-sensitive spatial filters", *Opt. Lett.*, **3** (1978) 85-87.
- 7.12. S.K. Case, "Pattern recognition with wavelength-multiplexed filters", *Appl. Opt.*, **18** (1979) 1890-1894.
- 7.13. Y. Ishii and K. Murata, "Colour-coded character-recognition experiment with wavelength-triplexed, reflection-type holographic filters", *Opt. Lett.*, **7** (1982) 230-232.
- 7.14. F.T.S. Yu and T.H. Chao, "Colour signal correlation detection by matched spatial filtering", *Appl. Phys. B*, **32** (1983) 1-6.
- 7.15. G.G. Mu, D.Q. Chen and Z.Q. Wang, "Colour-image correlation with a multiwavelength Fresnel holographic filter", *Opt. Lett.*, **13** (1988) 434-436.

- 7.16. F.T.S. Yu, S. Jutamulia and T.W. Lin, "Real-time polychromatic signal detection using a colour liquid crystal television", *Opt. Eng.*, **26** (1987) 453-459.
- 7.17. F.T.S. Yu, S. Jutamulia, R.V. Yelamarty and D.A. Gregory, "Adaptive joint transform correlator for real-time colour pattern recognition", *Opt. & Laser Tech.*, **21** (1989) 189-192.
- 7.18. W.D. Wright, "The Measurement of Colour", Chapter 4, Adam Hilger Ltd., London, 1969.
- 7.19. D. Casasent and S.F. Xia, "Phase correction of light modulators", *Opt. Lett.*, **11** (1986) 398-400.
- 7.20. J.C. Kirsch, D.A. Gregory, M.W. Thie and B.K. Jones, "Modulation characteristics of the Epson liquid crystal television", *Opt. Eng.*, **31** (1992) 963-969.
- 7.21. D.A. Gregory, J.C. Kirsch and E.C. Tam, "Full complex modulation using liquid-crystal television", *Appl. Opt.*, **31** (1992) 163-165.
- 7.22. C.F. Hester and D. Casasent, "Multivariant technique for multiclass pattern recognition", *Appl. Opt.*, **19** (1980) 1758-1761.
- 7.23. B.V.K. Vijaya Kumar, "Minimum-variance synthetic discriminant functions", *J. Opt. Soc. Am. A*, **3** (1986) 1579-1584.
- 7.24. A. Mahalanobis, B.V.K. Vijaya Kumar and D. Casasent, "Minimum average correlation energy filters", *Appl. Opt.*, **26** (1987) 3633-3640.
- 7.25. J.L. Horner and P.D. Gianino, "Applying the phase-only filter concept to the synthetic discriminant function correlation filter", *Appl. Opt.*, **24** (1985) 851-855.
- 7.26. Z. Bahri and B.V.K. Vijaya Kumar, "Generalized synthetic discriminant functions", *J. Opt. Soc. Am. A*, **5** (1988) 562-571.
- 7.27. G. Zalman and J. Shamir, "Maximum discrimination filter", *J. Opt. Soc. Am. A*, **8** (1991) 814-821.

- 7.28. J. Wozencraft and I. Jacobs, "Principles of Communication Engineering", Chapter 4, (Wiley, New York, 1965).
- 7.29. R.D. Juday, "Correlation with a spatial light modulator having phase and amplitude cross coupling", *Appl. Opt.*, **28** (1989) 4865-4869.
- 7.30. N. Clark, C.M. Crandall and M.K. Giles, "Using liquid crystal TV's in Vander Lugt optical correlators", *Proc. SPIE*, **1564** (1991) 439-451.
- 7.31. D.A. Gregory, J.A. Loudin, J.C. Kirsch, E.C. Tam and F.T.S. Yu, "Using the hybrid modulating properties of liquid crystal television", *Appl. Opt.*, **30** (1991) 1374-1378.
- 7.32. J.L. Horner and P.D. Gianino, "Phase-only matched filtering", *Appl. Opt.*, **23** (1984) 812-816.
- 7.33. J.L. Horner and J. Leger, "Pattern recognition with binary phase-only filters", *Appl. Opt.*, **24** (1985) 609-611.
- 7.34. D.M. Cottrell, R.A. Lilly, J.A. Davis and T. Day, "Optical correlator performance of binary phase-only filters using Fourier and Hartley transforms", *Appl. Opt.*, **26** (1987) 3755-3761.
- 7.35. L. Leclerc, Y. Sheng and H.H. Arsenault, "Rotation invariant phase-only and binary phase-only correlation", *Appl. Opt.*, **28** (1989) 1251-1256.
- 7.36. L. Leclerc, Y. Sheng and H.H. Arsenault, "Optical binary phase-only filters for circular harmonic correlations", *Appl. Opt.*, **30** (1991) 4643-4649.
- 7.37. M.A. Flavin and J.L. Horner, "Amplitude encoded phase-only filters", *Appl. Opt.*, **28** (1989) 1692-1696.
- 7.38. M.W. Farn and J.W. Goodman, "Optimal binary phase-only matched filters", *Appl. Opt.*, **27** (1988) 4431-4437.

- 7.39. J.D. Downie, "Design of optimal binary phase and amplitude filters for maximization of correlation peak sharpness", *Opt. Lett.*, **16** (1991) 508-510.
- 7.40. B.V.K. Vijaya Kumar and Z. Bahri, "Phase-only filters with improved signal to noise ratio", *Appl. Opt.*, **28** (1989) 250-257.
- 7.41. B.V.K. Vijaya Kumar and Z. Bahri, "Efficient algorithm for designing a ternary valued filter yielding maximum signal to noise ratio", *Appl. Opt.*, **28** (1989) 1919-1925.
- 7.42. D.L. Flannery, J.S. Loomis and M.E. Milkovich, "Transform-ratio ternary phase-amplitude filter formulation for improved correlation discrimination", *Appl. Opt.*, **27** (1988) 4079-4083.
- 7.43. G.G. Mu, X.M. Wang and Z.Q. Wang, "Amplitude-compensated matched Filtering", *Appl. Opt.*, **27** (1988) 3461-3463.
- 7.44. Y. Sun, Z.Q. Wang and G.G. Mu, "Amplitude compensated matched filters using circular harmonic expansion and a Mellin transform", *Appl. Opt.*, **29** (1990) 4779-4783.
- 7.45. A.S. Awwal, M.A. Karim and S.R. Jahan, "Improved correlation discrimination using an amplitude-modulated phase-only filter", *Appl. Opt.*, **29** (1990) 233-236.
- 7.46. H.J. Caulfield, "Role of the Horner efficiency in the optimization of spatial filters for optical pattern recognition", *Appl. Opt.*, **21** (1982) 4391-4392.
- 7.47. H.J. Caulfield and M.H. Weinberg, "Computer recognition of 2-D patterns using generalized matched filters", *Appl. Opt.*, **21** (1982) 1699-1704.
- 7.48. F.T.S. Yu, S. Wu, A. Mayers and S. Rajan, "Color holographic storage in LiNbO_3 ", *Opt. Comm.*, **81** (1991) 348-352.

Chapter 8. Conclusions

We have experimentally investigated the nonlinear effects of a moving grating at large fringe modulations, i.e. the nonlinear dependence of the enhancement of the diffraction efficiency and the optimum fringe velocity on the fringe modulation. The experiments provide, in certain circumstances, an insight into the grating formation.

We have applied optical bias to moving gratings to control the holographic recordings. It has been shown that a suitable optical bias not only relaxes the influence of the nonlinear dependence of the optimum fringe velocity on the fringe modulation, but also enhances the diffraction efficiency, which is an unexpected phenomenon.

To overcome the inherent drawback of poor discrimination in the intensity correlation, we have realized real-time intensity edge enhancement by nonlinear holographic recording in BSO and applied this technique to real-time intensity correlation. The resulting improvement in discrimination is quite encouraging.

The moving grating technique has also been applied to real-time intensity correlation. It has been shown that the random fluctuations in the diffraction efficiency caused by transient energy transfer are considerably suppressed, which is significant for the threshold setting of the correlator, and the signal-to-noise ratio of the output is enhanced, important in a noisy environment.

We have also achieved colour object recognition by using a commercially available liquid crystal television as the real-time input device in an intensity correlator. In this research, real-time holographic recording using the coloured object was not adopted. However, it can be achieved by using composite photorefractive crystals, e.g. BSO for the green and blue primary colours and BTO for red, and a white laser in the optical system.

Multi-class optical pattern recognition has been realized using a synthetic discriminant function filter implemented with an Epson liquid crystal display in the real-time intensity correlator. The problems in displaying the synthetic discriminant function filter, the negative pixel values in the computed data and the accommodation

to the linear dynamic range of the liquid crystal television, have been solved by adopting an appropriate bias level and a scaling factor in the computed synthetic discriminant function data. This is the first realization of a synthetic discriminant function filter in an optical system. Experimental results are in good agreement with computer simulations.

We have designed a new type of spatial filter, the quantized amplitude-compensated matched filter. It is an amplitude-only filter with several discrete grey levels, and so it accommodates an Epson liquid crystal television operating on the amplitude-mostly modulation mode. It is also characterized by high discrimination in optical pattern recognition. Therefore it would be a reasonable choice for both good performance and real-time realization.

Lastly, we have demonstrated the advantages of the intensity correlator using the Fresnel transform: these include the absence of coherent noise, relaxed requirements on the alignment accuracy, and accommodation to spatial light modulators suffering from significant phase variations. It also plays an important role in an optical system which uses a laser diode array. As the structure of the laser diode array becomes more and more practical, it will become very attractive in image processing. The ideas of the real-time intensity correlator could be applied to optical neural networks, where the advantages described in this thesis may improve the performance merits of existing optical neural network systems.

Appendix. List of Publications

The following publications and conference presentations were based on the work presented in this thesis.

Publications:

1. Z.Q. Wang, W.A. Gillespie, C.M. Cartwright and C. Soutar; "Real-time computer-aided multiplexed optical intensity correlator using Fresnel holographic filters and a liquid crystal television", *Opt. Comm.*, **86** (1991) 19-24.
2. Z.Q. Wang, C.M. Cartwright, W.A. Gillespie and C. Soutar, "Evaluation of the performance of the amplitude-compensated matched filter with different threshold values", *Optik*, **90** (1992) 139-143.
3. Z.Q. Wang, C.M. Cartwright, W.A. Gillespie and C. Soutar; "Binarization effects in a correlator with an amplitude-compensated matched filter", *Opt. Comm.*, **92** (1992) 19-22.
4. Z.Q. Wang, W.A. Gillespie, C.M. Cartwright, and C. Soutar; "Optical pattern recognition using a synthetic discriminant amplitude-compensated matched filter", *Appl. Opt.*, **32** (1993) 184-189.
5. Z.Q. Wang, C.M. Cartwright, C. Soutar and W.A. Gillespie; "Real-time colour image correlation with a colour liquid crystal television and a Fresnel holographic filter", *Appl. Opt.*, **32** (1993) 715-717.
6. Z.Q. Wang, C. Soutar, W.A. Gillespie and C.M. Cartwright; "Real-time edge-enhanced object correlation using incoherent readout of photorefractive BSO", *Optik*, **93** (1993) 157-162.
7. Z.Q. Wang, C.M. Cartwright, W.A. Gillespie and C. Soutar; "An optical matched filter using a quantized amplitude compensation technique", *Optik*, **94** (1993) 78-82.

8. Z.Q. Wang, C.M. Cartwright and W.A. Gillespie; "Real-time intensity correlation with a synthetic discriminant function filter", *J. of Opt. Soc. of Am. B*, **11** (1994) 1842-1847.

9. Z.Q. Wang, W.A. Gillespie and C.M. Cartwright; "Holographic-recording Improvement in a bismuth silicon oxide crystal by the moving grating technique", *Appl. Opt.*, **33** (1994) 7627-7633.

10. Z.Q. Wang, C.M. Cartwright, W.A. Gillespie and N.J. Cook; "The effects of optical bias on moving gratings in BSO at large fringe modulation", *Appl. Opt.*, submitted, February 1995.

Conference Presentations:

1. Z.Q. Wang, W.A. Gillespie, C.M. Cartwright and C. Soutar; "Real-time computer-aided multiplexed optical intensity correlator using Fresnel holographic filters and a liquid crystal television", EQEC91/QE10 Heriot-Watt Univ., Edinburgh, U.K., August 1991.

2. W.A. Gillespie, C.M. Cartwright, Z.Q. Wang and C.Soutar; "Real-time colour image correlation using a colour liquid crystal television and a Fresnel holographic filter", CLEO'92, Los Angeles, USA.

3. W.A. Gillespie, Z.Q. Wang, C. Soutar and C.M. Cartwright; "Real-time incoherent edge-enhanced object correlation using Fresnel transform in photorefractive BSO", *Applied Optics and Optoelectronics*, Leeds Univ., September 1992.

4. Z.Q. Wang, C.M. Cartwright, W.A. Gillespie and C. Soutar; "An optical matched filter using a quantized amplitude-compensation technique", *Applied Optics and Optoelectronics*, Leeds Univ., September 1992.

5. C.M. Cartwright, W.A. Gillespie and Z.Q. Wang; "Multi-class object recognition in real-time using a synthetic discriminant function filter", *Photorefractive Materials, Effects, and Devices PRM'93*, Kiev, Ukraine, August 1993.

6. W.A. Gillespie, Z.Q. Wang and C.M. Cartwright; "Enhancement of large-modulation recording in BSO by the moving grating technique", Photorefractive Materials, Effects, and Devices PRM'93, Kiev, Ukraine, August 1993.
7. Z.Q. Wang, W.A. Gillespie and C.M. Cartwright; "Enhancement of High modulation recording in an intensity correlator using moving fringe technique", EQEC'93, Firenze, Italy, September 1993.
8. G.A. Brost, K.M. Magde, C.M. Cartwright, W.A. Gillespie and Z.Q. Wang; "Influence of modulation and fringe velocity on the photorefractive response with moving gratings in $\text{Bi}_{12}\text{SiO}_{20}$ ", CLEO/Europe-EQEC'94, Amsterdam, Netherlands, September 1994.
9. C.M. Cartwright, W.A. Gillespie, Z.Q. Wang and N.J. Cook; "The effects of optical bias on moving gratings in BSO at large fringe modulation", Photorefractive Materials, Effects, and Devices PRM'95, Kiev, Colorado, U.S.A., June 1995.